Nonlinear Optics Studies on the MAX IV Storage Rings

Olsson, David K

2022

Document Version:
Publisher's PDF, also known as Version of record

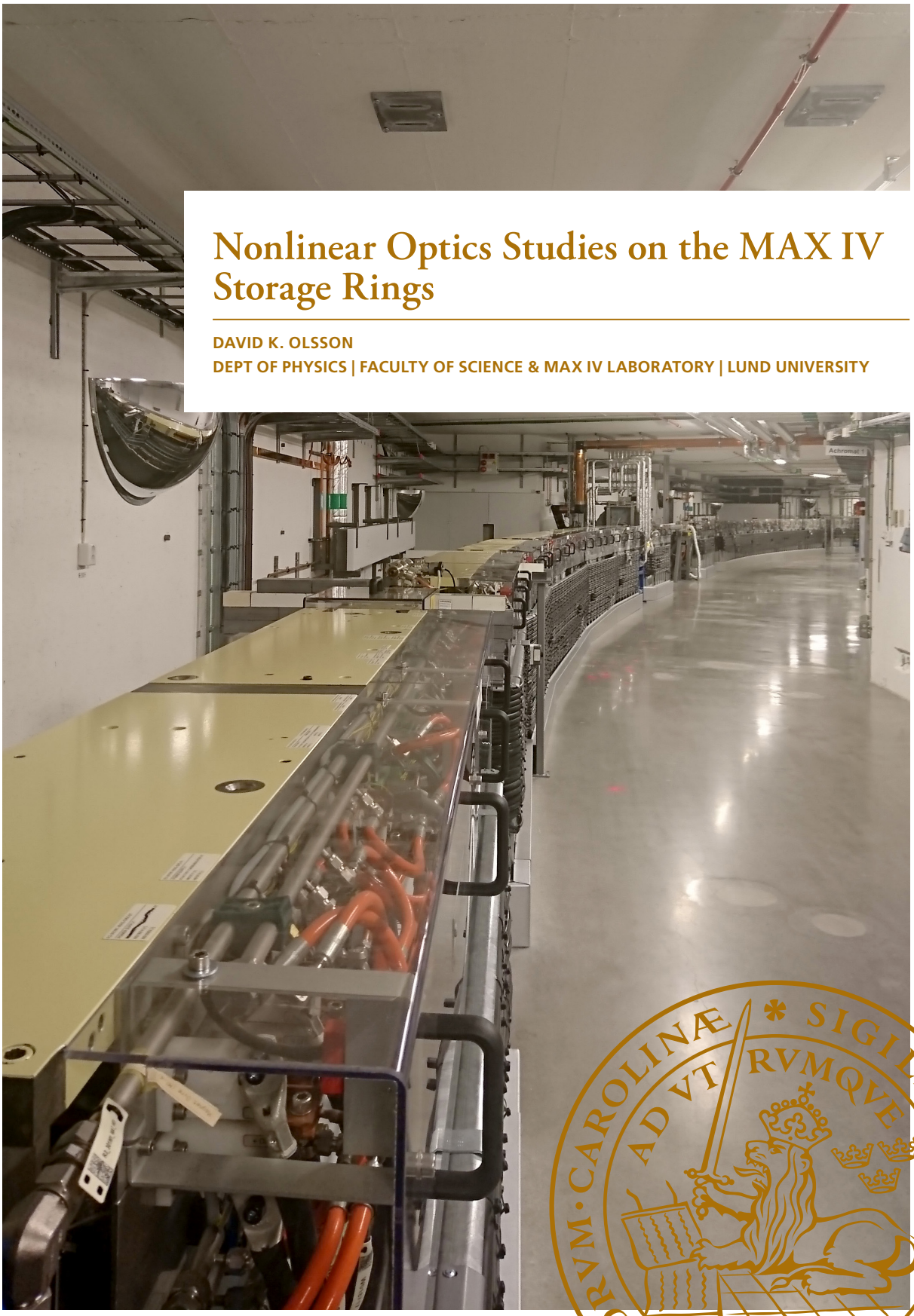

Nonlinear Optics Studies on the MAX IV Storage Rings

DAVID K. OLSSON
DEPT OF PHYSICS | FACULTY OF SCIENCE & MAX IV LABORATORY | LUND UNIVERSITY

Nonlinear Optics Studies on the MAX IV Storage Rings

Nonlinear Optics Studies on the MAX IV Storage Rings

by David K. Olsson

LUND
UNIVERSITY

Thesis for the degree of Doctor of Philosophy
Thesis advisors: Dr. Åke Andersson, Dr. Magnus Sjöström,
Dr. Francesca Curbis
Faculty opponent: Dr. James Safranek

To be presented, with the permission of the Faculty of Science of Lund University, for public criticism at the Department of Physics (Rydbergsalen) on Friday, the 14th of October 2022 at 13:15.

Organization	Document name
LUND UNIVERSITY Department of Physics Box 118 SE–221 00 LUND Sweden	**DOCTORAL DISSERTATION** Date of disputation 2022-10-14 Sponsoring organization
Author(s) David K. Olsson	

Title and subtitle

Nonlinear Optics Studies on the MAX IV Storage Rings

Abstract

The MAX IV Laboratory in Lund, Sweden, houses two electron storage rings operating at the energies 1.5, and 3 GeV. Both of these produce high-brilliance synchrotron radiation for beamline users. While the 1.5 GeV storage ring is a conventional third generation storage ring, employing a double-bend achromat structure, the MAX IV 3 GeV ring is the first realised fourth generation synchrotron. This ring employs a 7-bend achromat lattice structure to achieve a horizontal emittance of a few hundred pmrad. The multi-bend achromat design is the basis for many fourth generation synchrotron light sources. These lattice designs often require strong non-linear magnets in order to achieve their desired performance in terms of momentum acceptance and dynamic aperture, which in turn is needed to achieve the requirements in terms of beam lifetime and injection efficiency. The MAX IV 3 GeV storage ring itself is no exception, as it has a large number of chromatic sextupoles designed to minimize quadratic chromaticity. It also employs largely harmonic octupoles to minimise the amplitude-dependent tune shifts.

Because of the high requirements of the fourth generation storage rings' non-linear magnets, it is of general interest to find schemes which allow for accurate tuning of these elements, as well as the characterisation of the non-linear optics of the accelerator. Schemes of these types are already well established when dealing with the linear optics of a storage ring, and need now be developed further for the non-linear case.

This thesis presents schemes and results regarding the characterisation, correction, and optimisation of the non-linear optics of the MAX IV storage rings. These studies are mainly focussed on the MAX IV 3 GeV ring, but are aimed to be general enough that they can be applied on most fourth or third generation storage rings. This thesis also presents a specific case of the non-linear dynamics of a storage ring, where its properties are used to achieve pseudo single bunch through transverse resonance island buckets.

Key words

accelerator physics, synchrotron, storage ring, magnetic optics, non-linear optics, characterisation, optimisation

Classification system and/or index terms (if any)

Supplementary bibliographical information		Language English
ISSN and key title		ISBN 978-91-8039-362-1 (print) 978-91-8039-361-4 (pdf)
Recipient's notes	Number of pages 205	Price
	Security classification	

Nonlinear Optics Studies on the MAX IV Storage Rings

by David K. Olsson

LUND
UNIVERSITY

Cover illustration front: The MAX IV 3 GeV storage ring (Photo by David K. Olsson).

Cover illustration back: Rainbow over MAX IV (Photo by David K. Olsson).

Funding information: The MAX IV Laboratory Accelerator Division.

Faculty of Science, Department of Physics

ISBN: 978-91-8039-362-1 (print)
ISBN: 978-91-8039-361-4 (pdf)

Printed in Sweden by Media-Tryck, Lund University, Lund 2022

Printed matter
3041 0903

Media-Tryck is a Nordic Swan Ecolabel
certified provider of printed material.
Read more about our environmental
work at www.mediatryck.lu.se

MADE IN SWEDEN

If we knew what it was we were doing, it would not be called research, would it?
– Albert Einstein

Contents

List of publications

This thesis is based on the following publications, referred to by their Roman numerals:

I **Nonlinear optics from off-energy closed orbits**

D. K. Olsson, Å. Andersson, M. Sjöström
Physical Review Accelerators and Beams, vol. 23, 10, pp. 102803-13 (2020).

II **Commissioning and first-year operational results of the MAX IV 3 GeV ring**

P. F. Tavares, E. Al-Dmour, Å. Andersson, F. Cullinan, B. N. Jensen, D. Olsson, **D. K. Olsson**, M. Sjöström, H. Tarawneh, S. Thorin, A. Vorozhtsov
Journal of Synchrotron Radiation, 25, pp. 1291–1316 (2018).

III **Online Optimisation of the MAX IV 3 GeV Storage Ring Octupoles**

D. K. Olsson, Å. Andersson, M. Sjöström
Submitted to *Nuclear Instruments and Methods in Physics Research Section A*, August 2022.

IV **Studies on Transverse Resonance Island Buckets in third and fourth generation synchrotron light sources**

D. K. Olsson, Å. Andersson
Nuclear Instruments and Methods in Physics Research Section A, vol. 1017 (2021).

V **2nd Order Optics Symmetrisation through Off-Energy Orbit Response Matrix Analysis**

D. K. Olsson, Å. Andersson, M. Sjöström
Proceedings of the 10th International Particle Accelerator Conference, IPAC 2019, Melbourne, Australia, MOPTS004, pp. 841-843 (2019).

VI **Trials of Beam-Based Sextupole Calibration through 2nd Order Dispersion**

D. K. Olsson, Å. Andersson, M. Sjöström
Proceedings of the 10th International Particle Accelerator Conference, IPAC 2019, Melbourne, Australia, TUPGW064, pp. 1551-1553 (2019).

VII **Online Optimisation of the MAX IV 3 GeV Ring Dynamic Aperture**

D. K. Olsson
Proceedings of the 9th International Particle Accelerator Conference, IPAC 2018, Vancouver, BC, Canada, WEPAL047, pp. 2281-2283 (2018).

Publications not included in this thesis:

Beam Dynamics of the Transparent Injection for the MAX IV 1.5 GeV Ring

M. Apollonio, Å. Andersson, M. Brosi, **D. K. Olsson**, P. F. Taveres, A. S. Vorozhtsov
Proceedings of the 13th International Particle Accelerator Conference, IPAC 2022, Bangkok, Thailand, MOPOPT022, pp. 284-287 (2022).

Improved Emittance and Brightness for the MAX IV 3 GeV Storage Ring

M. Apollonio, Å. Andersson, M. Brosi, R. Lindvall, **D. K. Olsson**, M. Sjöström, R. Svärd, P. F. Taveres
Proceedings of the 13th International Particle Accelerator Conference, IPAC 2022, Bangkok, Thailand, MOPOPT023, pp. 288-291 (2022).

Studying the Dynamic Influence on the Stored Beam from a Coating in a Multipole Injection Kicker

J. Kallestrup, Å. Andersson, J. Breunlin, **D. K. Olsson**, P. F. Tavares, P. Alexandre, R. Ben El Fekih
Proceedings of the 10th International Particle Accelerator Conference, IPAC 2019, Melbourne, Australia, TUPGW063, pp. 1547-1550 (2019).

Status of the MAX IV Accelerators

P. F. Tavares, E. Al-Dmour, Å. Andersson, J. Breunlin, F. Cullinan, E. Mansten, S. Molloy, D. Olsson, **D. K. Olsson**, M. Sjöström, S. Thorin
Proceedings of the 10th International Particle Accelerator Conference, IPAC 2019, Melbourne, Australia, TUYPLM3, pp. 1185-1190 (2019).

Pulse-Picking by resonant Excitation (PPRE) for Timing Users at the MAX IV 3 GeV Storage Ring

T. Olsson, Å. Andersson, **D. K. Olsson**
Proceedings of the 9th International Particle Accelerator Conference, IPAC 2018, Vancouver, BC, Canada, THPMK004, pp. 4300-4303 (2018).

Acknowledgements

In 2016, at the end of my fourth year of the five-year engineering program at LTH, I was looking for a summer job. At the suggestion of my good friend Hans, I reached out to Professor Sverker Werin regarding the possibility of working at the MAX IV Laboratory. Sverker contacted Magnus Sjöström and, to my surprise, I was able to start working at the laboratory that summer. I spent much of that summer in the MAX IV control room, writing control software for the storage rings. I remember fondly the control room stand-up meetings, in which the smartest people I've ever met would discuss solutions to problems I didn't understand. During that summer I also, somewhat unexpectedly, got to shake hands with both the Swedish Prime Minister, Stefan Löfven, and the king of Sweden, Carl XVI Gustaf. They were both shorter than I expected.

The summer job turned into a part time job, and in the beginning of 2017 I started my master's project with Åke Andersson and Magnus Sjöström as supervisors. This was almost immediately followed by a PhD position, which produced this thesis.

I would firstly like to thank my supervisors, Åke Andersson, Magnus Sjöström and Francesca Curbis. Åke, thank you for your unrelenting optimism, it helped me pursue the projects I found interesting. Magnus, thank you for grounded pragmatism, without it much of my work never would have made it to print. Francesca, thank you for your guidance through the academic world. Thank you all for your enthusiasm and support.

I would also like to thank Francis Cullinan and Jonas Breunlin. Francis, thank you for helping me with the bunch-by-bunch feedback system and explaining how it works each time I forgot. Jonas, thank you for your help with setting up equipment at the diagnostic beamlines. I would like to thank Joel and Teresia for showing me the ropes during the beginning of my PhD studies. I would also like to thank all members of our "MAX IV students" group: Joel, Teresia, Francis, Jonas, Jonas, Mihai, Neven, Miriam, Henrique, Johan, Marco, and Domenico. Thank you for providing a comforting social context.

I would like to thank the remainder of the accelerator development group, as well as the operations group, whose support with systems with which I was not familiar was invaluable when performing measurements on the machines.

Finally, I would like to thank my parents, Anna-Lena and Bertil, for always being there and for supporting my interest in science, and I would like to thank my girlfriend, Rebecca, for supporting me through the entirety of my PhD studies.

Populärvetenskaplig sammanfattning på svenska

En synkrotron är en cyklisk partikelaccelerator i vilken laddade elementarpartiklar, t.ex. elektroner, färdas i en sluten bana med en hastighet nära ljusets. Denna bana definieras av magnetiska fält genererade av starka magneter. När partiklarna färdas genom dessa fält emitterar de elektromagnetisk strålning i sin färdriktning. Denna strålning kallas ”synkrotronljus” eller ”synkrotronstrålning”. Många partikelacceleratorer runt om i världen är konstruerade specifikt för att producera denna synkrotronstrålning. Strålningen har vissa önskvärda inställbara egenskaper som gör den till ett viktigt verktyg för att studera processer och strukturer i många vetenskapliga fält. Materialforskning, forskning inom medicin, geologi, och till och med arkeologi, bedrivs vid synkrotronljuskällor av forskare som reser över hela världen för att få tillfälle att använda sig av synkrotronstrålningen.

MAX IV-laboratoriet invigdes år 2016. Det hyser världens första ”fjärde generations” synkrotron, i form av dess 3 GeV elektronlagringsring med en omkrets på 528 meter. Denna nya generation av synkrotroner erbjuder synkrotronstrålning med högre ”briljans” än föregående generationer, dvs. användbar strålning med en högre intensitet än vad som tidigare har uppnåtts. Ökningen av briljans möjliggjordes av en innovativ design gällande styrkan och fördelningen av de magneter som styr elektronernas bana. Denna design har sedan dess stått som inspiration för många nya synkrotronljuskällor runt om i världen, samt för uppgraderingsprogram av existerande källor.

Hur en accelererad elektron reagerar när de passerar de magnetiska fälten i en synkrotron kan liknas vid hur ljus reagerar när det passerar en lins. Därför används benämningen *magnetoptik*, som vanligen förkortas till enbart *optik*. Denna delas i sin tur ofta upp i linjär och ickelinjär optik. Alla fjärde generationens synkrotroner innehåller starka ickelinjära magneter. Dessa magneters styrka måste kunna ställas in noggrant för att uppnå den önskade optiken, och därmed en accelerator med den önskade prestandan. För detta behöver nya metoder utvecklas för kalibrering samt karaktärisering av ickelinjär optik.

Denna avhandling presenterar metoder och resultat av korrektion, karaktärisering, samt optimering av den ickelinjära optiken av MAX IV-laboratoriets lagringsringar, framför allt dess fjärde generations synkrotron. Dessa procedurer har för syfte att öka olika aspekter av en accelerators prestanda, och vara generaliserbara nog att kunna appliceras på många andra synkrotroner runt om i världen, både tillhörande tredje och fjärde generationen.

Nonlinear Optics Studies on the MAX IV Storage Rings

List of Variables

c	- Speed of light
ε_0	- Permittivity of vacuum
e	- Particle charge
m_0	- Particle rest mass
E	- Particle energy
$\mathbf{p}$, p	- Particle momentum, magnitude
δ	- Relative particle momentum error
$(\mathbf{u}_x, \mathbf{u}_y, \mathbf{u}_s)$	- Frenet-Serret coordinates
$\mathbf{E}$	- Electric field
$\mathbf{B} = (B_x, B_y, B_s)$	- Magnetic field
r_0	- Reference particle position
(q_i, q_i')	- Transverse particle phase-space position
θ	- Dipole kick
ρ	- Radius of curvature
h	- Magnetic dipole field component
k	- Magnetic quadrupole field component
m	- Magnetic sextupole field component
o	- Magnetic octupole field component
L	- Orbit circumference
β, β_0, β_1	- Beta function, linear beta function, chromatic function
α	- Alpha function
γ	- Gamma function
ε	- Single particle emittance
Ψ	- Phase advance
ν	- Betatron tune
η, η_1, η_2	- Dispersion function, linear, 2nd order
α_c	- Momentum compaction factor (linear)
ξ	- Chromaticity
κ	- Emittance coupling
A	- Transverse acceptance
σ	- Transverse beam size
σ'	- Transverse beam divergence
δ_{acc}	- Momentum acceptance
σ_s	- Bunch length
τ	- Beam lifetime
ω_{RF}	- Accelerating cavity angular frequency
ω_{rev}	- Ring revolution angular frequency

n_{RF}	- Harmonic number
T	- Revolution period
ψ_s	- Synchrotron phase
Ω	- Synchrotron frequency

Chapter 1

Introduction

The first particle accelerators were built for the purpose of conducting experiments in the field of high-energy physics. These were electrostatic linear accelerators which grew in size and cost with the desired energy of the accelerated particle. By steering the particle beam in a circular path, they could be made to pass the accelerating structures more than once, allowing circular accelerators to reach higher particle energies without an increase in size. The steering was done using magnetic fields which, according to predictions by Iwanenko and Pomeranchuk in 1944[1], would result in particle energy losses in the form of radiation. This radiation was first observed in 1946 in a 70 MeV synchrotron in Schenectady, US. The observed radiation was named *synchrotron radiation*[2]. The first experiments utilizing synchrotron radiation as a measurement tool were carried out parasitically at such facilities.

The 1960s saw the rise of a new type of particle accelerator, which would become the basis of today's synchrotron light sources: the storage rings. In these, the particle beam could circulate for many hours, allowing higher beam current and greater beam availability. Although the storage rings were mainly built for the purpose of atomic and nuclear physics experiments, they proved to be ideal sources of synchrotron radiation. These storage rings are called the first generation synchrotron light sources, with each subsequent generation marking a large step increase in photon beam brightness[3].

The second generation of light source followed soon after. These facilities were specifically dedicated to the production of synchrotron radiation. The introduction of *insertion devices*, long arrays of alternating polarity magnets with the express purpose of generating radiation with more tunable desirable properties, soon called for a third generation of light sources: storage rings optimised for a low emittance with long straight sections for insertion devices. These machines where generally based on the

double-bend achromat design[3,4] and are still in use all over the world.

The story of the MAX IV Laboratory starts with the MAX I project, an electron storage ring designed both for nuclear physics and synchrotron radiation research. The ring was taken into operation in 1985 and had an experienced and motivated user community from the beginning. There were quickly ideas for the next accelerator and already in 1995 the 1.5 GeV third generation storage ring, MAX II, was taken into operation. MAX II became one of the first third generation light sources built in the world. The expanding user program at MAX-lab soon called for additional beamlines. These were realised in the smaller MAX III storage ring. This was 700 MeV storage ring which was capable of hosting a few low energy beamlines. Both the MAX II and MAX III storage rings served as important test beds for technologies which were later employed in the MAX IV project[5].

With the third generation light sources, storage rings where considered to be a mature technology. No major further improvements were believed possible. However, the MAX IV 3 GeV storage ring showed that a further reduction of emittance was possible by employing a multi-bend achromat design[6]. The MAX IV Laboratory was inaugurated in 2016. It operates two storage rings, the 3 GeV storage ring, which can be considered the first fourth generation storage ring, and the 1.5 GeV ring, a more traditional third generation light source. It also operates a short-pulse facility and a linac serving both the short pulse facility and as a full energy injector to the two storage rings[5,7].

The successful commissioning of the MAX IV 3 GeV storage ring sparked the development of several storage ring upgrade programs at synchrotron light source facilities around the world. A common feature of these upgrades is the use of a multi-bend achromat structure. Such a lattice generally requires stronger high-order magnets and more detailed control over the non-linear optics in order to achieve the desired performance.

This thesis presents research conducted to better understand, improve, and control the non-linear optics of the MAX IV storage rings. The schemes and methods used in this thesis can be used at other similar machines, including present and future fourth generation light sources. Chapter 2 gives a short summary of synchrotron radiation and its desirable properties. Chapter 3 aims to give a sufficient understanding of the theory of beam dynamics, as well as the conventions used in this thesis. Chapter 4 details the optics calibration schemes regularly used at the MAX IV Laboratory, while Chapter 5 presents online optimisation of the MAX IV 3 GeV storage ring and its results. Chapter 6 summarises the experiences of using Transverse Resonance Island buckets as a potential scheme for achieving pseudo single-bunch delivery in the 1.5 GeV ring. Finally, conclusions and a future outlook are presented in Chapter 7.

Chapter 2

Synchrotron Radiation

A charged particle undergoing acceleration will radiate energy in the form of electromagnetic waves[8]. In a circular accelerator, such as a storage ring, this occurs when the path of the relativistic stored particle is bent by magnetic fields. This particular radiation is called, as previously mentioned, synchrotron radiation and has some properties which has made it a useful tool in many scientific fields.

The radiated power of a highly relativistic particle travelling in a circular accelerator is given by[9]

$$P_s = \frac{e^2 c}{6\pi\varepsilon_0} \frac{1}{(m_0 c^2)^4} \frac{E^4}{\rho^2} \tag{2.1}$$

where e is the particle charge, c is the speed of light, ε_0 is the vacuum permittivity, m_0 is the particle rest mass, E is the total particle energy, and ρ is the radius of curvature of the particle orbit.

Since this power is inversely proportional to m_0^4 the radiated power of a heavier particle, such as a proton, is significantly less than that of an equally energetic lighter particle, such as an electron. Generating high power synchrotron radiation is easier using electrons than heavier particles, and most synchrotron light sources do indeed use electrons.

An accelerating non-relativistic particle will radiate electromagnetic waves with axial symmetry around the direction of acceleration. This is also true for a relativistic particle when observed in the frame of reference moving alongside the particle[8]. The spacial distribution of the radiation can be transformed from the rest frame to the laboratory frame using a *Liénard–Wiechert potential*[10,11]. This results in the emitted

radiation forming a sharply forward peaked distribution (tangential to the particle trajectory) in the shape of a narrow cone. It can be shown that the half-angle of this cone of radiation is approximately $1/\gamma_L$ (units of radians), where γ_L is the *Lorentz factor*[9]. For an electron storage ring with particle energies of 3 GeV, such as the large storage ring at the MAX IV Laboratory, the Lorentz factor is $\gamma_L = 5871$ which corresponds to a half-angle of $< 0.17\,\mathrm{mrad}$, or $0.01°$. This directionality is one of the properties which gives the synchrotron radiation its high *brilliance*, B_γ[9], which is defined as

$$B_\gamma = \frac{\text{photons}}{\text{s } 0.1\% \text{ BW mm}^2\text{mrad}^2\text{A}} \tag{2.2}$$

In order to generate higher brilliance synchrotron radiation with tunable properties, insertion devices (IDs) are installed in light sources such as storage rings. Although these can differ somewhat in structure they, are generally periodic magnetic structures consisting of an array of alternating polarity magnets. These cause the path of the particles to wiggle as they pass through the device, generating synchrotron radiation with a higher brilliance than that generated by a single bending magnet. At the MAX IV Laboratory, all synchrotron light used by the user beamlines is currently generated by IDs.

Chapter 3

Beam Dynamics

This chapter aims to give a sufficient understanding of the theory of beam dynamics, as well as the conventions used in this thesis. The main focus of this chapter, and this thesis, is the transverse beam dynamics. However, the basics of longitudinal beam dynamics will also be presented in order to be able to examine certain aspects of the performance of a storage ring.

3.1 A Charged Particle in a Magnetic Field

Before we can go into more detail regarding the description of beam steering and focussing in an electron storage ring, we have to look at the more general case of a charged particle moving in an electromagnetic field.

3.1.1 The Lorentz Force

A particle of charge e travelling through an electromagnetic field (where the electric field is denoted as **E** and the magnetic as **B**) with a velocity **v** will experience a force **F** known as *the Lorentz Force*[8], which is given by

$$\mathbf{F} = e(\mathbf{E} + \mathbf{v} \times \mathbf{B}) \tag{3.1}$$

Electrons travelling in a particle accelerator, such as a synchrotron, often do so at a speed close to the speed of light, c. Because of this, the contribution of a technologically attainable magnetic field, **B**, to the Lorentz force acting on these particles is

much greater than the contribution of an equally attainable electric field, **E**. For example, an electron travelling almost at the speed of light perpendicular to a magnetic field with a strength of 1 T will experience a force of equal strength as an electron in a $300\,\mathrm{MVm}^{-1}$ electric field. A static magnetic field strength of 1 T is currently technologically attainable, while a static $300\,\mathrm{MVm}^{-1}$ electric field is not. As a result, the beam steering and focussing in accelerators is generally done using magnetic fields, while the acceleration is done using electric fields (see Sec. 3.4).

3.1.2 Curvilinear Coordinate System

It is possible to describe the motion of a charged particle in a magnetic *lattice* (i.e. an array of magnetic elements) using a strictly Cartesian coordinate system, however this would result in long and cumbersome expressions. It is beneficial to adopt a *Frenet-Serret coordinate system*[12]. We define this curvilinear coordinate system as an orthogonal coordinate system moving along the trajectory of an ideal reference particle, as seen in Fig. 3.1[13]. The three unit vectors of this coordinate system are:

$$\begin{aligned}
\mathbf{u}_x(s) &\equiv -\frac{\mathrm{d}\mathbf{u}_s(s)}{\mathrm{d}s} \Big/ \left|\frac{\mathrm{d}\mathbf{u}_s(s)}{\mathrm{d}s}\right| \\
\mathbf{u}_y(s) &\equiv \mathbf{u}_s(s) \times \mathbf{u}_x(s) \\
\mathbf{u}_s(s) &\equiv \frac{\mathrm{d}\mathbf{r}_0(s)}{\mathrm{d}s}
\end{aligned} \tag{3.2}$$

where $\mathbf{r}_0$ is the position of a reference particle travelling along the ideal beam path.

Most conventional accelerators have an ideal beam path limited to the horizontal plane, which results in the $\mathbf{u}_y$ unit vector aligning with the vertical direction.

3.1.3 Expansion of the Magnetic Field

Using the curvilinear coordinate system we treat a particle moving parallel to the s-axis, $\mathbf{v} = (0, 0, v_s)$, through a transverse magnetic field, $\mathbf{B} = (B_x, B_y, 0)$. Looking specifically at movement in the horizontal plane, the particle will be affected by the Lorentz force, $F_L = -ev_sB_y$, and the centrifugal force, $F_c = mv_s^2/\rho$, where m is the particle mass and ρ is the radius of curvature. The balance of the forces leads to the relation

$$\frac{1}{\rho(x, y, s)} = \frac{e}{p} B_y(x, y, s) \tag{3.3}$$

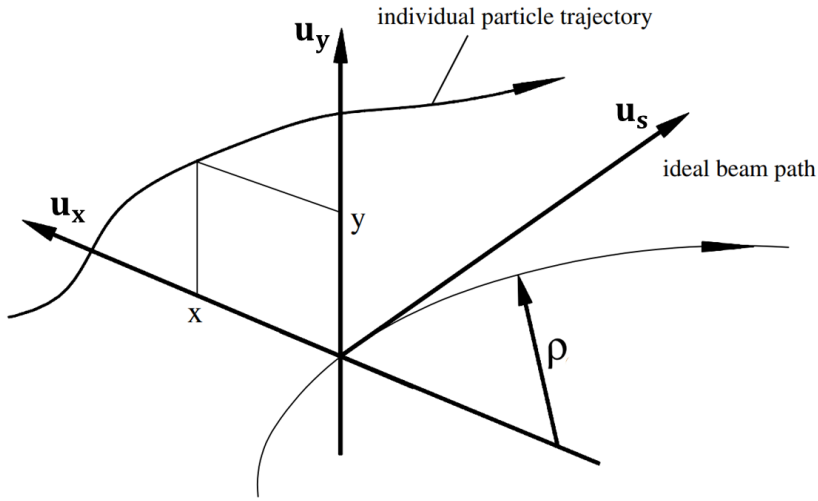

Figure 3.1: Curvilinear coordinate system with unit vectors corresponding to Eq. (3.2). Adapted from Wiedemann [13].

There is an equivalent expression for the motion in the vertical plane. The fraction e/p is known as the *beam rigidity*, where $p = |\mathbf{p}|$ is the magnitude of the momentum of the particle. It states that a particle of lower charge, or higher momentum, will be deflected less by the magnetic field.

Since the transverse movement of the particle is generally small compared to the radius of curvature, we can expand the magnetic field around the ideal beam path

$$B_y(x) = B_{y0} + \frac{\partial B_y}{\partial x}\Big|_{x,y=0} x + \frac{1}{2!}\frac{\partial^2 B_y}{\partial x^2}\Big|_{x,y=0} x^2 + \frac{1}{3!}\frac{\partial^3 B_y}{\partial x^3}\Big|_{x,y=0} x^3 + \ldots \quad (3.4)$$

Multiplying by the beam rigidity, e/p, we get the multipole expansion seen in Tab. 3.1 [14]. Here, only the *upright* multipole terms are presented. For a full expansion of an arbitrary transverse magnetic field the *skew* multipole terms also need to be included. However, in the design of magnetic lattices, upright multipole fields are generally favoured, as the low order upright fields lead to decoupled horizontal and vertical motion [15].

The multipole terms are functions of the longitudinal coordinate, s, and depend on the configuration of magnets in the ring. Since a particle will pass the same magnets with each revolution, the multipole terms are also periodic with the circumference of the ring, L. The definitions in Tab. 3.1 are commonly used, and will be used through-

Table 3.1: Definition of the first four orders of upright multipole fields in the expansion of the magnetic field. The corresponding terms can also be derived in the vertical plane.

dipole	$\frac{e}{p}B_{y0} = \frac{1}{\rho} = h$
quadrupole	$\frac{e}{p}\frac{\partial B_y}{\partial x}\Big\|_{x,y=0} = k$
sextupole	$\frac{e}{p}\frac{\partial^2 B_y}{\partial x^2}\Big\|_{x,y=0} = m$
octupole	$\frac{e}{p}\frac{\partial^3 B_y}{\partial x^3}\Big\|_{x,y=0} = o$

out this thesis. However, there are several other equally valid definitions which differ by some numerical factor used throughout the field of accelerator physics.

The multipole expansion of the magnetic field allows us to treat the dynamics of the motion one order at a time, generally from low to high. The dipole and quadrupole components of the field are able to steer and focus the beam, respectively, while higher order terms are used to correct for higher order effects which will be discussed in Sec. 3.3. The magnetic lattice of a ring is generally made up of linear magnetic elements, i.e. dipoles and quadrupoles, in addition to non-linear magnet elements, and sections where the magnetic field is zero, *drift sections*. When treating the magnetic optics of a ring it is common to separate it into *linear beam optics* and *non-linear beam optics*. In linear optics the 2nd order and higher terms are neglected. In non-linear optics the neglected terms are included.

When designing a ring the magnets are generally categorised according to their multipole expansion field content, with each magnet usually providing a single order of the multipole. However, sometimes *combined function magnets* are used, which provide two or more orders of the expansion simultaneously. These tend to be more difficult to manufacture, but also provide a more compact magnetic lattice. Both MAX IV storage rings make use of combined function magnets [16].

3.2 Linear Optics

In this section we will look at the linear approximation of the particle dynamics, i.e. the linear optics. This approximation will limit the derivation to dipole and quadrupole fields. We will return to the higher order non-linear effects and multipole fields in Sec. 3.3. This section is also limited to the upright multipole field terms, as these lead to simpler expressions, and the skew magnets are not the main focus of the work presented in this thesis. In most storage rings, including the MAX IV storage rings, the majority of main magnets are upright magnets. Additionally, the theory presented here assumes a particle with constant energy which, while not being strictly accurate, is a fair approximation for a storage ring.

3.2.1 The Equation of Motion

The transverse motion of a particle moving through a magnetic lattice is described by its position (x, y) and angle (x', y') relative to the ideal orbit in the Frenet-Serret coordinate system defined in Eq. (3.2). These variables describe the transverse *phase-space* position of the particle. The linear equation of motion of a charged particle moving through a magnetic lattice with its ideal beam path limited to the horizontal plane is [17]

$$\begin{aligned} x''(s) + \big(h^2(s) + k(s)\big)x(s) &= h(s)\delta \\ y''(s) - k(s)y(s) &= 0 \end{aligned} \tag{3.5}$$

where δ is the relative momentum error of the particle given by

$$\frac{1}{p} = \frac{1}{p_0(1+\delta)} = \frac{1}{p_0}\sum_{n\geq 0}(-\delta)^n \tag{3.6}$$

The derivation of the equation of motion can be found in Appx. A.1.

From here on out, the longitudinal dependence of the multipole terms will not be explicitly written out in order to increase the legibility of long expressions.

3.2.2 The Twiss Parameters

For an on-momentum particle ($\delta = 0$) Eq. (3.5) becomes an instance of Hill's equation [18]. We can generalise the equation of motion as

$$q_i''(s) + K(s)q_i(s) = 0 \tag{3.7}$$

where (q_i, q_i') is the particle position in either horizontal, $i = x$, or vertical, $i = y$, phase space, and $K(s)$ is an arbitrary piece-wise continuous function which represents the focussing along the lattice.

By nature of a circular accelerator we have the periodicity $K(s) = K(s + L)$. The equation of motion resembles that of a harmonic oscillator, and has known solutions of the form [9,19]

$$
\begin{aligned}
q_i(s) &= \sqrt{\varepsilon_i}\sqrt{\beta_i(s)}\cos\big(\Psi_i(s)+\phi_i\big) \\
q_i'(s) &= p_i(s) = -\frac{\sqrt{\varepsilon_i}}{\sqrt{\beta_i(s)}}\Big[\alpha_i(s)\cos\big(\Psi_i(s)+\phi_i\big)+\sin\big(\Psi_i(s)+\phi_i\big)\Big]
\end{aligned}
\tag{3.8}
$$

where β is the *beta function*, ϕ is an arbitrary phase for the specific particle, and the *phase advance*, Ψ, is defined as

$$
\Psi_i(s) \equiv \int_{s_0}^{s} \frac{\mathrm{d}\sigma}{\beta_i(\sigma)} \tag{3.9}
$$

where $s_0 \leq s$ is an arbitrary reference position along the reference orbit of the ring, and the *alpha function*, α, is defined as

$$
\alpha_i(s) \equiv -\frac{\beta_i'(s)}{2} \tag{3.10}
$$

Equation (3.8) shows that a particle will perform transverse oscillations, so called *betatron oscillations*, around the reference orbit. The amplitude of these are governed by the single-particle *emittance*, ε, and the beta function, $\beta(s)$. Due to the longitudinal dependence of the beta function the amplitude of the betatron oscillations will depend on s.

For any arbitrary particle the maximum amplitude of the oscillation is $\sqrt{\varepsilon_i\beta_i(s)}$ and occurs at the longitudinal position, s, which maximises $\cos(\Psi_i(s)+\phi_i)$. In the case of an ensemble of particles, such as the one found in a storage ring, all betatron oscillation amplitudes are limited by $\sqrt{\varepsilon_i\beta_i(s)}$, which defines the transverse size of the beam.

The number of full betatron oscillations performed each turn by a particle travelling in a circular accelerator is know as the *betatron tune*,

$$
\nu_i \equiv \frac{1}{2\pi}\oint \frac{\mathrm{d}s}{\beta_i(s)} \tag{3.11}
$$

The betatron tune is often simply referred to as the tune, or the transverse tune. The horizontal and vertical tunes together make up the *working point* of the storage ring. The importance of a well chosen working point will be discussed further in Sec. 3.2.5.

From Eq. (3.8) we can derive the relation

$$
\gamma_i(s)q_i^2(s) + 2\alpha_i(s)q_i(s)q_i'(s) + \beta_i(s)q_i'^2(s) = \varepsilon_i \tag{3.12}
$$

where the *gamma function*, γ, is defined as

$$\gamma_i(s) \equiv \frac{1+\alpha_i^2(s)}{\beta_i(s)} \tag{3.13}$$

The three optical functions, the beta function, $\beta(s)$, alpha function, $\alpha(s)$, and gamma function, $\gamma(s)$, are collectively known as the *Twiss parameters*. These define, in Eq. (3.12), an ellipse in phase space with an area of $\pi\varepsilon_i$. In perfect accordance with Liouville's theorem [20] this area, and thus ε_i, is a constant of motion as long as the particle follows the equation of motion (Eq. (3.8)). Knowing the Twiss parameters and the phase advance also allows the calculation of how a particle propagates in phase space given an initial position.

3.2.3 Dispersion

Let us now consider the motion of an off-momentum particle. Returning to Eq. (3.5) we can write the horizontal displacement of an off-momentum particle as

$$x_{total}(s) = x(s) + x_\delta(s) = x(s) + \eta(s)\delta \tag{3.14}$$

where η is called the *dispersion function*.

Inserting Eq. (3.14) into Eq. (3.5) results in

$$\begin{aligned} &x''(s) + \eta''(s)\delta + (h^2+k)\big(x(s)+\eta(s)\delta\big) \\ &= x''(s) + (h^2+k)x(s) \\ &+ \big(\eta''(s) + (h^2+k)\eta(s)\big)\delta = h\delta \end{aligned} \tag{3.15}$$

Since the part of the equation independent of δ is equal to zero (see Eq. (3.5)) the equation becomes

$$\eta''(s) + (h^2+k)\eta(s) = h \tag{3.16}$$

This equation can be transformed into the equation of motion of a forced harmonic oscillator using *Floquet's transformation* [21]. The transformation applied to a general instance of the forced Hill's equation can be found in Appx. A.2. In the case of the dispersion the $q_i(s)$, $K(s)$, and $f(s)$ functions found in the appendix correspond to

η, (h^2+k), and h, respectively. From this we arrive at an expression for the dispersion function given by

$$\eta(s) = \frac{\sqrt{\beta(s)}}{2\sin\pi\nu}\int_s^{s+L}\sqrt{\beta(\sigma)}h(\sigma)\cos\big(\pi\nu + \Psi(s) - \Psi(\sigma)\big)\mathrm{d}\sigma \tag{3.17}$$

The dispersion is a measure of how the closed orbit of a particle is displaced as a consequence of that particle's error in momentum, relative to the nominal momentum. Dispersion arises due to the $h\delta$ term in the horizontal equation of motion (see Eq. (3.5)). Since there is no equivalent term in the vertical equation of motion, the vertical dispersion function is in general nominally zero.

3.2.4 Closed Orbit Distortion

In a storage ring, or any other circular accelerator, the beam is likely to encounter a number of static dipole errors while circulating. Assuming these errors do not cause the beam to be lost, they will alter the equilibrium orbit of the beam causing a *closed orbit distortion*.

Assume a number of dipole errors, Δh_{ij}, of the form

$$\Delta h_{ij} = \begin{cases} \frac{\theta_{ij}}{\Delta s}, & \text{if } s_j < s < s_j + \Delta s \\ 0, & \text{otherwise} \end{cases} \tag{3.18}$$

where i indicates the transverse plane, s_j is the longitudinal position of the error, θ_{ij} is the kick angle of the integrated field, and Δs is the length of the error. Inserting these disturbances into the generalised equation of motion of an on-momentum particle (see Eq. (3.7)) results in

$$q_i''(s) + K(s)q_i(s) = \sum_j \Delta h_{ij} \tag{3.19}$$

Using the Floquet's transformation derived in Appx. A.2, with $f(s) = \sum_j \Delta h_{ij}$ the expression for the closed orbit distortion becomes

$$q_{i\theta}(s) = \frac{\sqrt{\beta_i(s)}}{2\sin\pi\nu_i}\sum_j\int_s^{s+L}\sqrt{\beta_i(\sigma)}\Delta h_{ij}\cos\big(\pi\nu_i + \Psi_i(s) - \Psi_i(\sigma)\big)\mathrm{d}\sigma \tag{3.20}$$

Assuming a kick from a thin dipole error, i.e. letting $\Delta s \to 0$, the expression can be written using the integrated kick angle and the dirac function, δ_{s_j}, as

$$\begin{aligned} q_{i\theta}(s) =& \frac{\sqrt{\beta_i(s)}}{2\sin\pi\nu_i} \sum_j \int_s^{s+L} \sqrt{\beta_i(\sigma)}\theta_{ij}\delta_{s_j}(\sigma)\cos\big(\pi\nu_i + \Psi_i(s) - \Psi_i(\sigma)\big)\mathrm{d}\sigma \\ =& \frac{\sqrt{\beta_i(s)}}{2\sin\pi\nu_i} \sum_j \sqrt{\beta_{ij}}\theta_{ij}\cos\big(\pi\nu_i + \Psi_i(s) - \Psi_{ij}\big) \end{aligned} \tag{3.21}$$

where $\beta_{ij} = \beta_i(s_j)$ and $\Psi_{ij} = \Psi_i(s_j)$.

With a different equilibrium orbit, the length of the orbit may also change. Since the phase at which the particle reaches the RF cavities, the *synchronous phase*, is required to remain the same, the change of orbit length results in a change of momentum. As seen in Sec. 3.2.3 this results in a change of the closed orbit governed by the dispersion function. In order to include this effect in the expression for the closed orbit distortion the induced change of momentum must be found.

Beginning with the total path length to first order which is given by[22]

$$L = L_0 + \Delta L = \oint \big(1 + hx(s)\big)\mathrm{d}s = L_0 + \oint hx_\delta(s)\mathrm{d}s + \oint hx_\theta(s)\mathrm{d}s \tag{3.22}$$

where L_0 is the path length of the nominal orbit, and $x_\delta(s)$ and $x_\theta(s)$ are the changes to the horizontal closed orbit due to a change in momentum and dipole errors, respectively.

Since, to first order, there will only be a change of momentum if the orbit equilibrium changes in the plane of bending, only the horizontal case is treated here. The synchronicity requirement gives us that $\Delta L = 0$ which allows us to write

$$-\oint hx_\delta(s)\mathrm{d}s = \oint hx_\theta(s)\mathrm{d}s \tag{3.23}$$

The left-hand side becomes

$$-\oint hx_\delta(s)\mathrm{d}s = -\oint h\eta(s)\delta\mathrm{d}s = -\alpha_c L_0\delta \tag{3.24}$$

where α_c is known as the *momentum compaction factor*, which is a measure of the relative change of orbit length given a relative change of momentum.

The right-hand side can be rewritten using Eq. (3.21) as

$$\begin{aligned}
&\oint h x_\theta(s)\mathrm{d}s \\
&= \sum_j \theta_j \oint \delta_{s_j} \frac{\sqrt{\beta_x(\sigma)}}{2\sin\pi\nu_x} \oint \sqrt{\beta_x(s)} h(s) \cos\big(\nu_x\pi + \Psi_x(s) - \Psi_x(\sigma)\big)\mathrm{d}s\mathrm{d}\sigma \\
&= \sum_j \theta_j \eta(s_j)
\end{aligned} \tag{3.25}$$

The shift in momentum from the new equilibrium orbit becomes

$$\delta = -\sum_j \frac{\theta_j \eta(s_j)}{\alpha L_0} \tag{3.26}$$

Adding the dispersive change in orbit to Eq. (3.21), in the same way as was done in Eq. (3.14), results in a final expression for the closed orbit distortion

$$q_{i\theta}(s) = \frac{\sqrt{\beta_i(s)}}{2\sin\pi\nu_i} \sum_j \theta_j \Big[\sqrt{\beta_{ij}} \cos\big(\nu_i\pi + \Psi_i(s) - \Psi_{ij}\big) - \frac{\eta_i(s_j)\eta_i(s)}{\alpha L_0} \Big] \tag{3.27}$$

The above expression predicts the change of the closed orbit given the introduction of known dipole kicks, such as from dipole corrector magnets. This allows the calculation of dipole kicks required to alter the closed orbit to the desired shape, e.g. to compensate for the closed orbit distortion induced by unknown dipole errors. However, in practice, the closed orbit distortion from a dipole kick is generally found numerically through particle tracking. This has the advantage of being able to include the contributions from higher order magnetic elements, which would have a significant effect at a large enough orbit distortion.

Worth noting in equations (3.21) and (3.27), as well as in the expression for the dispersion function (Eq. (3.17)), is that for a tune approaching an integer, the amplitude of the equilibrium orbit will tend towards infinity. Under these conditions a beam can eventually no longer circulate. The region close to an integer value of the tune

is known as the *integer stopband* and is the lowest order of the transverse *optical resonances*. In a ring with dipole errors there exists no stable solution for a particle with an integer tune. In practice, all rings have some dipole errors, which is why operating on an integer tune value is avoided.

3.2.5 Optical Resonances

The optical resonance present in Eq. (3.27) can easily be intuitively understood. Imagine a particle circulating in an accelerator with an integer betatron tune. At any arbitrary longitudinal position the particle arrives with the same phase every turn. If there is a dipole error present in the accelerator the particle will be deflected into a new orbit, which, at the location of the error, is separated from the old orbit by some non-zero angle. Since the integer betatron tune will ensure that the dipole error always occurs at the same betatron phase, the angular deflection will accumulate linearly with the number of turns until the amplitude of the particle is too large to be contained within the accelerator. Similar to the integer resonance being driven by a dipole error, quadrupole errors drive half-integer resonances (see Fig. 3.2), sextupoles drive third-integer resonances etc.

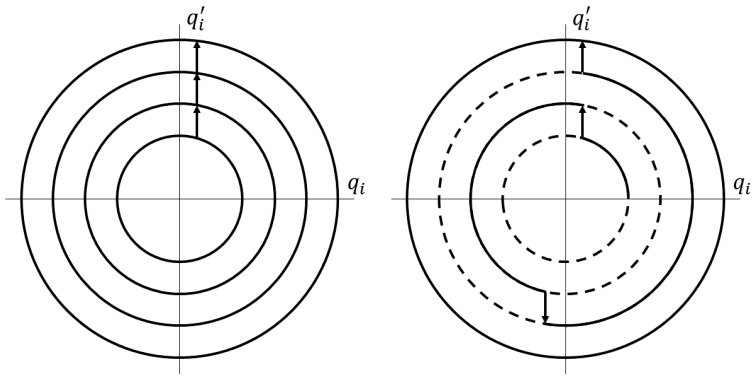

Figure 3.2: Propagation in phase space of a particle in a storage ring. Left: A particle with an integer tune will encounter a dipole error while at the same position in phase space as the previous turn, resulting in constructive interference which increases the amplitude of the particle oscillation with every turn. Right: A particle with a half-integer tune will encounter a quadrupole error while at the opposite position in phase space as the previous turn, resulting in constructive interference which increases the amplitude of the particle oscillation with every turn.

As the order of the optical resonance increases, it becomes more difficult to intuitively understand. In order to get a qualitative understanding of an arbitrary resonance, consider the equation of motion under the influence of a perturbation of an arbi-

trary order. The horizontal equation of motion (Eq. (3.5)), after applying Floquet's transformation (see Appx. A.2), becomes[23]

$$\frac{\mathrm{d}^2 w}{\mathrm{d}\Phi^2} + \nu_{x0}^2 w = \bar{p}_{nr}(\Phi) w^n v^r \tag{3.28}$$

where $w = \frac{x}{\sqrt{\beta_x}}$, $v = \frac{y}{\sqrt{\beta_y}}$, ν_{x0} is the unperturbed horizontal tune, and $\bar{p}_{nr}(\Phi)$ is an arbitrary perturbation periodic in Φ.

In a storage ring, perturbations which depend on the betatron oscillation amplitude in both planes can be present. Thus, the vertical variable v is included in the perturbed horizontal equation of motion. The order of the perturbation in each plane is given by n and r, respectively.

If the perturbations are assumed to be small enough, then w and v can be approximated as the solutions to the unperturbed equation of motion, w_0 and v_0. Each term on the right-hand side of Eq. (3.28) can then be written as the Fourier series

$$\begin{aligned} \bar{p}_{nr}(\Phi) &= \sum_m \bar{p}_{nrm} e^{im\Phi} \\ w^n(\Phi) \approx w_0^n(\Phi) &= \sum_{|l|\leq n} W_l e^{il\nu_{x0}\Phi} \\ v^r(\Phi) \approx v_0^r(\Phi) &= \sum_{|q|\leq r} V_q e^{iq\nu_{y0}\Phi} \end{aligned} \tag{3.29}$$

which results in the equation of motion

$$\frac{\mathrm{d}^2 w_0}{\mathrm{d}\Phi^2} + \nu_{x0}^2 w_0 = \sum \bar{p}_{nrm} W_l V_q e^{i(m+l\nu_{x0}+q\nu_{y0})\Phi} \tag{3.30}$$

where l, m, and q are integers.

From this, the condition for resonance can be easily identified as

$$m + l\nu_{x0} + q\nu_{y0} = \nu_{x0} \tag{3.31}$$

The above derivation can be performed for the vertical equation of motion, resulting in a very similar resonance condition. Combining the two results in a more symmetric condition for resonance given by[23]

$$m\nu_x + n\nu_y = q \tag{3.32}$$

where m, n, and q are now integers, not to be confused with the variables of summation used when deriving this expression.

The order of the resonance is given by $|m| + |n|$. When choosing the working point, i.e. the set of horizontal and vertical tunes (ν_x, ν_y) at which to operate a storage ring, it is important to avoid dangerous resonance lines in order to avoid beam loss, reduction of beam lifetime, or the deterioration of other aspects of beam performance. In Fig. 3.3 the resonance lines of orders up to and including the fifth can be seen. In practice these lines have a certain thickness, rather than being mathematically thin. The thickness is called *stop-band width* and depends on the strength of the resonance [22, 23]. In general, the strength of a resonance line reduces as the order of the line increases. Resonances past a certain order are weak enough that they need not be taken into account when operating a particular storage ring.

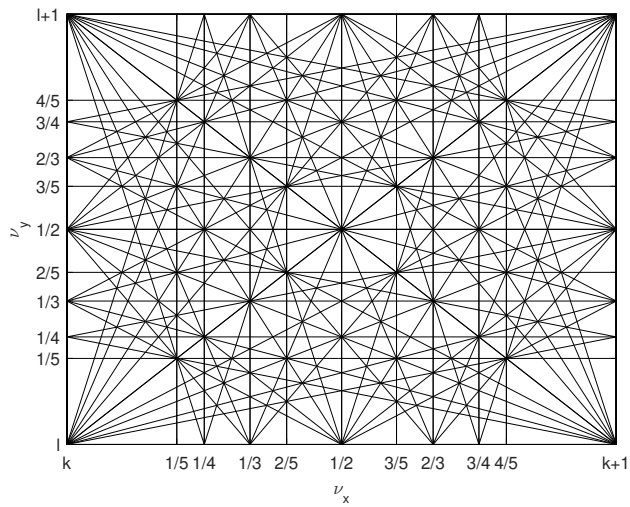

Figure 3.3: Resonance lines of order five and lower. k and l are positive integers corresponding to the integer value of the horizontal and vertical tunes.

3.2.6 Chromaticity

As seen in Sec. 3.2.3, a change in beam momentum results in a change of beam steering from the bending dipoles, which in turn results in a change of closed orbit. The change in momentum also results in a change of beam focussing and a potential subsequent change of betatron tune. This shift in betatron tune, $\Delta\nu_{x,y}$, induced by a relative change in momentum, δ, is called the chromaticity, ξ. We define this quantity as

$$\xi_{x,y} \equiv \frac{\Delta\nu_{x,y}}{\delta} \tag{3.33}$$

The shift in tune can be found by considering the change of focussing given a change in momentum. Limiting the derivation to only the terms linear with δ the changes become

$$\begin{aligned}\Delta k_x =& -(2h^2+k)\delta + (2h^3+m+4hk)\eta\delta - h'\eta'\delta \\ \Delta k_y =& k\delta - (2hk+m)\eta\delta + h'\eta'\delta\end{aligned} \tag{3.34}$$

These terms can be derived from the equations of motion found in Appx. A.1 by considering the closed orbit of an off-nominal momentum beam (see Eq. (3.14)).

In order to find the shift in tune induced by the above change of focussing consider first the shift in tune from a general quadrupole error. This can be derived from the transfer matrix of a thin quadrupole (see Eq. (A.37)) with some quadrupole error Δk, which is given by

$$\mathbf{M}_{quad+error} = \begin{pmatrix} 1 & ds \\ -(K(s)+\Delta k)ds & 1 \end{pmatrix} \tag{3.35}$$

This transfer matrix can to first order in ds be written as

$$\mathbf{M}_{quad+error} = \begin{pmatrix} 1 & 0 \\ -\Delta k ds & 1 \end{pmatrix} \mathbf{M}_{quad} = \mathbf{M}_{error}\mathbf{M}_{quad} \tag{3.36}$$

For a storage ring in which a thin gradient error is present, as defined above, the transfer matrix of a full revolution can be written as the standard full revolution matrix (see Eq. (A.34)) times the error matrix, $\mathbf{M}_{error}$,

$$\mathbf{M}_{error}\mathbf{M}_{s\to s+L} = \begin{pmatrix} \cos\mu + \alpha_{i0}\sin\mu & \beta_{i0}\sin\mu \\ -\Delta k \mathrm{d}s(\cos\mu+\alpha_{i0}\sin\mu) & -\Delta k \mathrm{d}s\beta_{i0}\sin\mu \\ -\gamma_{i0}\sin\mu & +\cos\mu-\alpha_{i0}\sin\mu \end{pmatrix} \tag{3.37}$$

where $\mu = 2\pi\nu_i$ (omitting the subscript i for simplicity), and α_{i0}, β_{i0}, and γ_{i0} are the unperturbed Twiss parameters.

Given a tune shift of $d\nu_i$, i.e. a new tune $\nu_i + d\nu_i$, the full revolution transfer matrix can also be written as

$$\mathbf{M}^*_{s\to s+L} = \begin{pmatrix} \cos\chi + \alpha_i \sin\chi & \beta_i \sin\chi \\ -\gamma_i \sin\chi & \cos\chi - \alpha_i \sin\chi \end{pmatrix} \tag{3.38}$$

where $\chi = 2\pi(\nu_i + d\nu_i)$, once again omitting the subscript i.

Using the similarity of matrices, the traces of $\mathbf{M}_{error}\mathbf{M}_{s\to s+L}$ and $\mathbf{M}^*_{s\to s+L}$ can be equated, resulting in

$$2\cos 2\pi\nu_i - \Delta k ds \beta_{i0} \sin 2\pi\nu_i = 2\cos 2\pi(\nu_i + d\nu_i) \tag{3.39}$$

from which the expression for a small tune shift, $d\nu_i$, given a gradient error, Δk_i, can be found to be

$$d\nu_i = \frac{1}{4\pi}\Delta k_i \beta_{i0} ds \tag{3.40}$$

This relation can now be used to find the tune shifts induced by the quadrupole error defined in Eq. (3.34)

$$\begin{aligned} d\nu_x =& -\delta\frac{1}{4\pi}\big((2h^2+k) - (2h^3 + m + 4hk)\eta + h'\eta'\big)\beta_x ds \\ d\nu_y =& \delta\frac{1}{4\pi}\big(k - (2hk+m)\eta + h'\eta'\big)\beta_y ds \end{aligned} \tag{3.41}$$

By integration we arrive at the expressions for the horizontal and vertical chromaticities:

$$\begin{aligned} \xi_x \equiv \frac{\Delta\nu_x}{\delta} =& -\frac{1}{4\pi}\oint \big((2h^2+k) - (2h^3 + m + 4hk)\eta + h'\eta'\big)\beta_x \mathrm{d}s \\ \xi_y \equiv \frac{\Delta\nu_x}{\delta} =& \frac{1}{4\pi}\oint \big(k - (2hk+m)\eta + h'\eta'\big)\beta_y \mathrm{d}s \end{aligned} \tag{3.42}$$

Assuming a lattice with a large radius of curvature, $h^2 \ll 1$, and no significant combined-function magnets, $hk \approx 0$, and neglecting the derivatives with respect to s, we arrive at the well known result

$$\xi_{x(y)} = \underset{(+)}{-}\frac{1}{4\pi}\oint (k - m\eta)\beta_{x(y)} \mathrm{d}s \tag{3.43}$$

The chromaticity of a storage ring without sextupoles is called the *natural chromaticity*. This chromaticity generally has a large negative value. This means that particles with small shifts in momentum have large shifts in tune and risk encountering dangerous optical resonances. Additionally, a negative chromaticity leads to so called *head-tail instabilities*[24], which might limit the maximum beam current which can be stored in the ring. For these reasons, the chromaticities in both planes, (ξ_x, ξ_y), are generally kept at small positive values. The compensation of the chromaticities is done using sextupole magnets. As seen in Eq. (3.43), these sextupoles have to be placed at locations along the beam orbit with a non-zero horizontal dispersion, $\eta \neq 0$. In order to simultaneously correct both the horizontal and the vertical chromaticity at least two separate groups of sextupoles are required.

3.3 Non-Linear Optics

In this section the beta and dispersion functions introduced in Sec. 3.2, equations (3.8) and (3.17) respectively, will be expanded upon to include some non-linear effects induced by higher order magnets, such as sextupoles and octupoles, as well as higher order contributions from quadrupoles and dipoles. The main focus is what will be referred to as *2nd order optics*, i.e. the lowest order non-linear optics. Here, as in Sec 3.2, the theory is limited to upright magnets and under the assumption that the particle energy is constant.

3.3.1 2nd Order Dispersion

The dispersion function, η, discussed in Sec. 3.2.3 is an important function when characterising the linear optics. This dispersion can also be referred to as the linear dispersion, or the 1st order dispersion, as it describes a change in closed orbit which is linear with δ. In a similar way as to how the 1st order dispersion is used for linear optics characterisation, the 2nd order dispersion can be used for higher order optics characterisation.

The higher order dispersion functions will be defined through the expansion of the dispersion function with momentum

$$\eta = \eta_1 + \eta_2\delta + \eta_3\delta^2 + ... \tag{3.44}$$

where η_1 is the linear dispersion previously denoted η, and η_2 is the 2nd order dispersion. The dispersion can also be expanded to 3rd and higher order, but this thesis will be limited to the 2nd order.

When deriving the 2nd order dispersion the same approach used for deriving the 1st order dispersion can be used. However, higher order terms must be included in the initial equation of motion

$$\begin{aligned} &x'' - h(1+hx) - x'(hx' + h'x) = \\ &(1 - \delta + \delta^2)[-h - (2h^2 + k)x - (h^3 + \frac{1}{2}m + 2hk)x^2 - \frac{1}{2}hx'^2] \end{aligned} \tag{3.45}$$

This equation can easily be derived from the end result in Appx. A.1.

Using the definition of dispersion (see Eq. (3.14)) we can once again separate the equation of motion into terms dependent and independent of x. The part independent of x becomes

$$\begin{aligned} &\eta'' + (h^2 + k)\eta = \\ &h + \Big[- h + (h'\eta' + 2h^2 + k)\eta - (h^3 + \frac{1}{2}m + 2hk)\eta^2 + \frac{1}{2}h\eta'^2\Big]\delta \end{aligned} \tag{3.46}$$

Inserting the expansion of the dispersion from Eq. (3.44) into the above equation, while only retaining terms up to first order in δ, the equation can be separated into

$$\eta_1'' + (h^2 + k)\eta_1 = h \tag{3.47}$$

and

$$\eta_2'' + (h^2 + k)\eta_2 = -h + (h'\eta_1' + 2h^2 + k)\eta_1 - (h^3 + \frac{1}{2}m + 2hk)\eta_1^2 + \frac{1}{2}h\eta_1'^2 \tag{3.48}$$

The first equation is the one used in Sec. 3.2.3 to find an expression for the 1st order dispersion (Eq. (3.16)), while the second can be used in the same way to find the 2nd order dispersion. Using the approach of Floquet's transformation (see Appx. A.2) the 2nd order dispersion becomes

$$\eta_2(s) = \frac{\sqrt{\beta(s)}}{2\sin\pi\nu}\int_s^{s+L}\sqrt{\beta(\sigma)}f\cos\big(\pi\nu + \Psi(s) - \Psi(\sigma)\big)\mathrm{d}\sigma \tag{3.49}$$

where

$$f = -h + (h'\eta_1' + 2h^2 + k)\eta_1 - (h^3 + \frac{1}{2}m + 2hk)\eta_1^2 + \frac{1}{2}h\eta_1'^2 \tag{3.50}$$

Although this expression is a bit cumbersome it reveals two important properties of the 2nd order dispersion which are used in the papers of this thesis: η_2 is linear with chromatic sextupole strengths, m, and independent of magnets of order higher than sextupoles. In particular, these properties are utilised in Paper **I** and Paper **VI**, where the 2nd order dispersion is included in the characterisation of the 2nd order optics of the MAX IV 3 GeV storage ring and the calibration of the chromatic sextupoles.

3.3.2 Chromatic Functions

The Twiss parameters can also be expanded with momentum in a similar manner to the dispersion. Looking at the beta functions in particular, we define the chromatic functions, β_1, as

$$\beta = \beta_0 + \beta_1\delta + ... \tag{3.51}$$

The chromatic functions can be calculated by introducing a linear perturbation, $p(s)$, to the equation of motion of the form

$$q_i''(s) + K(s)q_i(s) = p(s)q_i(s) \tag{3.52}$$

We choose $p(s)$ to be the linear chromatic gradient errors experienced by a particle with a momentum error of δ. These are the same gradient errors used when deriving the expression for the chromaticity in Sec. 3.2.6 (see Eq. (3.34)). The variation of the beta function from a linear perturbation is given by[25]

$$\frac{\Delta\beta(s)}{\beta(s)} = \frac{1}{2\sin 2\pi\nu_0}\oint \beta(\sigma)p(\sigma)\cos\Big[2\big(\pi\nu_0 + \Psi(s) - \Psi(\sigma)\big)\Big]\mathrm{d}\sigma \tag{3.53}$$

where ν_0 is the unperturbed tune.

From the above equation the expression for the chromatic functions can be found to be

$$\beta_1 = \frac{\mathrm{d}\beta(s)}{\mathrm{d}\delta} = \frac{\beta_0(s)}{2\sin 2\pi\nu_0}\oint \beta_0(\sigma)\frac{\mathrm{d}p(\sigma)}{\mathrm{d}\delta}\cos\Big[2\big(\pi\nu_0+\Psi(s)-\Psi(\sigma)\big)\Big]\mathrm{d}\sigma \tag{3.54}$$

where the perturbation $p(s)$ in either plane is given by

$$\begin{aligned} p_x =&(2h^2 + k)\delta - (2h^3 + m + 4hk)\eta\delta + h'\eta'\delta \\ p_y =& - k\delta + (2hk + m)\eta\delta - h'\eta'\delta \end{aligned} \tag{3.55}$$

Similar to the 2nd order dispersion, the chromatic functions in both planes are linearly dependent on chromatic sextupoles. This property is used in Paper **I** when correcting the 2nd order optics of the MAX IV 3 GeV ring using the sextupoles, although through the proxy of the off-energy orbit response to a dipole perturbation.

3.3.3 Amplitude-Dependent Tune Shift

As stated in Sec. 3.2.2, a charged particle travelling through a storage ring performs betatron oscillations. If left undisturbed these oscillations will damp down to a small amplitude through the process of *synchrotron damping*, which will be discussed further in Sec. 3.4. For the MAX IV storage rings the synchrotron damping time is of the order of milliseconds (see Appx. B for further details). However, there are situations where a kick might significantly increase the oscillation amplitude. This might be due to unwanted disturbances, such as ID gap movements, or intentional, such as the disturbance from an injection kicker. The increase in amplitude will cause the beam to pass through higher order magnets transversally off-centre. The feed-down from these magnets cause a tune shift of the oscillating particle, which changes with the amplitude of the oscillation. The tune shift is called an *Amplitude-Dependent Tune Shift* (ADTS), or a *tune shift with amplitude*[25].

The effect on the ADTS from higher order magnets can be derived from the equation of motion in Appx. A.1. Application of Floquet's transformation, derived in Appx. A.2, on the horizontal equation of motion and singling out the most relevant terms results in

$$w'' + \nu_0^2 w = \nu_0^2\beta^2 k\delta w - \nu_0^2\beta^2 m\eta\delta w - \frac{1}{2}\nu_0^2\beta^{5/2} m w^2 - \frac{1}{6}\nu_0^2\beta^3 o w^3 ... \tag{3.56}$$

Here we can identify the first two terms of the right-hand side of the equation as the natural chromaticity and the chromaticity compensation from sextupoles (see Eq. (3.43)). The third and fourth terms are the contributions to the ADTS from the sextupoles and octupoles, respectively[25]. Using the same procedure the corresponding terms in the vertical plane can be found.

The ADTS may cause the horizontal or vertical tune to cross a transverse resonance at a certain betatron oscillation amplitude. If the particular resonance is strong enough

to cause loss of beam it might limit the maximum amplitude of stable betatron oscillations a particle can have while stored in the ring. This limit is known as the *dynamic aperture*. Similar to the physical aperture, particles with an amplitude beyond the dynamic aperture are lost. The dynamic aperture can not be analytically calculated, but needs to be either measured or found trough numerical simulation.

3.3.4 Transverse Acceptance

The transverse emittance limit for which an electron can still be contained within a storage ring is given by[26]

$$A_i = \underset{s}{\text{minimise}}\Big[\frac{(a_i - \eta_i\delta)^2}{\beta_i}\Big] \tag{3.57}$$

where A_i is the transverse acceptance, and a_i is the half aperture which limits the acceptance value.

An off-momentum particle will travel along a dispersive orbit, which brings them closer to the limiting aperture of the ring. As a result, the maximum allowed betatron oscillation amplitude of an off-momentum particle is reduced by the amplitude of the dispersive orbit. The limiting aperture is not necessarily the smallest aperture of the ring, as the value of the beta and dispersion functions also affect the acceptance. Since the dispersion function in the vertical plane is generally zero, the vertical acceptance is momentum independent.

The limiting aperture, a_i, is either a limit in the physical aperture or a limit in the dynamic aperture. The physical aperture refers to physically blocking the beam with e.g. the beam pipe, while the dynamic aperture is a limitation set by the optics of the storage ring.

For linear betatron motion we can easily find the local projection of the acceptance. This is the maximum transverse position a particle can have in a ring without being lost

$$q_i(s) = \pm\sqrt{A_i\beta_i(s)} + \eta_i(s)\delta \tag{3.58}$$

For a ring with significant non-linear elements the dispersion function is dependent on δ, while the beta functions are dependent on both δ and the amplitude of the oscillations. For such a ring Eq. (3.58) no longer applies. The transverse acceptance can instead be found through numerical particle tracking.

3.3.5 Transverse Resonance Island Buckets

A part of the non-linear transverse dynamics which is yet to be discussed in this thesis is the motion of the beam close to a transverse resonance. This is of importance in Paper **IV** where this motion gives rise to *Transverse Resonance Island Buckets*, TRIBs[27].

When investigating the motion of a particle close to a resonance it becomes favourable to switch to a Hamiltonian formulation of the problem. The derivation of such a Hamiltonian will not be done here, but a full derivation can be found in literature[28]. The Hamiltonian of the motion close to the third order resonance under the influence of sextupole fields is given by[28]

$$H = (\nu_i - \frac{m}{3})\jmath - A\jmath^{3/2}\cos(3\psi + \phi_i) + B\jmath^2 \tag{3.59}$$

where m is an integer, A and B are constants set by the lattice structure, and the action-angle variables $(\jmath, \psi)$ are related to the variables of the Floquet's transformation (see Appx. A.2) as

$$\begin{aligned} w =& \sqrt{\frac{2\jmath}{\nu_i}}\cos(\Phi - \phi_i) \\ \dot{w} =& -\sqrt{2\nu_i\jmath}\sin(\Phi - \phi_i) \end{aligned} \tag{3.60}$$

The Hamiltonian describes the total energy of a system, in this case a particle close to the third order resonance. The motion can be investigated qualitatively by plotting the level curves of the Hamiltonian, as can be seen in Fig. 3.4. Here, the choice has been made to transform the level curves back to the more intuitive Cartesian coordinates.

Figure 3.4 shows that the Hamiltonian in Eq. (3.59) gives rise to six additional fix points separated in phase space from the fix point of the regular centre beam. The separatrix around each of the displaced stable fix points will be referred to as *islands*, while the separatrix around the regular beam centre will be referred to as the *core*. A particle placed in the islands or the core will have their motion contained to its separatrix unless it is influenced by other external forces. This allows for independent population of the core and islands.

The islands appear in phase space at the location where the ADTS crosses the resonance. This means that at the location of the island the fractional tune will match the value of the resonance. In the case of the third order resonance, the fractional tune of a particle in the islands is $1/3$. After a full revolution of the ring the particle will have propagated to the position in phase space of the next island. Only after three full

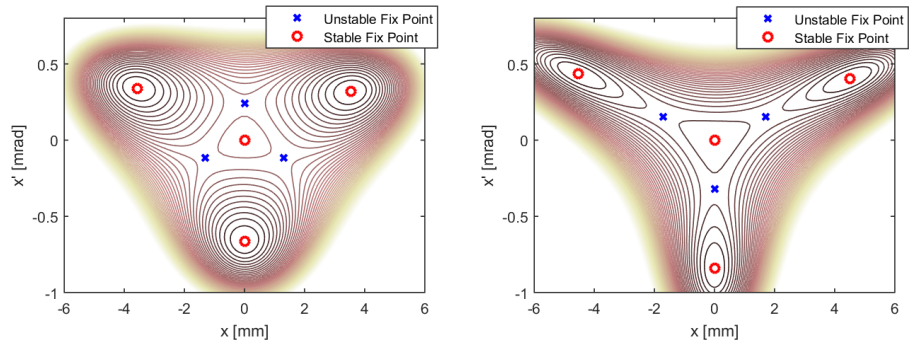

Figure 3.4: Level curves of Eq. (3.59) for two different sets of values for $(\nu_i - m/3)$, A, and B. The action-angle variables have been transformed to x-x' using the values of the optical functions at the centre of a straight section of the 1.5 GeV ring when operating close to a third order resonance. The colour scale indicates the magnitude of the left-hand side of Eq. (3.59) from low (red), to high (yellow).

revolutions will it return to its original position in phase space. This means that all three islands form a single closed orbit which closes only every third revolution. With each of the three turns the particles will travel with different displacement through the magnetic lattice, in comparison to the core orbit. This results in the optical functions of each of the three turns being different from both each other as well as the core.

3.4 Longitudinal Dynamics

Although this thesis is mainly focussed on the transverse dynamics of a storage ring, this section has been included to give a basic understanding of the longitudinal dynamics. This is required to further analyse certain aspects of the performance of a storage ring, such as momentum acceptance and lifetime.

3.4.1 Synchrotron Oscillations

When a relativistic electron travelling through a storage ring has its trajectory deflected by the magnets of the ring it will emit synchrotron radiation. In doing so, the electron will lose some of its energy. If this energy is not replenished the electron will eventually not be able to circulate in the ring. In order to compensate for the energy loss a storage ring has one or more Radio Frequency (RF) cavities in which the lost energy is replenished using an oscillating electric field.

An electron with the nominal energy, E_0, travelling along the ideal orbit will lose some amount of energy each turn, ΔE. The loss of energy is distributed along the orbit at any location where the particle emits synchrotron radiation. If the electron

regains this amount of energy each turn it will continue to circulate along the ideal orbit and is referred to as the *synchronous electron*, or the *synchronous particle*. The longitudinal phase at which this electron arrives at the accelerating cavities is called the synchronous phase, ψ_s. Since this electron needs to regain the same amount of energy each turn, the angular frequency of the accelerating RF, ω_{RF}, needs to be an integer multiple, n_{RF}, of the angular revolution frequency, ω_{rev},

$$\omega_{RF} = n_{RF}\omega_{rev} \tag{3.61}$$

Electrons travelling through a storage ring are generally highly relativistic, thus a slight change of momentum will not significantly change their speed. However, an off-nominal momentum particle will travel along its dispersive orbit. The change in orbit path length given a change in momentum is given by the momentum compaction factor, α, which was previously defined as

$$\alpha \equiv \frac{1}{L_0}\oint \frac{\eta(s)}{\rho(s)}\mathrm{d}s \tag{3.62}$$

Typically, the momentum compaction factor of an electron storage ring is positive[29]. This results in a higher momentum electron taking a longer path in the ring and thus having a lower revolution frequency. This electron will arrive at the cavities later than the synchronous particle, while a lower momentum electron will arrive earlier. For this reason the accelerating RF is designed so that the synchronous electron arrives on the upward slope of the negative part of the oscillating field (see Fig. 3.5). A higher momentum electron will arrive later and thus receive less energy from the cavity, while a lower momentum electron will receive more. Should the synchronous electron instead be defined to arrive on the downwards slope of the RF field, an electron with a momentum deviation from the synchronous electron will have its deviation grow in magnitude with each turn, until the electron is eventually lost. For a positively charged particle, such as a positron, the accelerating field has the opposite sign.

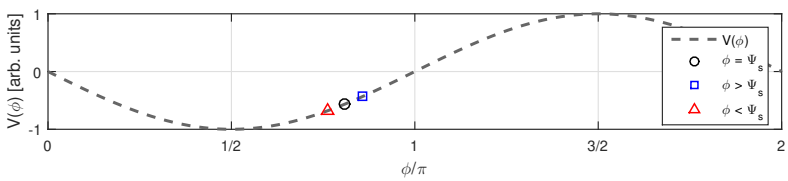

Figure 3.5: The synchronous particle (black circle), a higher energy (blue square), and a lower energy (red triangle) particle. As the higher (lower) energy particle takes a longer (shorter) path around the ring, assuming a positive momentum compaction factor, it will arrive later (earlier) in RF phase than the synchronous particle and thus receive less (more) energy from the accelerating field.

Since particles can only be stably accelerated on one slope of the RF field, the beam travelling through a storage ring is not a continuous stream of electrons, but rather a train of distinct electron *bunches*. The maximum number of electron bunches in a storage ring is given by its number of *RF buckets*, i.e. the number of full oscillations the RF field can perform during one revolution of the ring, n_{RF}, also referred to as the *harmonic number* of the storage ring (see Eq. (3.61)).

Particles with a momentum deviation relative to the synchronous particle will start to oscillate around the synchronous particle in longitudinal phase space. Longitudinal phase space is in this case spanned by the momentum deviation and phase offset of a particle compared to the synchronous particle. These oscillations are called *synchrotron oscillations*, and their frequency is called the *synchrotron frequency*. When written as a fraction of the accelerating frequency the synchrotron frequency is called the *synchrotron tune*.

The equation of motion of a relativistic particle performing synchrotron oscillations is given by[30,31]

$$\frac{\mathrm{d}\phi}{\mathrm{d}t} = -\omega_{RF}\alpha\delta \tag{3.63}$$

$$\frac{\mathrm{d}\delta}{\mathrm{d}t} = \frac{1}{T_0 E_0}(eV(\phi) - U(E)) \tag{3.64}$$

where ϕ is the phase deviation from the synchronous phase, E and E_0 are the energy of the particle and the nominal energy respectively, $T_0 = L_0/\beta c$ is the revolution period (note that here β is the ratio v_s/c, not to be confused with the beta function), $V(\phi)$ is the accelerating voltage seen by a particle with phase deviation ϕ, and $U(E)$ is the energy loss per turn of a particle with energy E.

Assuming small oscillations around the synchronous phase we can expand the accelerating field, keeping only terms linear with ϕ. We can also expand the energy loss around the energy of the synchronous particle resulting in

$$eV(\phi) - U(E) \approx eV(\psi_s) + e\frac{\mathrm{d}V}{\mathrm{d}\phi}\Big|_{\psi_s}\phi - U(E_0) - \frac{\mathrm{d}U}{\mathrm{d}E}\Big|_{E_0}E_0\delta \tag{3.65}$$

For a particle of nominal energy the change of energy with each turn should be zero, $eV(\psi_s) = U(E_0) = U_0$. Differentiating the initial equation of motion (Eq. (3.63)) and using the above approximation results in

$$\frac{\mathrm{d}^2\phi}{\mathrm{d}t^2} + \frac{\omega_{RF}\alpha}{E_0 T_0} e \frac{\mathrm{d}V}{\mathrm{d}\phi}\Big|_{\psi_s} \phi - \frac{\omega_{RF}\alpha}{T_0} \frac{\mathrm{d}U}{\mathrm{d}E}\Big|_{E_0} \delta = 0 \tag{3.66}$$

The equation can now be rewritten as a differential equation of motion valid for small phase oscillations

$$\frac{\mathrm{d}^2\phi}{\mathrm{d}t} + 2\alpha_z \frac{\mathrm{d}\phi}{\mathrm{d}t} + \Omega^2 \phi = 0 \tag{3.67}$$

where α_z is the *damping decrement* defined by

$$\alpha_z \equiv \frac{1}{2T_0} \frac{\mathrm{d}U}{\mathrm{d}E}\Big|_{E_0} \tag{3.68}$$

and Ω^2 is the square of the synchrotron frequency

$$\Omega^2 = \frac{\omega_{RF}\alpha}{E_0 T_0} e \frac{\mathrm{d}V}{\mathrm{d}\phi}\Big|_{\psi_s} \tag{3.69}$$

The particles orbiting the ring oscillate in the longitudinal plane with the frequency Ω. The oscillations are either damped or antidamped depending on the sign or α_z. The synchrotron radiation emitted by the particles have a damping effect on both the longitudinal and transverse oscillations known as synchrotron damping. This occurs because the synchrotron radiation is emitted along the instantaneous direction of motion of the particle, causing its momentum to decrease both longitudinally and transversally. In the longitudinal plane this momentum is replenished by the RF-cavities, while in the transverse plane the loss of momentum leads to a damping of the betatron motion[32]. The damping time from this effect is generally much longer than the period of the longitudinal oscillations, which allows further treatment of the longitudinal oscillations to ignore the damping. Due to effects described in Sec. 3.5 the longitudinal oscillations never damp down to zero.

In order to investigate the stability of the longitudinal motion an assumption must be made regarding the waveform of the accelerating voltage. Assuming the accelerating voltage can be expressed as a sinusoidal

$$V(\phi) = V_0 \sin\phi \tag{3.70}$$

the synchrotron oscillation frequency squared becomes

$$\Omega^2 = \frac{\omega_{RF}\alpha}{E_0 T_0} e V_0 \cos\psi_s \tag{3.71}$$

The equation of motion without damping is

$$\frac{\mathrm{d}^2\phi}{\mathrm{d}t} + \Omega^2\phi = 0 \tag{3.72}$$

which is a harmonic oscillator with stable oscillations if the oscillation frequency $\Omega > 0$. From Eq. (3.71) we get that ψ_s has to be chosen so that $\cos\psi_s > 0$, which for a positive value of $V(\phi)$, results in $0 < \psi_s < \pi/2$. For the energy of the synchronous particle to not change it is required that $eV_0 \sin\psi_s = U_0$ which ultimately results in the expression for the synchronous phase[30]

$$\psi_s = \arcsin\frac{U_0}{eV_0} \tag{3.73}$$

The MAX IV storage rings utilise passive harmonic cavities in addition to the active accelerating cavities. These operate at a higher resonant frequency, relative to the accelerating cavities, with the purpose of mitigating instabilities through bunch lengthening and synchrotron tune spread[33]. The addition of the fields from the harmonic cavities means that the accelerating voltage no longer can be described as the simple sinusoidal in Eq. (3.70). However, at a sufficiently low stored current the induced field in the harmonic cavities is low enough that total accelerating voltage can be approximated as a sinusoidal. This can also be achieved by sufficiently detuning the harmonic cavities from the resonance frequency.

3.4.2 Beam Lifetime

The number of electrons stored in a storage ring is quantified by the *beam current* passing a cross section of the beam pipe at any longitudinal position. Through a number of different processes the beam loses electrons and thus the beam current decays. The measurement of the current loss over time is called the *beam lifetime*.

The loss of electrons are due to single particle processes, which leads to an exponential decay of the beam current with time, and two particle processes, which leads to a hyperbolic decay. Combining the two processes leads to the expression for the total number of particles at time t[34]

$$N = N_0 \frac{e^{-t/\tau_1}}{1 + (1 - e^{-t/\tau_1})\frac{\tau_1}{\tau_2}} \tag{3.74}$$

where N_0 is the initial number of particles, T_1 is the exponential beam lifetime, and T_2 is the hyperbolic beam lifetime. By replacing N and N_0 with the beam current, I,

and the initial beam current, I_0, the same expression can be used for the beam current decay.

When letting T_1 go to infinity in Eq. (3.74) the expression becomes that of a purely hyperbolic decay, while letting T_2 go to infinity results in an exponential decay. For relatively short time intervals, such as the time window used to measure the lifetime, we can simply add the loss rates of the different lifetime contributions. The total lifetime becomes[34]

$$\frac{1}{\tau} = \sum_n \frac{1}{\tau_n} \tag{3.75}$$

Two important contributions to the electron beam lifetime are the *gas lifetime*, and the *Toucschek scattering lifetime*, the latter of which is discussed further below. The gas lifetime is a combination of scattering processes in which electrons from the beam interact with residual gas molecules in the vacuum chamber. These include elastic and inelastic scattering against both gas nuclei and electrons.

Touschek Scattering Lifetime

When many electrons travel in small bunches there is an increased probability of elastic collisions between two electrons. The probability is increased further due to the transverse (betatron) and longitudinal (synchrotron) oscillations performed by the electrons. Should the collision of two electrons be such that there is a momentum transfer from the transverse motion to the longitudinal, it can result in a large change of energy due to relativistic effects, and may lead to the loss of the particles[35]. Such a collision will be referred to as a *Touschek event*. If a Touschek scattered particle is lost it is always due to the transfer of momentum to the longitudinal plane exceeding the momentum acceptance. The limiting momentum acceptance is set by either the RF-bucket momentum acceptance, or the lattice momentum acceptance. In the former case the limit is uniform throughout the ring, while in the latter case the limit depends on the s-coordinate. The decay rate from Touschek scattering is proportional to the number of particles in the bunch, thus the decay is hyperbolic and the decay time constant is given by[36]

$$\frac{1}{\tau} = \frac{r_e^2 c q}{8\pi e \gamma_L^3 \sigma_s} \frac{1}{L} \oint \frac{F([\delta_{acc}(s)/\gamma\sigma_{x'}(s)]^2)}{\sigma_x(s)\sigma_y(s)\sigma_{x'}(s)\delta_{acc}^2(s)} \mathrm{d}s \tag{3.76}$$

where r_e is the classical electron radius, q is the bunch charge, σ_s is the bunch length, σ_x and σ_y are the horizontal and vertical beam sizes, γ_L is the Lorentz factor of the

electrons, $\sigma_{x'}$ is the beam divergence at $x \approx 0$, δ_{acc} is the local relative momentum acceptance set by the RF-system or the lattice, and $F(x)$ is the function defined by

$$F(x) = \int_0^1 (\frac{1}{u} - \frac{1}{2}\ln\frac{1}{u} - 1)e^{-x/u}\mathrm{d}u \tag{3.77}$$

The Touschek lifetime's dependence on the momentum acceptance is used in both Paper **I** and Paper **III** to measure how the momentum acceptance changes with different magnet settings.

3.4.3 Lattice Momentum Acceptance

Particles which experience a Touschek event are more likely to be from the centre of the beam where the particle density is high. After the event the particles are still on the nominal on-momentum orbit, but their equilibrium orbit is now the dispersive orbit of a particle with a relative momentum error of δ. They are displaced from their dispersive orbit by an amplitude of $-\eta(s_0)\delta$, where s_0 is the longitudinal position of the Touschek event, and will start performing betatron oscillations with this amplitude around the dispersive orbit. The particle oscillation envelope is given by[36,37]

$$q_{i,max}(s) = \eta_i\delta + \sqrt{\beta_i(s)\mathscr{H}_i(s_0)}\delta \tag{3.78}$$

where

$$\mathscr{H}_i(s) = \gamma_i(s)\eta_i^2(s) + 2\alpha_i(s)\eta_i(s)\eta_i'(s) + \beta_i(s)\eta_i'^2(s) \tag{3.79}$$

If the lattice is such that the optical functions (α, β, γ, η) are not significantly different with for a particle with a momentum error of δ, then Eq. (3.78) gives us the lattice momentum acceptance at the location s_0[36]

$$\delta_{acc}(s_0) = \underset{s,i}{\text{minimise}}\Big[\frac{a_i}{\sqrt{\mathscr{H}_i(s_0)\beta_i} + \eta_i}\Big] \tag{3.80}$$

where a_i is the limiting aperture, at some longitudinal position, in plane i, either due to a physical aperture or the dynamic aperture. Since the vertical dispersion is generally zero, this limiting aperture is most often in the horizontal plane.

In a modern synchrotron, such as the MAX IV synchrotrons, the strong focussing leads to a large natural chromaticity which needs to be corrected with strong sextupoles. These sextupoles, and higher order magnets, contribute with a significant non-linearity to the beam optics, some of which has been explained in more detail

in Sec. 3.3. In short, the dispersive orbit is no longer linearly dependent on δ, while the Twiss parameters are dependent on both δ and the amplitude of the betatron oscillation. Due to these complex dynamics introduced by non-linear magnets the momentum acceptance of such a lattice is generally found through numerical particle tracking by investigating whether a pair of particles with a momentum deviation $\pm\delta$ at a starting location s are contained within the ring for a sufficient number of turns or not.

3.4.4 RF Momentum Acceptance

The maximum allowed momentum deviation of a particle may not only be limited by the lattice, but also by the RF cavities. Assuming an accelerating voltage given by a pure sinusoidal (see Eq. (3.70)) and that the energy loss per turn is much smaller than the nominal energy of the beam ($U_0 \ll E_0$) the RF momentum acceptance is given by[36]

$$\delta_{acc}^{RF} = \sqrt{\frac{2U_0\lambda}{\pi E_0 \alpha_c L}(\cot\psi_s + \psi_s - \frac{\pi}{2})} \tag{3.81}$$

where λ is the RF wavelength.

The criterion $U_0 \ll E_0$ is is fulfilled by both the 1.5 GeV and 3 GeV storage rings which have a bare lattice radiation loss per turn of $117.2\,\mathrm{keV}$ and $360.0\,\mathrm{keV}$, respectively.

Together with the derived expression for the synchronous phase of a purely sinusoidal accelerating field (see Eq. (3.73)), Eq. (3.81) results in an increase in RF momentum acceptance as the accelerating voltage, V_0, increases. This property is used in Paper **I** as a way of probing the lattice momentum acceptance. By decreasing the momentum acceptance using the accelerating voltage until the lifetime is affected, the point has been found where the momentum acceptance of the storage ring is limited by the lattice rather than the RF cavities. From the value of V_0 at which this transition happens the lattice momentum acceptance can be calculated.

3.5 Equilibrium Beam Emittance

The emittance of synchrotron radiation does not only lead to a transverse damping effect, in the from of synchrotron damping (see Sec. 3.4.1), but the same process of emitting synchrotron radiation can also excite betatron oscillations. When a photon is emitted from an electron travelling on the nominal orbit it will loose some

momentum. Similarly to the case of a Touschek-scattered particle (see Sec. 3.4.2), the equilibrium orbit of this particle is now the dispersive orbit as given by $\eta\delta$. The particle is displaced from this orbit and will begin performing betatron oscillations resulting in an increase in the single-particle emittance

$$\varepsilon_i = \big(\gamma_i(s_0)\eta_i^2(s_0) + 2\alpha_i(s_0)\eta_i(s_0)\eta_i'(s_0) + \beta_i(s_0)\eta_i'^2(s_0)\big)\delta^2 = \mathscr{H}_i(s_0)\delta^2 \tag{3.82}$$

where s_0 is the point of photon emission.

The emittance of the entire beam will reach an equilibrium when the excitation and damping from the photon emission reach equal strength. In order to calculate this equilibrium emittance is necessary to average over all possible photon energies and emission probabilities. In the case of a ring where the bending only occurs in the horizontal plane, as is the case for most rings, there is a non-zero horizontal dispersion function. This results in a horizontal beam emittance given by[32]

$$\varepsilon_x = \frac{55}{32\sqrt{3}}\frac{\hbar c}{m_0c^2}\gamma^2\frac{\langle h^3\mathscr{H}_x\rangle}{J_x\langle h^2\rangle} \tag{3.83}$$

where $\hbar$ is the reduced Planck constant (not to be confused with the dipole part of the magnetic multipole expansion, $h = 1/\rho$, the angle brackets represent an averaging over the circumference of the ring, $\langle f(s)\rangle = \frac{1}{L}\oint f(s)\mathrm{d}s$, and J_x is the *horizontal damping partition number* given by[9,32]

$$J_x = 1 - \frac{\oint h\eta_x(2k + h^2)\mathrm{d}s}{\oint h^2\mathrm{d}s} \tag{3.84}$$

From Eq. (3.82) it would seem that there is no lower limit of the vertical beam emittance. However, if we take into account that the synchrotron radiation is emitted in a cone with an angular spread of $\pm 1/\gamma$ there will be some recoil on the particle orthogonal to the particle trajectory, which includes the vertical plane. This effect is significantly smaller than the preciously mentioned effect, which defined the horizontal emittance, and could therefore be safely neglected from this calculation. The lower limit of the vertical beam emittance is given by[32]

$$\varepsilon_y = \frac{55}{32\sqrt{3}}\frac{\hbar c}{m_0c^2}\frac{\bar{\beta}_y}{2J_y}\frac{\langle h^3\rangle}{\langle h^2\rangle} \tag{3.85}$$

where $\bar{\beta}_y$ is the average of the vertical beta function, and $J_y = 1$ is the *vertical damping partition number*.

The lower limit of the vertical beam emittance is significantly smaller than the emittance achieved in a real ring[32]. Due to unavoidable vertical dipole errors a non-zero spurious dispersion function appears in the vertical plane. This vertical dispersion contributes to a vertical emittance increase in the same way as was shown for the horizontal case. By changing the subscripts $x \rightarrow y$, Eq. (3.83) also applies for the vertical plane. Additionally, a fraction of the emittance from the horizontal plane can be coupled to the vertical plane by skew quadrupoles, either intentionally or from magnet errors[22]. The emittance coupling of a storage ring is given by

$$\kappa = \varepsilon_y / \varepsilon_x \tag{3.86}$$

The emittance value is also affected by *intrabeam scattering*, IBS. Similar to Touschek scattering, IBS is an instance of coulomb scattering between the particles in the beam. However, the momentum transfer of IBS is small and does not lead to beam loss, but rather increases the beam energy spread and beam size. In a synchrotron, this effect is counteracted by the radiation damping and leads to a new equilibrium emittance. The effect of IBS is generally small, but in a low emittance light source it is not negligible[38].

3.6 Beam Diagnostics

This section aims to give an overview of the two systems of beam diagnostics which were heavily used in the work presented in this thesis: the *beam position monitor*, and the *diagnostic beamline*.

3.6.1 Beam Position Monitor

The arguably most important beam diagnostics tool for transverse optics studies in a storage ring is the beam position monitor, or BPM. As the name suggests the BPM is able to measure the transverse beam position of the electron beam.

The BPM pickup consists of four electrodes inside the vacuum chamber. These are arranged symmetrically around the beam axis at some longitudinal position in the ring. Their placement is generally around $45°$ from the horizontal plane in order to avoid being exposed to synchrotron radiation, which could otherwise lead to systematic measurement errors or even damage to the electrodes.

As the electron beam passes the BPM, a signal is induced on the electrodes. Pickup electrodes cannot in general sense a static electric or magnetic field, instead the signal is induced by the modulation of the passing beam current, i.e. the longitudinal bunching of the stored beam. The strength of the induced current has the approximate proportionally $I_{ind} \propto 1/r$, where r is the distance from the beam to the electrode. This approximation assumes the beam displacement and the beam size to be small compared to r. The horizontal and vertical beam positions may be determined using the relations:

$$\begin{aligned} \Delta x &= K_x \frac{(I_1 + I_4) - (I_2 + I_3)}{\sum_i I_i} \\ \Delta y &= K_y \frac{(I_1 + I_2) - (I_3 + I_4)}{\sum_i I_i} \end{aligned} \tag{3.87}$$

where K_x and K_y are calibration constants which depend on the BPM geometry, and I_1 - I_4 are the signals induced in each BPM electrode. Here, the BPM electrodes are numbered as seem in Fig. 3.6.

In the case where the beam passes through the centre of the BPM, the four electrode signals should be identical. Due to imperfections of the electrode, the BPM geometry, the cabling and the electronics of the BPM, this is rarely the case. A mismatch in signal will linearly affect the beam position from the BPM resulting in a non-zero position reading from a centred beam. This offset in beam position is called the *BPM offset*.

The BPM offset can be measured using a beam-based calibration method where the centre of an adjacent quadrupole magnet is taken as the nominal orbit reference[39]. The beam is placed at a number of positions in the BPM (and consequently in the quadrupole), either horizontally or vertically depending on which offset is to be measured. For each position the strength of the quadrupole is changed by a known amount. The change in closed orbit induced by the change in quadrupole strength will depend linearly on the displacement of the beam relative to the centre of the quadrupole. From the changes of the closed orbit at the different beam positions it is possible to find the beam position where the orbit is unaffected by the change of quadrupole strength. This corresponds to the beam passing through the centre of the quadrupole and is used as the zero orbit reference for the adjacent BPM.

The 2nd order optics of the MAX IV 3 GeV storage ring is investigated using the NOECO scheme (Non-linear optics from Off-Energy Closed Orbits, Paper **I**). This method relies on the effect a chromatic sextupole has on the position of an off-energy beam. The effect is relatively small and thus requires a significant shift of the beam

energy to be accurately measured. This corresponds to a large beam displacement in the BPMs, at which point the approximation $I_{ind} \propto 1/r$ and and the simple linear relation in Eq. (3.87) no longer holds. In order to get accurate beam position readings at large beam displacements we require a higher order function which maps the BPM readings to the actual position of the beam in the BPM. Such a function can easily be found if we know how a sufficiently dense grid of beam positions maps to the BPM reading for each position.

The map from beam position to BPM reading can be measured by stretching a RF-excited wire at different positions through the BPM and monitoring the electrical response. Naturally, this method cannot be used without removing the BPM from the accelerator. A less invasive method is the theoretical determination of the map. This can be done by viewing the beam passing through the BPM as an electrostatic problem defined within the closed boundary set by the beam pipe. A full derivation of this method can be found in a DAΦNE technical note [40], in which the BPM geometry is reduced to two dimensions and solved using a boundary element method. The problem can be represented by the matrix equation

$$\mathbf{G}\sigma + \mathbf{B} = 0 \tag{3.88}$$

where σ is the vector containing the induced charge, σ_n, for all line elements in the BPM geometry, **G** is the matrix with elements given by

$$G_{mn} = \begin{cases} -\ln|\mathbf{r}_m - \mathbf{r}_n| \cdot l_n & \text{if } m \neq n \\ 2(1 - \ln(l_m)) \cdot l_m & \text{if } m = n \end{cases} \tag{3.89}$$

and **B** is the column vector with elements

$$B_m = \ln \frac{1}{|\mathbf{r}_0 - \mathbf{r}_m|} \tag{3.90}$$

where $\mathbf{r}_0$ is the position of the beam, and $\mathbf{r}_m$ and l_m are the centre and the length of the mth line element, respectively.

The matrix equation can be solved for σ by inverting the **G** matrix. The charge induced in every electrode can be found by computing the sum $\sum_k \sigma_k \cdot l_k$ over all elements belonging to the electrode of interest (see Fig. 3.6). This charge can be used in place of the current in Eq. (3.87) to calculate the beam position perceived by the BPM for any given true beam position, $\mathbf{r}_0$. Performing this calculation for grid of beam positions allows the fitting of polynomial maps from 'beam position perceived by the BPM' to 'true position of the electron beam'. A grid of simulated beam positions and the corresponding simulated BPM readings can be seen in Fig. 3.6.

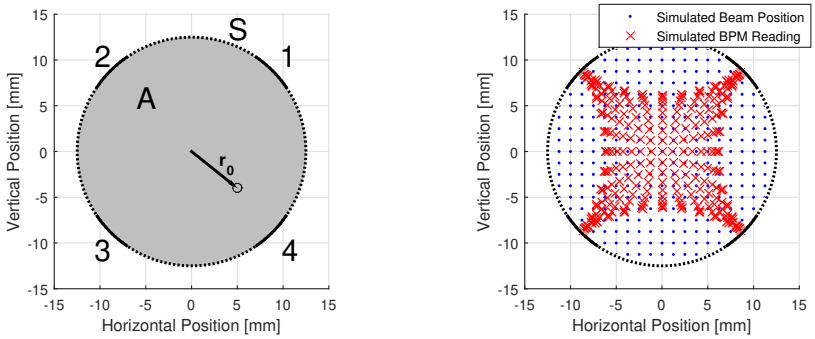

Figure 3.6: Left: Cross section of BPM model with circular geometry. The electrodes are indicated by the numbers 1-4. This model is a good approximation of the BPMs of the MAX IV 3 GeV storage ring, and was used for the linearisation calculation. Right: 'Simulated Beam Position' and corresponding 'Simulated BPM Reading' when accounting for the non-linearities of the BPM. The deviation between the real and perceived beam position becomes smaller as the beam position approaches the centre of the BPM.

3.6.2 Diagnostic Beamline

The 3 GeV Storage Ring Diagnostic Beamlines

The MAX IV 3 GeV storage ring has two diagnostic beamlines. These take light from dipole 1 and 6 in achromat 20 and 2, respectively. The two beamlines are at locations with close to zero and non-zero dispersion, allowing for the measurement of both the transverse beam sizes and the energy spread of the beam.

Both beamlines focus the 488 nm π-polarised SR onto a CMOS camera using a fused silica plano-convex lens. A wavelength filter and a Glan-Taylor polariser are placed just before the image plane to select the desired wavelength and polarisation. In order to protect the beamline optics from powerful X-rays, a thin absorber is placed upstream of the lens. A horizontal and vertical diffraction obstacle is placed downstream of the lens, resulting in a diffraction pattern on the camera. This pattern is used to calculated the horizontal and vertical beam sizes, as described for the vertical plane in the paper by Breunlin et al.[41] A schematic side view of the diagnostic beamlines in the MAX IV 3 GeV storage ring can be seen in Fig. 3.7[42].

The 1.5 GeV Storage Ring Diagnostic Beamlines

The MAX IV 1.5 GeV storage ring has two diagnostic beamlines. These take light from the same bending dipole in achromat 5, but have source points which are separated longitudinally. The two source points are at locations with non-zero and close to zero dispersion allowing the measurement of both the transverse beam sizes and the energy

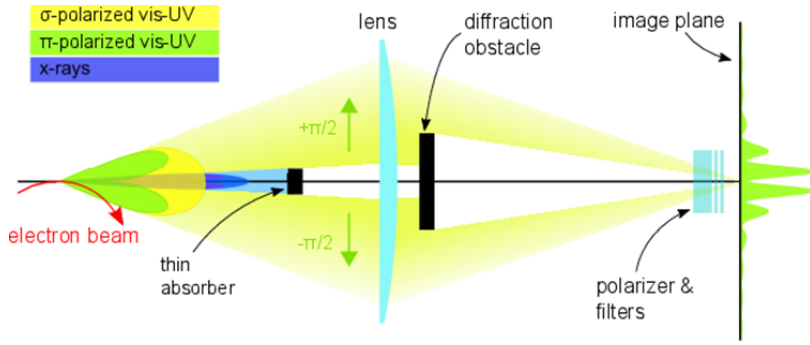

Figure 3.7: Schematic side view of the diagnostic beamlines of the MAX IV 3 GeV storage ring.

spread of the beam.

The beamlines image the cross-section of the electron beam onto a camera CMOS detector using a fused silica plano-convex lens. The beam image is angle independent as long as the dipole radiation is emitted within the horizontal acceptance of the beamline. These acceptances are 6.78 mrad and 4.85 mrad, respectively, and are set by movable baffles at the position of the lens. Wavelengths of 632 nm and 730 nm, respectively, are selected using a narrow bandpass filter, while a Glan-Taylor polarizer is used to select the π-polarised component of the light. The resulting beam image has an upper and lower intensity peak which are used to calculate the vertical beam size. More details on how this calculation is performed can be found in the paper by Andersson et al. [43] The horizontal beam size is found through the fitting of a Gaussian distribution to the horizontal beam profile. The hard X-rays emitted in the forward direction of the beam are blocked by a horizontal absorber before the first mirror in order to reduce the heat load. A schematic side view of the vertical imaging of the diagnostic beamlines in the MAX IV 1.5 GeV storage ring can be seen in Fig. 3.8 [42].

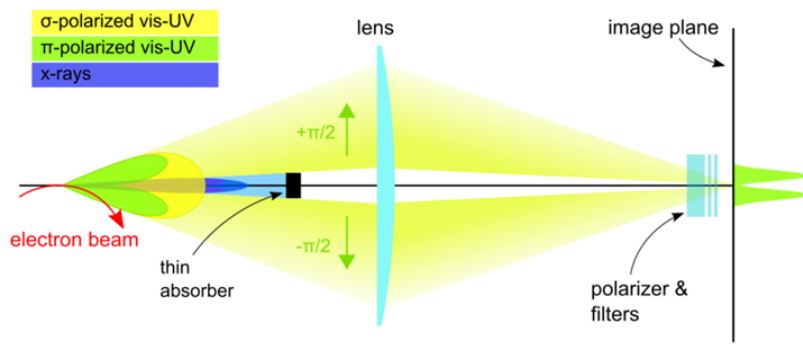

Figure 3.8: Schematic side view of the vertical imaging of the diagnostic beamlines of the MAX IV 1.5 GeV storage ring.

The diagnostic beamlines of the 1.5 GeV ring are not only important for measuring the beam sizes and energy spread, but also for measuring the island population and the separation between islands during TRIBs experiments, as can be seen in Paper **IV**.

Chapter 4

Optics Calibration

This chapter describes methods used to calibrate the optics of a storage ring. Specifically, the well established *Linear Optics from Closed Orbits* scheme[44], and the novel *Non-linear Optics from off Energy Closed Orbits* scheme presented in Paper **I**. Both of these schemes rely on a model of the lattice, and numerical particle tracking. In the case of the work presented in this thesis this was done using *Accelerator Toolbox*[45].

4.1 Linear Optics from Closed Orbits

Before the contents of Paper **I** can be analysed it is important to know the state of the linear optics of the MAX IV 3 GeV storage ring prior to the measurements. This applies to most measurements or experiments concerning higher order optics. In many synchrotron light sources around the world, including the MAX IV storage rings, the standard method for characterising and symmetrising the linear optics is Linear Optics from Closed Orbits, or LOCO[44]. In this section follows a short description of the LOCO scheme as well as the results of applying LOCO to the 3 GeV storage ring, which corresponds to the state of the linear optics prior to the measurements in Paper **I**.

4.1.1 The Orbit Response Matrix

The LOCO scheme uses a measurement of the *Orbit Response Matrix*, ORM, and the linear dispersion, η_1, to characterise the linear optics of a storage ring. The ORM is the closed orbit distortion induced by each dipole corrector as measured by each

$$\begin{pmatrix} x \\ y \end{pmatrix} = M_{ORM} \begin{pmatrix} \theta_x \\ \theta_y \end{pmatrix} \tag{4.1}$$

where θ_x and θ_y are column vectors consisting of the kick strengths of each dipole corrector magnet, and x and y are column vectors consisting of the corresponding horizontal and vertical closed orbit in each BPM given the dipole corrector kicks.

Thus, this matrix has a number of rows equal to twice the number of BPMs, in order to account for both horizontal and vertical beam positions, and a number of columns equal to the number of dipole corrector magnets. The measured lattice dispersion is appended to the matrix with an appropriate weight, forming the final matrix used for linear optics characterisation by the LOCO scheme.

The magnitude of the dipole corrector kicks, θ, used to measure the ORM should be as small as possible to reduce the influence of higher order magnets, such as sextupoles and octupoles. The lower limit of the kick strengths is set by the noise level of the beam position measurement.

4.1.2 Linear Optics Characterisation

The LOCO procedure minimises the difference between the measured ORM and the ORM of a fitted model

$$\chi^2 = \sum_{ij} \frac{(M_{model,ij} - M_{meas,ij})^2}{\sigma_i^2} \tag{4.2}$$

where σ_i is the noise level of the ith BPM.

The minimisation is performed using a Gauss-Newton, or similar, minimisation method where the minimisation parameters are parameters of the model of the machine. The parameters are chosen by the user, but generally includes the quadrupole magnet strengths, as well as the BPM gains and dipole corrector kick strengths. These parameters have a significant impact on the ORM. Post minimisation, the model will have beta and dispersion functions which match the measured data as closely as possible given the fitting parameters.

The LOCO procedure cannot guarantee that the model it arrives at is a good representation of the machine. Any errors which affect the ORM but are not included in the fitting parameters will be attributed to the available parameters, if possible. Simultaneously, it is important to not include too many fitting parameters as to avoid

singularities in the fitting procedure. These can lead to incorrect or even non-physical parameter values, as moving in certain directions in parameter space may not affect the model ORM.

4.1.3 Linear Optics Correction

Once the model ORM has converged to the measured ORM the resulting parameter values can be used to calculate new settings, e.g. for the quadrupole magnet strengths. These can be applied to the machine to correct its linear optics (Twiss parameters and dispersion) towards that of the goal model. The choice of fitting parameters will not necessarily correspond to the true sources of error. Instead, the LOCO fit will attribute the source of the error to a nearby fitting parameter. For instance, if the strength of the quadrupoles are part of the fitting parameters, an undesired quadrupole field in a dipole bending magnet will be attributed to nearby quadrupole magnets. This makes the LOCO model less representative of the machine, but it allows the calculation of new quadruple settings which can compensate for the quadrupole field in the bending dipole. Such a setting might be desirable as it may not be possible to correct a quadrupole error in a dipole magnet using the dipole magnet itself, but the effect of the error can be compensated using nearby quadrupole magnets.

Since the new parameters settings calculated by LOCO might correct errors in the linear optics indirectly, it is generally not sufficient to calculate and apply new settings once. Using an iterative approach of alternating LOCO measurements and corrections, the scheme reaches convergence when the errors present in the machine cannot be corrected further given the choice of fitting parameters. At this point the difference between the measured and model ORM should ideally be only BPM measurement noise.

The beta functions of the MAX IV 3 GeV ring and their beta-beat after a few iterations of LOCO corrections can be seen in Fig. 4.1. The corresponding 1st order dispersion can be seen in Fig. 4.2. The remaining peak-to-peak beta-beat was $2.5\,\%$ horizontally and $1.8\,\%$ vertically, while the residual peak-to-peak dispersion was $0.6\,\mathrm{mm}$ horizontally and $4\,\mathrm{mm}$ vertically. This is the level of beta-beat and dispersion residual the ring has during standard delivery and is comparable to the state of the linear optics presented in Paper **II**, in addition to being the state of the linear optics when the NOECO scheme was first applied to the ring (see Paper **I**).

In addition to the linear optics correction, LOCO is also used to correct the coupling and vertical dispersion of the 3 GeV ring. This is done simultaneously as the linear optics correction by including skew quadrupoles in the fitting parameters. These skew fields are achieved through additional trim coils on sextupoles and octupoles

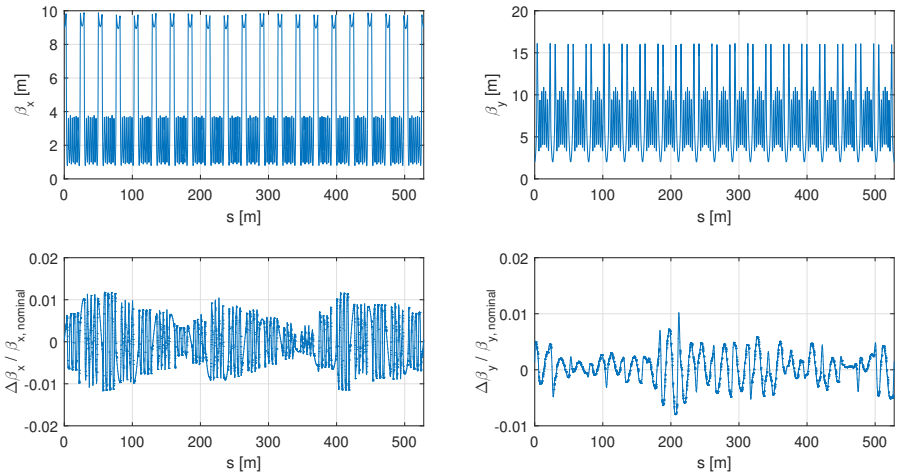

Figure 4.1: Horizontal (top left) and vertical (top right) beta functions of the MAX IV 3 GeV storage ring after correcting the linear optics using LOCO. The corresponding beta-beats can be seen in the bottom two plots. Data from 2022-03-14.

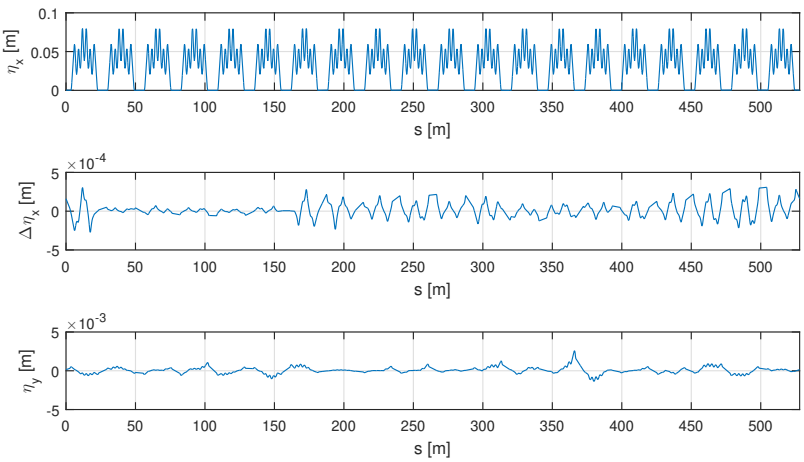

Figure 4.2: Horizontal dispersion (top), horizontal dispersion residual (middle), and vertical dispersion (bottom) of the MAX IV 3 GeV storage ring after correcting the linear optics using LOCO. Since the nominal vertical dispersion is zero, the vertical residual has been omitted. Data from 2022-03-14.

(see Appx. B.1). The goal value of the coupling correction is zero. However, after the lattice has been corrected using LOCO, the coupling is increased by uniformly increasing the strength of harmonic skew quadrupoles. This is done in order to increase the beam lifetime, while keeping the vertical emittance below its goal value of

8 pmrad[46].

4.2 Non-linear Optics from Off-Energy Closed Orbits

This section summarises the design of the Non-linear Optics from Off-Energy Closed Orbits (NOECO) scheme, as well as its deployment on the MAX IV 3 GeV storage ring. The aim was to create a standardised scheme for characterising and symmetrising the 2nd order optics of a storage ring, in a similar way to how LOCO has become the standardised way to correct the linear optics. The increase in machine performance, as well as the limitations of the scheme are discussed.

4.2.1 The Off-Energy Orbit Response Matrix

The NOECO scheme uses a principle similar to that of LOCO, but instead of investigating the effect of the quadrupole gradients on the nominal momentum orbit response it investigates the chromatic gradient errors experienced by a beam with a momentum deviation δ, as given by Eq. (3.34), and how these affect the orbit response of such a beam. Of particular interest is the $m\eta\delta$ term since it allows the correction of the chromatic gradient without affecting the settings of lower order magnets used to correct the linear optics.

Analogously to the LOCO scheme, the NOECO scheme uses a measured *Off-Energy Orbit Response Matrix*, OEORM, and 2nd order dispersion, η_2, to characterise the 2nd order optics of the ring. The OEORM is defined as

$$M_{OEORM} = \frac{(M_{ORM,+\delta/2} - M_{ORM,-\delta/2})}{\delta} \tag{4.3}$$

where $M_{ORM,\pm\delta/2}$ is the ORM measured at a momentum error of $\pm\delta/2$.

Equivalently, the OEORM is also given by

$$\begin{pmatrix} x_{+\delta/2} - x_{-\delta/2} \\ y_{+\delta/2} - y_{-\delta/2} \end{pmatrix} = M_{OEORM}\delta \begin{pmatrix} \theta_x \\ \theta_y \end{pmatrix} \tag{4.4}$$

where $x_{\pm\delta/2}$ and $y_{\pm\delta/2}$ are the column vectors consisting of the horizontal and vertical closed orbit of a beam with a momentum error $\pm\delta/2$ while affected by the dipole corrector kicks given by θ_x and θ_y.

Determination of Measurement Parameters

Before the OEORM of the MAX IV 3 GeV storage ring was measured, an investigation was done to find a good choice of the measurement parameters δ and θ. The value of the momentum shift, δ, must not be too large as to avoid the effects of fields of higher order than sextupoles, nor too small as that would lead to a measurement with a poor signal-to-noise ratio. The choice of δ was found by looking at the change of the model OEORM given a known change of sextupole strengths. In Fig. 4.3 this is simulated with and without an artificial BPM noise, $\sigma = 0.40\,\mu\text{m}$, for a number of values of δ. From the figure it is clear that the OEORM depends approximately linearly on the sextupole strength for all investigated values of δ. This linearity can be investigated in more detail by fitting a first order polynomial to each line in Fig. 4.3. The residual of each of these fits can be seen in Fig. 4.4 plotted against δ. The non-linear contribution increases with increasing delta, which can be seen from the increasing residual when fitting to data without noise. However, for the investigated values of δ, this increase is significantly lower than the contribution from BPM noise, which makes it beneficial to chose as large a δ as possible when measuring the OEORM of the MAX IV 3 GeV storage ring. The size of δ is instead limited by whether or not it is practically possible to measure an ORM at a given momentum deviation without significant risk of beam loss. Empirically, this value was found to be $\delta = 3.3\,\%$.

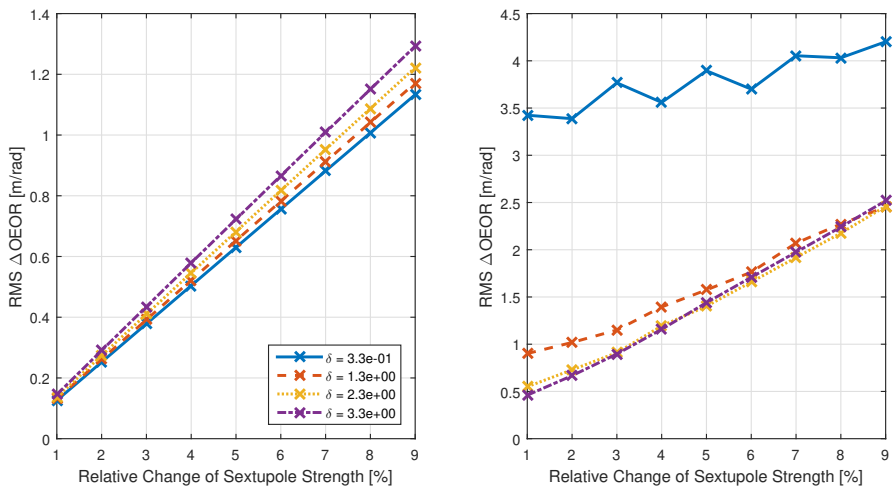

Figure 4.3: Mean difference of the model MAX IV 3 GeV ring OEOR of a single dipole corrector measured with different values of δ when increasing the strength of a single sextupole circuit, in this case belonging to the SD sextupole family. The right-hand side plot includes a normal distributed artificial BPM noise of $\sigma = 0.40\,\mu\text{m}$. A similar behaviour is seen for all other dipole correctors.

A similar investigation was performed by looking at how the linearity of the OEORM with sextupole strengths was affected by the choice of dipole corrector kick strength,

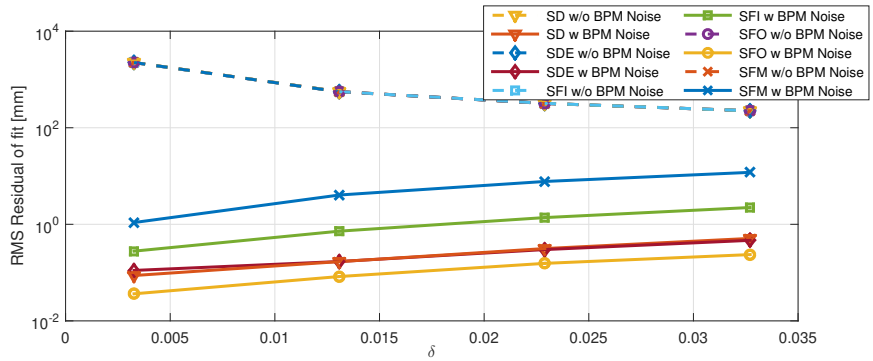

Figure 4.4: Residual when fitting a first order polynomial to the lines in Fig. 4.3, calculated for, and averaged over, all sextupole families and dipole correctors in the MAX IV 3 GeV storage ring.

θ, used when measuring. The results from this investigation can be seen in Fig. 4.5 and 4.6. For the range of investigated values of θ the BPM noise is the dominating non-linear contribution. The non-linear contribution from higher order magnets only becomes greater than the contribution from BPM noise when $\theta \gtrapprox 1\,\mathrm{mrad}$.

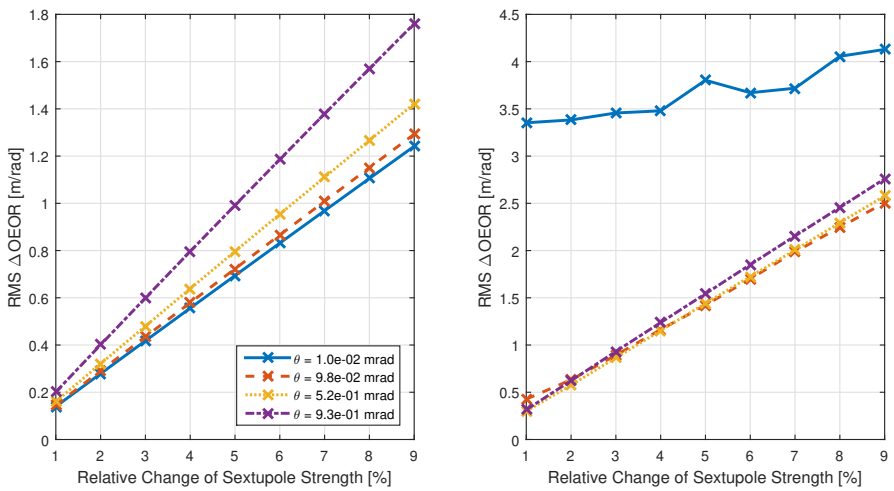

Figure 4.5: Mean difference of the model MAX IV 3 GeV ring OEOR of a single dipole corrector measured with different values θ when increasing the strength of a single sextupole circuit, in this case belonging to the SD sextupole family. The right-hand side plot includes a normal distributed artificial BPM noise of $\sigma = 0.40\,\mu\mathrm{m}$. A similar behaviour is seen for all other dipole correctors.

The maximum possible kick achievable by a dipole corrector in MAX IV 3 GeV storage ring was $\pm 0.5\,\mathrm{mrad}$. However, much of this corrector range was already used to correct the beam orbit, which leaves less range to freely choose a value of θ. A kick $\theta = 0.1\,\mathrm{mrad}$ was empirically found to be sufficient without saturating too many corrector magnets.

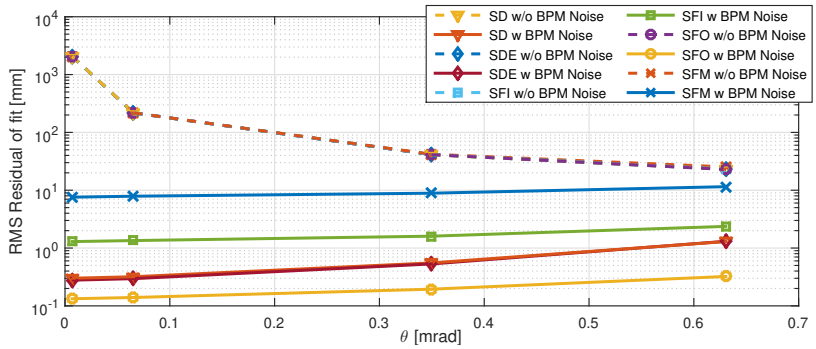

Figure 4.6: Residual when fitting a first order polynomial to the lines in Fig. 4.5, calculated for, and averaged over, all sextupole families and dipole correctors in the MAX IV 3 GeV storage ring.

4.2.2 2nd Order Optics Characterisation

Not only parameters pertaining to the measurement of the OEORM and the 2nd order dispersion need to be determined in order to characterise the 2nd order optics. It is equally important to carefully choose the parameters used when fitting the model to the measured data. The fit was done by minimising the weighted sum of squares

$$\chi^2 = \sum_{ij} E_{ij}^2 = \sum_{ij} \frac{(M_{OEORM,meas,ij} - M_{OEORM,model,ij})^2}{\sigma_i^2} \tag{4.5}$$

which is the OEORM equivalent to Eq. (4.2).

The minimisation of χ^2 is done by iteratively solving

$$-E_{ij} = \frac{\partial E_{ij}}{\partial K_l} \Delta K_l \tag{4.6}$$

for ΔK_l, where K_l are the chosen fitting parameters. For the purpose of saving time, a static Jacobian, $\frac{\partial E_{ij}}{\partial K_l}$, was used. The Jacobian was calculated around the nominal model lattice.

The main parameters used when characterising the 2nd order optics through NOECO were the strengths of the chromatic sextupoles. In the case of the MAX IV 3 GeV storage ring all sextupoles are chromatic. In addition to these, all BPM gains and dipole corrector kick strengths were included in all fits performed in this thesis. This is only natural as any errors in the BPM gain or corrector kicks would translate to a pure amplitude error in a row or column of the OEORM. The 2nd order dispersion is used to distinguish between the contribution from the BPM gains and the corrector kick

strengths to the amplitude of the OEORM, since the dispersion is only dependent on the BPM gains not the dipole correctors. The vertical 2nd order dispersion of the MAX IV 3 GeV storage ring is nominally zero, which means that it cannot be used to separate the vertical BPM gain from vertical corrector kick strength. This singularity is clearly seen in the singular value decomposition of the Jacobian (see Fig. 4.7). During the fitting procedure the corresponding singular value was excluded.

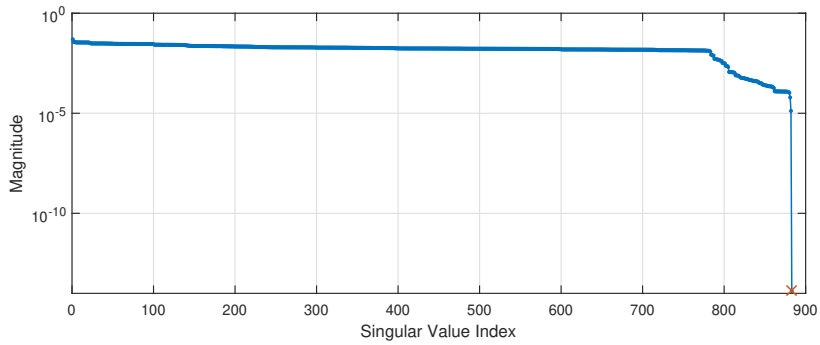

Figure 4.7: Singular values of the OEORM Jacobian. The singular value marked with a red cross corresponds to increasing (decreasing) the vertical BPM gain while decreasing (increasing) the vertical dipole corrector kick strength. This singular value was excluded from the fitting procedure.

Using the strength of all sextupole circuits, the BPM gains, and corrector magnet kick strengths as fitting parameters, NOECO arrives at a model of the 2nd order optics of the MAX IV 3 GeV storage ring. The chromatic functions from such a model can be seen in Fig. 4.8. This model represents the ring before any symmetrisation of the 2nd order optics of the lattice was attempted and all sextupole strengths were set solely by the measured excitation curves.

Since the fitting is done by altering the strength of sextupole circuits the model will not necessarily represent the true sextupole errors of the storage ring. Any errors not isolated to the sextupoles will be attributed to nearby sextupole circuits as accurately as possible, and any errors from individual sextupoles will be attributed to entire circuits. This does not mean that the scheme is completely unhelpful in finding specific sextupole errors, as it will still gives a good idea of the approximate location of the error. Additionally, the simulation results in Paper **I** show that the scheme was able to accurately characterise the chromaticities and chromatic functions of a model lattice with individual sextupole magnet errors, as well as alignment errors.

The scheme was experimentally evaluated by introducing a number of known errors to a set of sextupole circuits. These errors are fully within the parameter space of fitting procedure, and should therefore be relatively easy to detect. The chosen errors consisted of reductions of 2 %, 5 %, 10 %, 15 %, and 20 % introduced to circuits belonging to the families SD, SDend, SFi, SFo, and SFm, respectively. A reduction

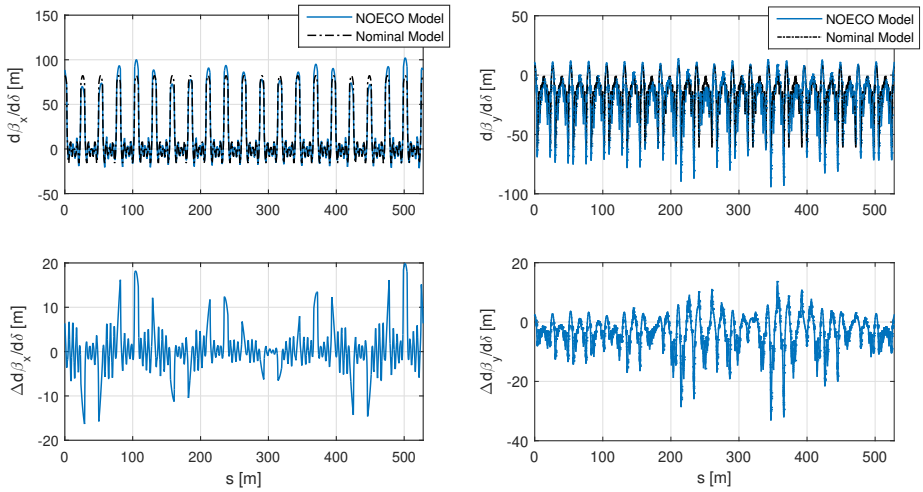

Figure 4.8: Horizontal (left) and vertical (right) chromatic functions and their errors relative to the chromatic functions of the design lattice.

was chosen specifically in order to follow the known hysteresis curve of the magnets. NOECO measurements were performed both before and after introducing the errors, allowing the detection of the change of magnet circuit strengths. In Fig. 4.9 the known reduction, and the one detected by NOECO, can be seen. All of the errors were detected by the scheme, although a spread of errors not corresponding to those introduced can also be seen within each sextupole family.

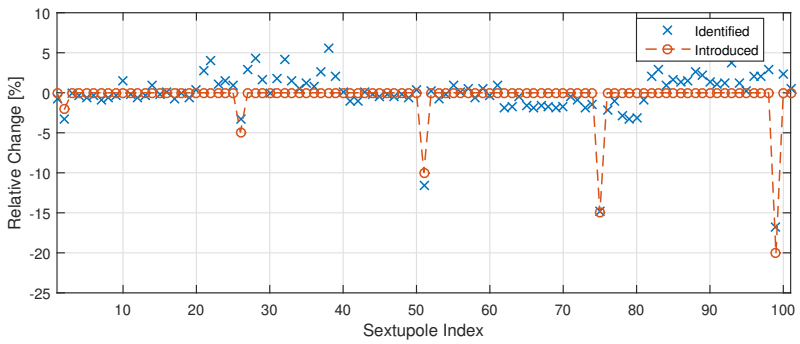

Figure 4.9: Introduced and NOECO-identified relative sextupole circuit errors. The NOECO scheme is able to identify all five errors, but also reports a spread of errors within each family which do not correspond to the introduced errors.

4.2.3 2nd Order Optics Correction

The attribution of unknown sources of sextupole errors to the sextupole circuits is not necessarily an issue when symmetrising the 2nd order lattice. Even if the errors were fully known it might not be practical to correct them all at their source. Instead, NOECO can compensate for such errors using the strength of a nearby sextupole, similarly to how unknown quadrupole errors are compensated with nearby quadrupoles when using the LOCO scheme. Using the sextupole circuit strengths from a NOECO fitted model a new set of sextupole settings can be calculated using

$$m_{machine,new} = \frac{m_{goal}}{m_{fitted}} m_{machine,old} \tag{4.7}$$

where $m_{machine,new}$ and $m_{machine,old}$ are the old and new sextupole settings respectively, m_{goal} are the sextupole settings of the goal lattice, and m_{fitted} are the settings of the NOECO fitted model.

Since there will be discrepancies between the NOECO fitted model and the ring, for instance the source of the sextupole errors, a single correction to the machine will likely not be sufficient to fully symmetrise the 2nd order optics. An iterative process of measuring, fitting, and correcting might be required.

The identified difference in sextupole circuit strengths, compared to nominal, extracted from the initial NOECO iteration can be seen in Fig. 4.10. In this fit each sextupole circuit was an individual fitting parameter. A correction calculated from this fit could not be fully applied to the ring as it resulted in the saturation of several circuits belonging to the SDend family. The large correction to the SDend family can be understood when looking at the lattice structure of the storage ring. The SDend and SFm sextupoles are separated only by a short straight section and a quadrupole magnet (see Fig. B.3 in Appx. B.1). The lack of both BPMs and dipole corrector magnets between the two sextupoles (see Fig. B.2 in Appx. B.1) leaves the NOECO scheme without a measurement point in this area. This makes it difficult for the scheme to separate the effect of the SDend sextupole from that of the SFm, causing it to suggest large changes of these families without significantly affecting the OEORM. This issue was resolved by treating the two families as a single combined sextupole family, which resulted in the second model sextupole settings seen in Fig. 4.10. The use of the combined SDend-SFm circuits also changed the fitted sextupole strengths of other sextupole families but did not significantly alter the 2nd order optics found by the fit, as seen in Fig. 4.11.

The sextupole corrections calculated from the NOECO fit were applied to the MAX IV 3 GeV storage ring followed by a cycling of the magnets to ensure a known hys-

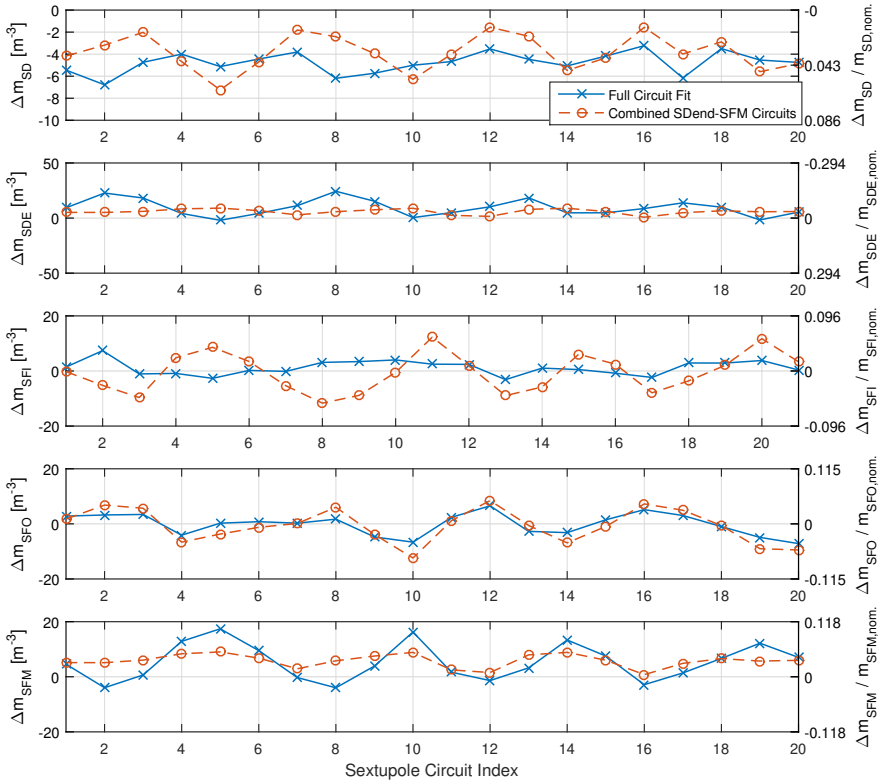

Figure 4.10: Difference between sextupole circuit strengths identified by NOECO and nominal values when fitting all circuits or combining the SDend-SFm families.

teresis curve. This process was iterated yielding the changes to NOECO-fitted model sextupole settings seen in Fig. 4.12. After a single iteration of corrections there is a large reduction in the difference between nominal and NOECO-fitted sextupole strengths. Subsequent iterations only identifies relatively small differences. Notable is the eighth SFi circuit which does not change between iteration one and two. This was because of this particular circuit being saturated.

From the initial and final NOECO-fitted models, corresponding to iterations zero and two, respectively, it is possible to calculate the chromatic functions before and after the NOECO symmetrisation. The remaining chromatic function error when comparing to the nominal model can be seen in Fig. 4.13 along with the same comparison of the 2nd order dispersion function. While the NOECO scheme is able to correct the chromatic functions towards their nominal values it was unable to correct

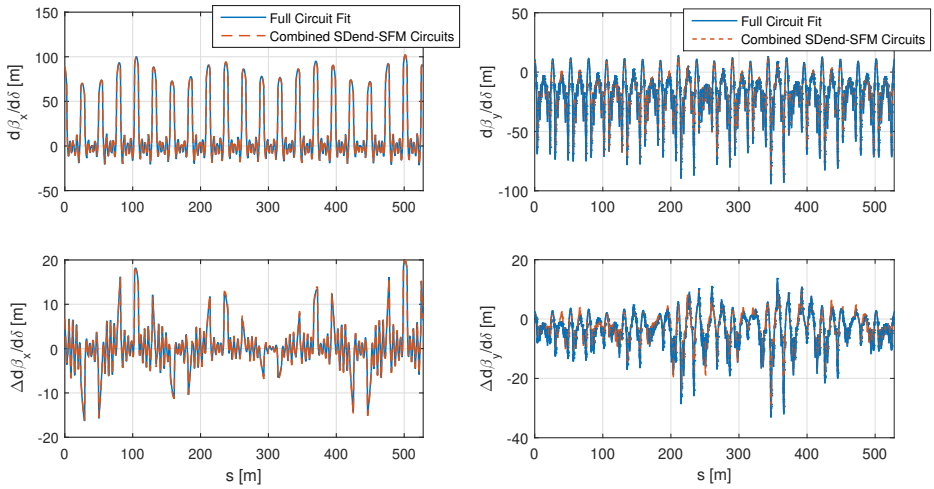

Figure 4.11: Horizontal (left) and vertical (right) chromatic functions and their errors relative to the chromatic functions of the design lattice when fitting all circuits or combining the SDend-SFm families.

the 2nd order dispersion (see Fig. 4.14).

The correction of the 2nd order dispersion could be improved by increasing its weight factor from 1 to 200, where 1 is the weight of every other point in the OEORM. Doing so did not significantly affect the chromatic functions of the fit, as can be seen in Fig. 4.15 and Fig. 4.16. Here, the starting point of the 2nd order optics differs from the final values in Fig. 4.13 due to the two data sets being measured a year apart.

The correction of the chromatic functions towards their nominal values has only been shown through the NOECO optics characterisation, while the correction of the 2nd order dispersion could be seen through direct measurement. The convergence of the chromatic functions is only proof that the fitting procedure is self-consistent, there might still be inconsistencies between the chromatic function of the fitted model and the real ring lattice. As an additional independent measurement of the 2nd order optics the chromaticities of the storage ring were recorded with each iteration of corrections. These can be seen in Tab. 4.1. It is clear that the chromaticites converge towards the nominal values of $+1/+1$, and that the measured and fitted values are in agreement. This is an indication that the fitted optics are describing those of the storage ring well.

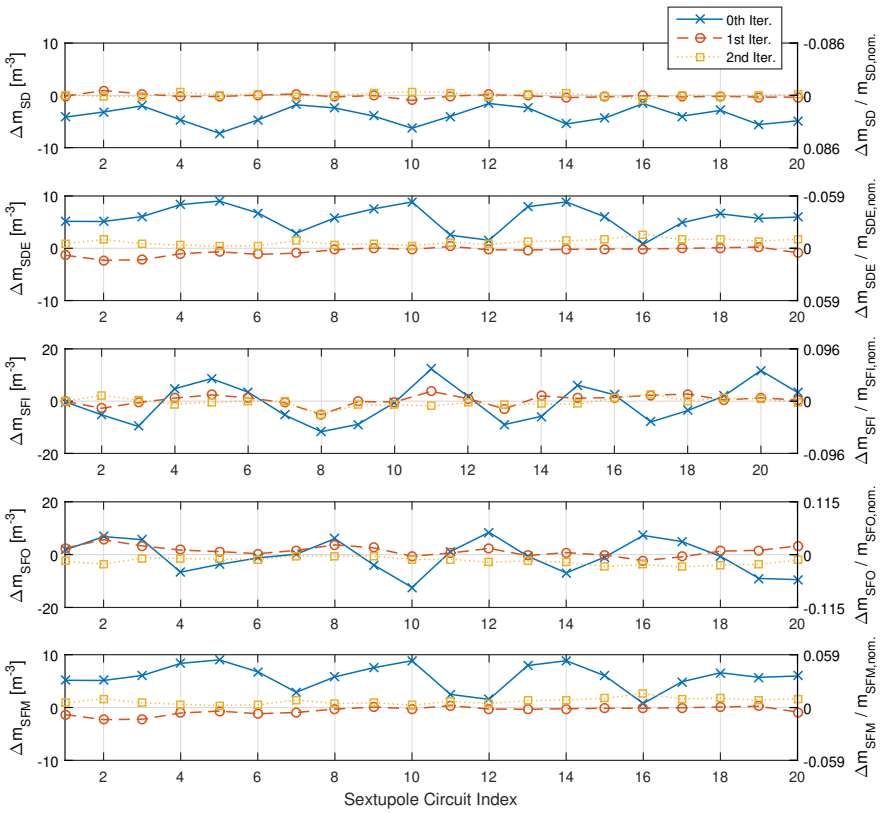

Figure 4.12: Difference between sextupole circuit strengths identified by NOECO with each iteration of corrections and nominal values. As each iteration of corrections is applied the difference in strength identified by NOECO converges towards zero.

Table 4.1: Measured chromaticites and chromaticities of the NOECO fitted model. The NOECO procedure is able to predict the measured chromaticities, and each application of corrections to the sextupole circuit strengths correct the chromaticities towards the nominal values of $+1/+1$.

	Measured ξ_x / ξ_y	Fitted ξ_x / ξ_y
0th Iter.	$+0.9233$ / $+3.2345$	$+0.7873$ / $+3.2507$
1st Iter.	$+1.2167$ / $+0.8254$	$+1.1884$ / $+0.9677$
2nd Iter.	$+1.0089$ / $+0.9722$	$+0.9963$ / $+0.9948$

4.2.3.1 Effect on Performance

The effects of the new sextupole settings on the performance of the MAX IV 3 GeV storage ring were initially investigated through scraper-lifetime measurements, the results of which can be seen in Fig. 4.17. These measurements are done by slowly

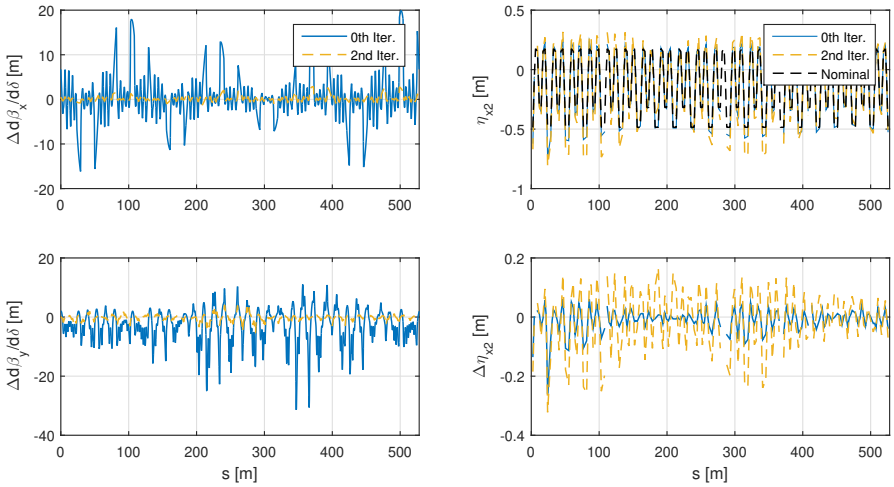

Figure 4.13: Chromatic function errors (left) relative to the chromatic functions of the design model, and measured 2nd order dispersion compared to design (right) after zero and two iterations of corrections. The corrections were calculated from NOECO fits with no additional weighing of the 2nd order dispersion.

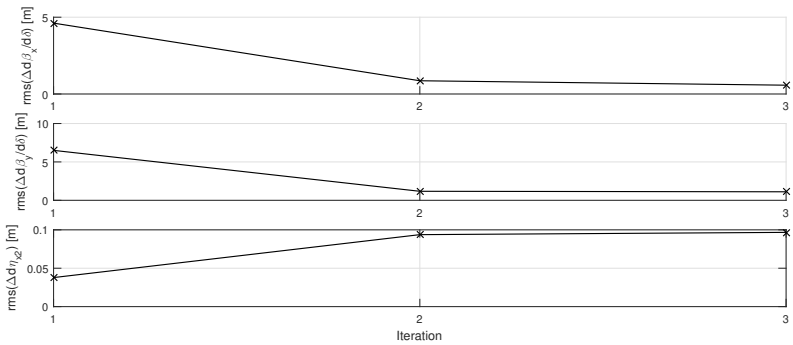

Figure 4.14: Evolution of the RMS errors of the chromatic functions and horizontal 2nd order dispersion with each iteration of corrections applied to the ring. The corrections were calculated from NOECO fits with no additional weighing of the 2nd order dispersion.

inserting a scraper while monitoring the beam lifetime. The distances from the beam centre where the scrapers start affecting the beam lifetime are taken as the transverse dynamic apertures of the lattice at the locations of the scrapers. From these measurements, the horizontal transverse dynamic aperture appears to have increased, without a decrease in the vertical plane.

When performing a scraper-lifetime measurement it is not necessarily the transverse dynamic acceptance which is limiting the beam lifetime. From Eq. (3.80) it is clear that the lattice momentum acceptance is also affected by the scrapers (in this case

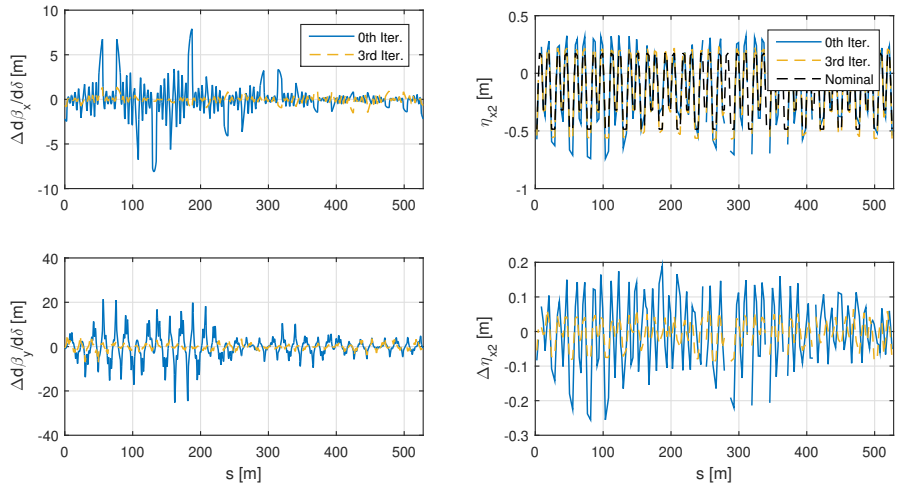

Figure 4.15: Chromatic function errors (left) relative to the chromatic functions of the design model, and measured 2nd order dispersion compared to design (right) after zero and two iterations of corrections. The corrections were calculated from fits with a dispersion weight of 200.

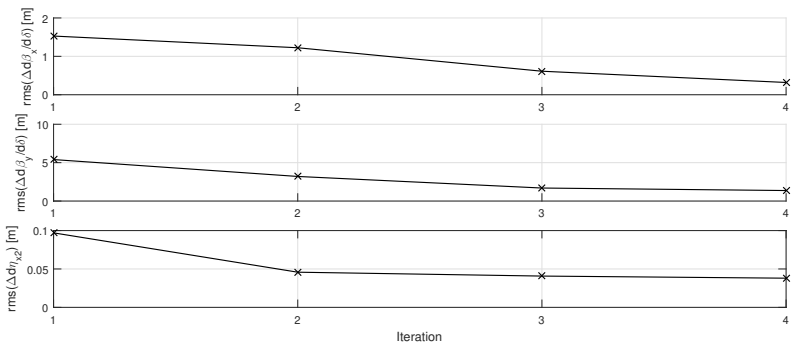

Figure 4.16: Evolution of the RMS errors of the chromatic functions and horizontal 2nd order dispersion with each iteration of corrections applied to the ring. The corrections were calculated from fits with a dispersion weight of 200.

only the horizontal scraper, since the vertical dispersion and betatron coupling are well corrected), which in turn affects the beam lifetime. If the decrease in physical aperture, introduced by the horizontal scraper, limits the momentum acceptance before it limits the dynamic aperture, then the horizontal scraper-lifetime measurement becomes an indirect measurement of the momentum acceptance. In such a case, this measurement cannot be used to derive the horizontal dynamic acceptance.

In order to perform a more direct measurement of the momentum acceptance, the RF voltage was varied while monitoring the beam lifetime. The results of this measurement before and after the NOECO symmetrisation can be seen in Fig. 4.18. These

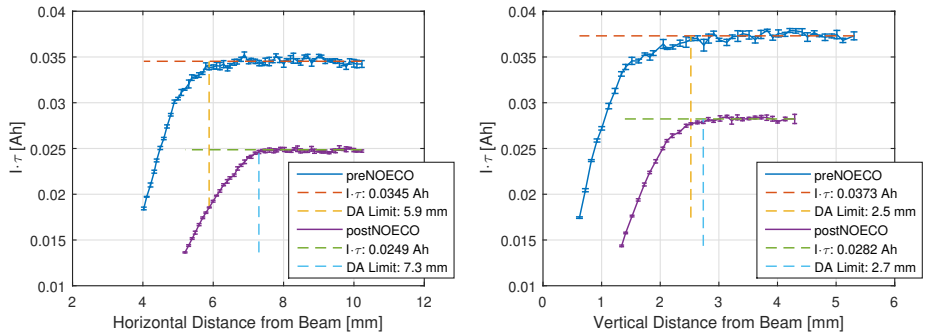

Figure 4.17: Current-lifetime product vs. scraper distance to beam centre. The measurements show a larger horizontal dynamic aperture after the NOECO symmetrisation, compared to the initial settings, without a decrease in the measured vertical dynamic aperture. The difference in initial lifetime for the two settings was due to the higher coupling and concurrent higher vertical emittance in the initial settings.

measurements were done at a bunch current of $\sim 1.5\,\mathrm{mA}$, using a short train of 8 bunches. This allows the gas lifetime contribution to be neglected, while keeping the Touschek lifetime low enough to be accurately measured. Decreasing the RF voltage will only affect the beam lifetime once the RF momentum acceptance is smaller than the lattice momentum acceptance. Since the lifetime of the post-NOECO lattice starts decreasing at a higher RF voltage than the pre-NOECO lattice, it has a larger lattice momentum acceptance.

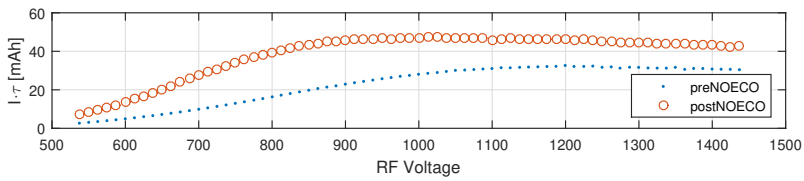

Figure 4.18: Measured beam current-lifetime product of the MAX IV 3 GeV ring vs. total accelerating cavity voltage before and after applying the NOECO corrections to the lattice. The lifetime of the post-NOECO lattice starts decreasing at a higher accelerating voltage indicating a larger lattice momentum acceptance.

The increase in momentum acceptance can be more explicitly seen when comparing the measured lifetime to the theoretical Touschek lifetime's dependence on the RF voltage when only limited by the RF momentum acceptance. This theoretical data was calculated using OPA[47], and scaled to fit the measured current-lifetime product ($I \cdot \tau$) at the lowest voltages where the lifetime is dominated by the RF momentum acceptance (see Fig. 4.19). By taking the measured lifetime as a fraction of the scaled theoretical Touschek lifetime it becomes possible to directly compare the measurements of two lattices with different vertical emittances, as seen in Fig. 4.20. At the operating RF momentum acceptance of the MAX IV 3 GeV storage ring at the time

of the measurement, 5.4 %, the NOECO-symmetrised optics resulted in an increase in Touschek lifetime by a factor of 2 compared to pre-symmetrisation optics.

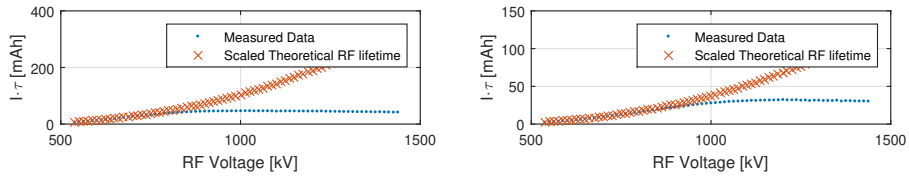

Figure 4.19: Measured current-lifetime product of the pre- (left) and post-NOECO (right) optics at different RF voltages, and the corresponding scaled theoretical Touschek lifetimes, determined only by the RF momentum acceptance.

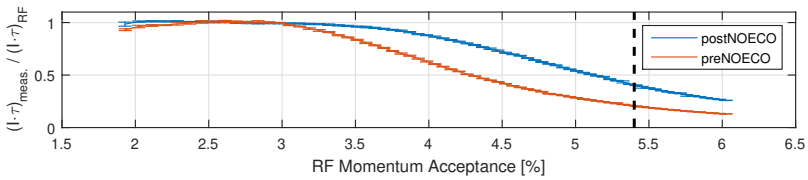

Figure 4.20: Measured current-lifetime product plotted against RF momentum acceptance as a ratio of measured current-lifetime product to simulated Touschek lifetime only determined by the RF momentum acceptance. The vertical dashed line corresponds to the RF momentum acceptance of the MAX IV 3 GeV ring during delivery at the time of the measurements. At this acceptance value the NOECO symmetrization increased the Touschek lifetime by a factor of 2.

The increase in Touschek lifetime is apparent during normal operation. The current and lifetime during a day of standard delivery, before and after applying the sextupole settings found by NOECO, can be seen in Fig. 4.21. Here, the emittance coupling of the new optics has been increased to match that of the previous delivery optics.

An additional effect of the symmetrisation of the 2nd order optics was the ability to inject at nominal betatron tunes (42.20/14.28). Prior to this, delivery was performed at slightly lower tunes ($\sim$ 42.15/14.24), which allowed for injection.

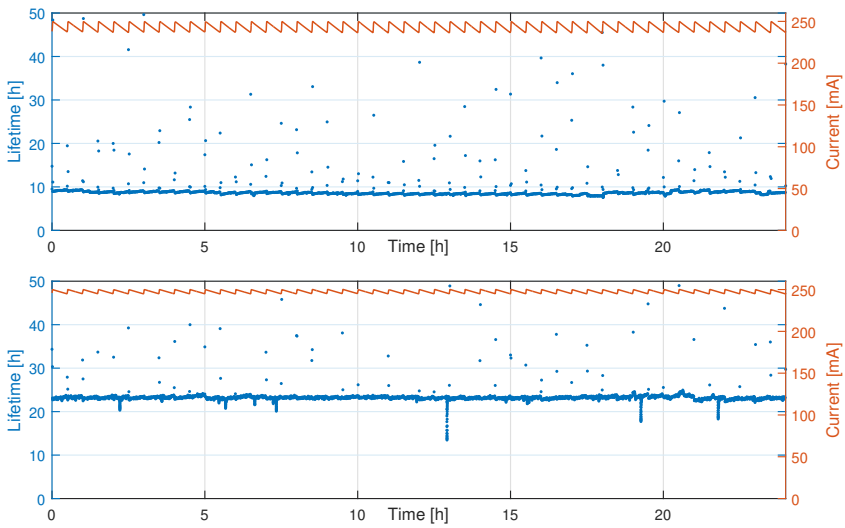

Figure 4.21: Lifetime and stored current of the MAX IV 3 GeV storage ring during normal delivery before (top) and after (bottom) symmetrising the 2nd order optics using NOECO. Data from 2019-06-11 and 2020-01-07, respectively.

Chapter 5

Optics Optimisation

A somewhat different approach to improving the performance of an accelerator is online optimisation. Unlike the previously discussed calibration schemes, optimisation schemes generally do not rely on an established model. Instead, these aim to maximise or minimise an objective function which is either directly measured on the machine, or through a proxy fitness function. While this approach does not provide a characterisation of the optics it does have the advantage of, depending on the choice of fitting objective, being able to improve certain aspects of the machine performance beyond that of the nominal model. However, it might also result in a deterioration of aspects of the performance which were not incorporated in the fitness function.

The following chapter describes the optimisation schemes used on the MAX IV 3 GeV storage ring, as well as their results when applied to different objectives with different parameters. This includes both optimisation done on the ring prior to the development of NOECO, and after NOECO had been deployed (see Sec. 4.2 in Chap. 4).

5.1 Kick Resilience Optimisation

The first changes to the settings of the higher order magnets of the MAX IV 3 GeV ring, not including simple chromaticity correction, were optimisations with the goal of increasing the stored beam's resilience to a kick applied by the horizontal dipole pinger magnet. These optimisations were performed before the development of the NOECO scheme, and are presented in more detail in Paper **VII**. At the time of these experiments the single horizontal dipole pinger was used as an injection kicker. Due to an insufficient kick resilience of the stored beam, the maximum achievable stored current would saturate during injection, as the injection kicker would kick out more

stored beam than was injected. This optimisation aimed to resolve this issue.

The algorithm used for the optimisation was the *Robust Conjugate Direction Search*[48], RCDS, with the relative loss rate of the stored beam when kicked by the dipole injection kicker as the fitness function. The fitting parameters were the settings of the five sextupole magnet families, SD, SDend, SFi, SFm, and SFo, and the three octupole families, OXX, OXY, and OYY. All magnets within each family were changed uniformly by the optimisation procedure in order to reduce its run time. Additionally, a model chromaticity response matrix was used to calculate three linear combinations of sextupoles which did not affect the chromaticity. These were used by the optimisation, rather than using the individual sextupole family strengths directly, resulting in a 6-dimensional parameter space.

Four runs of the optimisation procedure were performed. Between each of these, the dipole kicker kick strength had to be increased in order to ensure a sufficient loss-rate signal for the optimisation algorithm. Despite constructing a chromaticity independent parameter space there were some small drifts in chromaticity, which were corrected between each run. These drifts were believed to be due to mismatches between the model chromaticity response matrix and the machine.

The relative change of sextupole and octupole strengths compared to the initial nominal values can be seen in Fig. 5.1. These changes resulted in an increase in horizontal kick resilience from $1.2\,\mathrm{mrad}$ to $2.1\,\mathrm{mrad}$ while the vertical kick resilience remained constant at $0.51\,\mathrm{mrad}$. This corresponds to an increase in horizontal acceptance from $1.7\,\mathrm{mm\,mrad}$ to $5.2\,\mathrm{mm\,mrad}$.

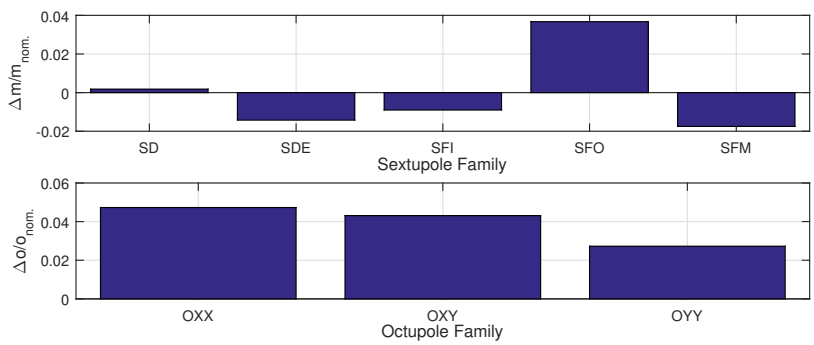

Figure 5.1: Sextupole and octupole family strengths, compared to nominal, arrived at by the kick resilience optimisation.

After the optimisation process an increase of beam current-lifetime product from $2.88\,\mathrm{Ah}$ to $3.75\,\mathrm{Ah}$ was observed. This was due to an increase in lattice momentum acceptance, which was confirmed by a momentum acceptance measurement (see Paper **VII**). The optimisation procedure's ability to increase the momentum acceptance

was due to the loss rate observed when kicking the beam also included a contribution from the Touschek lifetime. The effect of both contributions were reduced, resulting in both an increase in kick resilience and momentum acceptance.

5.2 Lifetime Optimisation

The first octupole optimisations done after the NOECO scheme was deployed on the MAX IV 3 GeV ring were lifetime optimisations which used the beam current-lifetime product as their fitness function. These are presented in more detail in Paper **III**. The algorithm employed for this purpose was RCDS with the octupole family strengths as fitting parameters. Since the octupoles are all connected in series within each family (with some exceptions, see Appx. B.1) this constitutes only three parameters. Although a more granular correction of octupole strengths was technically possible, through the application of shunt resistors to individual magnets, it would not have been practical to implement. The low parameter-space dimensionality was also the reason why optimisation of the octupoles was chosen over characterisation, as too few parameters would likely result in a poor characterisation of the accelerator. The optimisation was performed at a beam current of $3\,\mathrm{mA}$ in an approximate 9-bucket filling pattern in order for the beam lifetime to be sufficiently low to be accurately measured. The optimisation procedure was performed at an accelerating cavity voltage which corresponded to an approximate $5.4\,\%$ RF momentum acceptance. The change in octupole settings found by the procedure can be seen in Tab. 5.1.

Table 5.1: Octupole circuit strengths before and after the current-lifetime optimisation.

	Model Oct.	$I \cdot \tau$ Oct. Opt.	$\Delta o/o$
OXX	$-1649\,\mathrm{m}^{-4}$	$-1802\,\mathrm{m}^{-4}$	$-9.28\,\%$
OXY	$3270\,\mathrm{m}^{-4}$	$3518\,\mathrm{m}^{-4}$	$7.57\,\%$
OYY	$-1420\,\mathrm{m}^{-4}$	$-1236\,\mathrm{m}^{-4}$	$-13.00\,\%$

A momentum acceptance measurement was performed on the ring with model octupole settings and on the lifetime optimised ring, in order to evaluate the effect of the new octupole settings. Model settings refers to octupole settings based solely on rotating coil calibration curves. The measurements were performed at the same filling pattern used during the optimisation, i.e. at a beam current of $3\,\mathrm{mA}$ with an approximate 9-bucket filling pattern. This was done in order to avoid any potential effects of the gas lifetime or IBS. The results of the two measurements can be seen in Fig. 5.2. At the time of writing, the RF momentum acceptance used during beam delivery was approximately $5.4\,\%$. At this level the optimised octupole strengths resulted in an increase in Touschek lifetime of $18.5\,\%$ relative to model octupole settings.

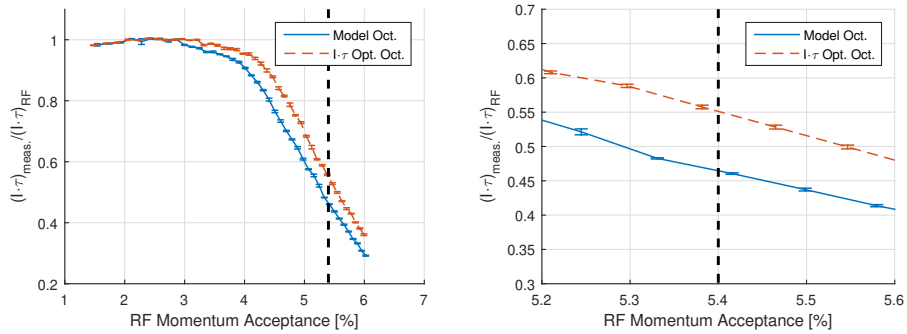

Figure 5.2: Measured lifetime plotted against RF momentum acceptance as a ratio of measured lifetime to Touschek lifetime of a model only limited by the RF momentum acceptance. At the delivery RF momentum acceptance (vertical dashed line) of $5.4\,\%$, the current-lifetime optimisation increased the Touschek lifetime by $18.5\,\%$ relative to model octupole settings, i.e. settings based solely on rotating coil calibration curves.

5.3 ADTS Optimisation

The optics found by the NOECO scheme were also characterised by measuring the ADTS. This measurement was done by kicking the beam with a dipole pinger magnet, either horizontally or vertically, while monitoring the evolution of the beam position using the turn-by-turn BPM data. The field from the pingers was a half sinusoidal with a width of two revolution times. In order to ensure that the entire beam sees approximately the same kick strength, a short bunch train was used. The betatron tune of the kicked beam was extracted from the turn-by-turn data using the NAFF algorithm [49] as it requires relatively few turns of data for an accurate tune measurement. This is important as the decoherence of the kicked beam [50] limits the number of turns of useful data to a few hundred in the case of the MAX IV 3 GeV storage ring. This also means that the beam must be kicked once per data point, rather than monitoring the tune as the transverse beam oscillations dampen.

Figure 5.3 shows the ADTS at the centre of a straight section of the 3 GeV storage ring before and after applying the NOECO correction, but without changing the octupole settings arrived at during the kick resilience optimisation (see Sec. 5.1). The resulting ADTS when applying the model octupole settings to the NOECO symmetrised machine is shown in the same figure. While the ADTS of the NOECO optics is closer to that of the nominal model, compared to the pre-NOECO optics, the improvement is quite small. This is not surprising as the NOECO scheme only corrects the chromatic gradients of the lattice, while not looking at any geometric effects. Each measurement was performed with an iteratively increasing kick strength until a single kick resulted in a $1\,\%$ loss of beam current. Thus, they also provide a conservative measurement of the transverse dynamic aperture.

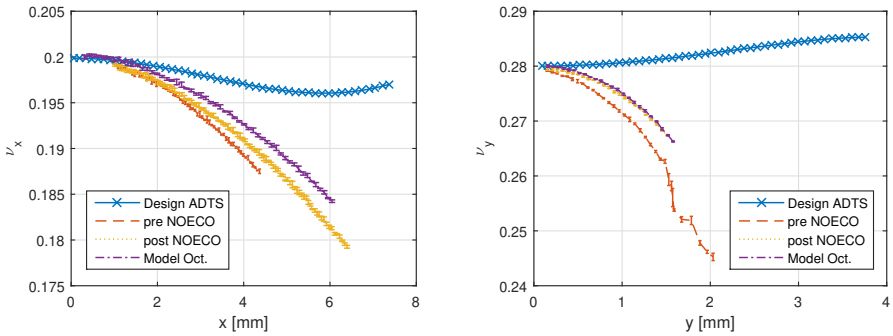

Figure 5.3: Horizontal (left) and vertical (right) ADTS of the MAX IV 3 GeV design model, measured ADTS before and after applying the sextupole corrections suggested by the NOECO scheme, and the ADTS of the NOECO symmetrised machine with model octupole strengths. The amplitude of the beam corresponds to the beta functions at the centre of a long straight section.

In order to arrive at an ADTS which better corresponds to that of the nominal model, an optimisation was set up to minimise the difference between measured and nominal ADTS, the results of which are presented in more detail in Paper **III**. The optimisation was performed on the online machine using the RCDS algorithm. Once again, the octupole family strengths were used as fitting parameters. Since measuring a detailed ADTS (such as the one seen in Fig. 5.3) was judged too time consuming for an iterative optimisation procedure, such as RCDS, a less time consuming proxy was used instead. The proxy consisted of a set of three kick amplitudes: one predominately horizontal, one predominately vertical, and one approximately diagonal. These were applied to the beam using both the horizontal and vertical pinger magnets. From the turn-by-turn data, the betatron tunes and maximum oscillation amplitude of the kicked beam were extracted. In order to be able to extract both transverse tunes, the beam was kicked in both planes for each proxy point. The nominal tune shift, given the oscillation amplitude, was found using a ADTS map calculated from the model. The function to minimise was the sum-square difference between the measured and nominal tune shifts at the three proxy points.

The ADTS of the ring when using the model octupole strengths can be seen in Fig. 5.4. Here, the tune shift in each plane was measured with an additional small excitation in the opposite plane in order to be able to measure both betatron tunes. The most noticeable difference between this measured and the nominal ADTS was the vertical tune shift with vertical amplitude, which was in the opposite direction.

After a single run of the optimisation procedure the resulting ADTS was the one seen in Fig. 5.5. All four tune shifts are significantly closer to their nominal model values. The change of octupole strengths which the optimisation procedure arrived at can be seen in Tab. 5.2.

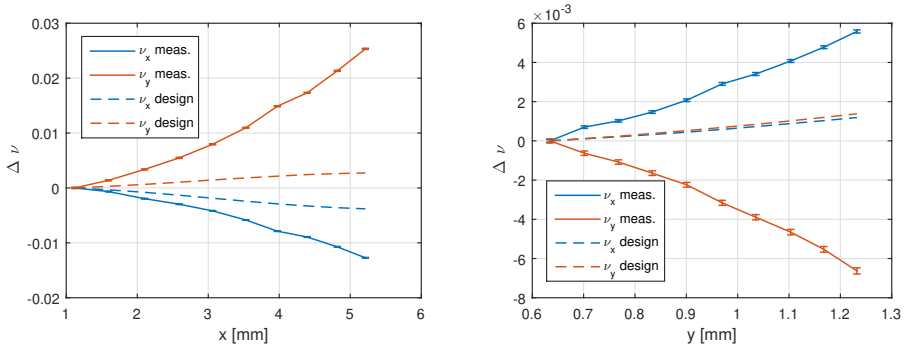

Figure 5.4: Measured tune shift with horizontal (left) and vertical (right) amplitude of the MAX IV 3 GeV ring with model octupole strengths, and the corresponding design tune shifts. The tune shift with horizontal amplitude is larger than design, while the vertical tune shift with vertical amplitude has the opposite sign. The measurement in each plane was done with a slight excitation in the opposite plane in order to measure both tunes.

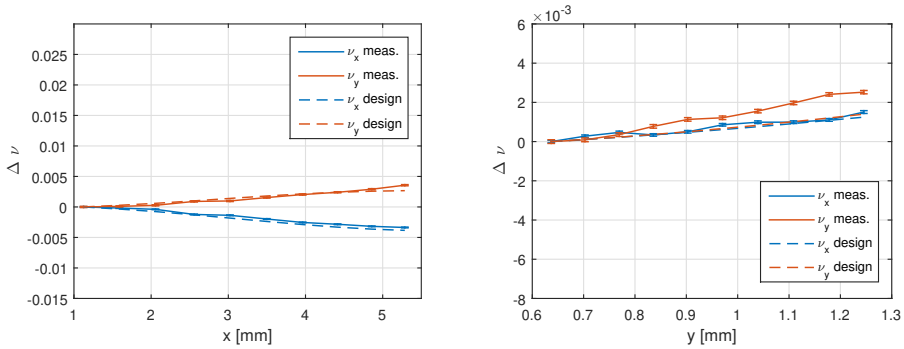

Figure 5.5: Measured tune shift with horizontal (left) and vertical (right) amplitude after the ADTS octupole optimisation, and the corresponding design tune shifts. The difference between the measured and design ADTS has decreased in both planes relative to the initial octupole settings (see Fig. 5.4). The measurement in each plane was done with a slight excitation in the opposite plane in order to measure both tunes.

Table 5.2: Octupole circuit strengths before and after the ADTS optimisation.

	Model Oct.	ADTS Oct. Opt.	$\Delta o/o$
OXX	$-1649\,\mathrm{m}^{-4}$	$-1607\,\mathrm{m}^{-4}$	$-2.53\,\%$
OXY	$3270\,\mathrm{m}^{-4}$	$3449\,\mathrm{m}^{-4}$	$5.48\,\%$
OYY	$-1420\,\mathrm{m}^{-4}$	$-1112\,\mathrm{m}^{-4}$	$-21.13\,\%$

In Fig. 5.6 the ADTS of the current-lifetime optimised lattice and the ADTS-optimised lattice can both be seen, along with those of the lattice with model octupole strengths. Unsurprisingly, the ADTS of the lattice with ADTS-optimised octupoles follows the model ADTS the closest. As described in Sec. 5.2, this measurement also gives a value of the horizontal and vertical dynamic acceptance, which are summarised in Tab. 5.3. From the table we see that the ADTS-optimised octupole settings also result in an

increase in both horizontal and vertical dynamic acceptance compared the model octupole settings. The current-lifetime optimisation outperformed the ADTS optimisation in terms of vertical acceptance, but resulted in a lower horizontal acceptance than the model octupole settings.

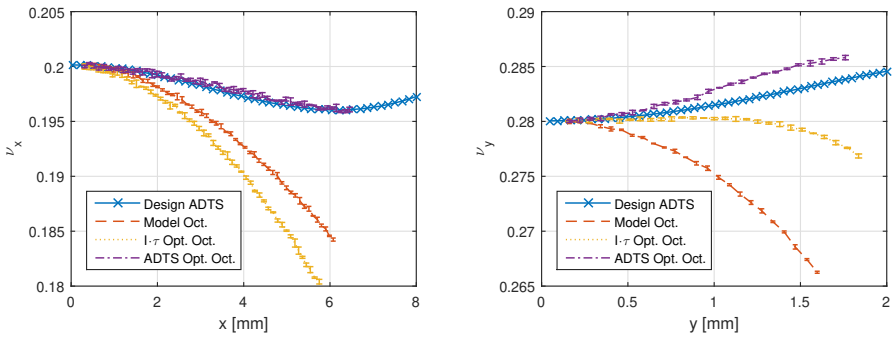

Figure 5.6: Horizontal (left) and vertical (right) ADTS of the MAX IV 3 GeV design model, and measured ADTS of the 3 GeV ring with three different sets of octupole settings. The amplitude of the beam corresponds to the beta functions at the centre of a long straight section.

Table 5.3: Transverse dynamic acceptance as measured by the BPM turn-by-turn data when kicking the beam with a dipole pinger magnet. Here, the limit of the dynamic acceptance is given by the kick strength which causes a $1\,\%$ loss of stored current. These limits correspond to the measurement seen in Fig. 5.6.

	A_x[mm mrad]	A_y[mm mrad]
Model Octupoles	4.10	1.28
$I \cdot \tau$ Optimisation	3.67	1.69
ADTS Optimisation	4.63	1.55

In Fig. 5.7 the results of momentum acceptance measurements on the three octupole settings can be seen. At the delivery RF momentum acceptance of $5.4\,\%$, the ADTS optimisation increased the Touschek lifetime by $15.1\,\%$ relative to nominal octupole settings, compared to a $18.5\,\%$ increase in the case of the current-lifetime optimisation. The increase in momentum acceptance is believed to be mainly due to chromatic effects from the OYY family of octupoles, despite this family being only weakly chromatic. Such an increase is natural in the case of the current-lifetime optimisation as the procedure is indirectly looking at the momentum acceptance through the Touschek lifetime. The increase in momentum acceptance from the ADTS optimisation, which is neither directly nor indirectly looking at the momentum acceptance, is believed to be due to the resulting optics approaching the design optics. These optics have a favourable performance in terms of both momentum and transverse acceptance.

The injection scheme of the MAX IV 3 GeV storage ring utilises, at the time of writing, a multipole injection kicker[51]. However, should this device fail, a single horizontal

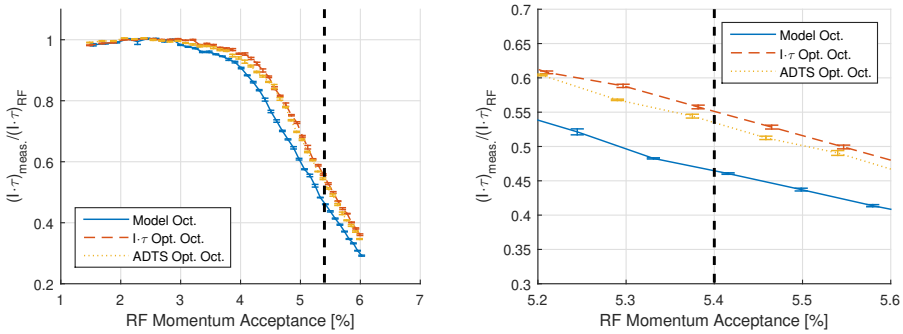

Figure 5.7: Measured lifetime plotted against RF momentum acceptance as a ratio of measured lifetime to Touschek lifetime of a model only limited by RF momentum acceptance. At the delivery RF momentum acceptance (vertical dashed line) of $5.4\,\%$, the current-lifetime optimisation increased the Touschek lifetime by $18.5\,\%$, while the ADTS optimisation resulted in an increase of $15.1\,\%$, relative to model octupole strengths.

dipole kicker magnet will serve as a backup system. It is therefore of some importance to have optics with a large horizontal dynamic acceptance, as to ensure efficient injection with the dipole kicker. Of the two octupole optimisation procedures presented here, only the ADTS optimisation resulted in an increase in the horizontal dynamic acceptance. It is thus the more likely candidate when determining the octupole strengths of the ring, despite not resulting in the largest Touschek lifetime.

Chapter 6

Transverse Resonance Island Buckets

This chapter presents the investigations into using TRIBs as a mode of pseudo single-bunch delivery. These investigations have almost exclusively focussed on the MAX IV 1.5 GeV storage ring, due to the greater interest in single-bunch delivery from its user beamlines. Thus, the work presented in this chapter, and most of Paper **IV**, pertains to the 1.5 GeV ring.

6.1 TRIBs at the MAX IV 1.5 GeV Storage Ring

A beamline at a storage ring might be interested in light with different temporal structures. These temporal structures can be altered by changing in which buckets to store electrons, and which to leave empty. A temporal structure which is of interest to many beamline users, other than the semi-continuous light provided by an even fill, is a single short pulse. Such a pulse can be provided by employing a single-bunch filling pattern, or by leaving a sufficient number of buckets empty before and after a single bunch to allow the beamline to block the light from all but this bunch. In the case of the MAX IV 1.5 GeV storage ring, the former of the two filling patterns is regularly used to provide single-bunch light to beamlines.

The single bunch filling pattern employed in the 1.5 GeV ring is detrimental to continuous-light users who are generally interested in higher photon flux. Therefore, the beamlines have to agree amongst themselves whether or not to sacrifice beam time of continuous-light users for the benefit of single-bunch users. In order to avoid this

compromise there has been a number of investigations into pseudo single-bunch modes of delivery, both globally[52] and at the MAX IV Laboratory[53,54,55,56], which would allow for simultaneous single-bunch and continuous delivery. The 1.5 GeV ring utilises passive harmonic cavities which are designed to perform optimally with a homogeneous multi-bunch filling pattern. Since these are required to achieve the desired bunch lengthening, beam lifetime, emittance, and high current stability[16] it is generally preferable that a pseudo single-bunch mode of delivery employed at this storage ring does not significantly alter the longitudinal filling pattern. Investigations into one such mode of delivery will be presented in this thesis, pseudo single-bunch trough Transverse Resonance Island Buckets, TRIBs, which is the subject of Paper **IV**. Using this scheme for single-bunch delivery was pioneered at the MLS and BESSY II[27]. For a brief comparison between this scheme and other single-bunch schemes investigated at the MAX IV Laboratory, see Paper **IV**.

The TRIBs pseudo single-bunch mode of delivery in the MAX IV 1.5 GeV ring operates the ring at a working point close to the horizontal third order resonance. By adjusting the strength of the sextupoles, the ADTS can be made to cross the resonance and establish islands in phase space. In order to achieve stable islands with a clear separation from the core, the tune spread of the beam was reduced by setting the horizontal chromaticity to zero. The islands make up the island orbit (see Fig. 6.1), which can be populated independently of the core orbit. The separation of the islands from each other, and from the core, in horizontal phase space allows each beamline to individually choose whether to use the SR of the core orbit or one of the islands, while blocking the other sources of SR. A conceptual image of this setup can be seen in Fig. 6.1, where both the core and island orbit are populated. In this figure, an aperture is used to select only the SR of a single island. If the island orbit has a single-bunch fill, while the core has an even multi-bunch fill, this allows for simultaneous single- and multi-bunch delivery. Additionally, a beamline would be able to easily switch between the two modes of delivery without affecting other beamlines at the storage ring.

The island orbit of the 1.5 GeV storage ring is populated by exciting a bunch in the core beam using a resonant excitation at the core tune, which is generated using the bunch-by-bunch system and applied with a stripline kicker[57]. Sufficient excitation amplitude causes the population of the bunch to leave the core and become trapped in the islands. This process results in the core bunch being split three-ways between the three islands in horizontal phase space. The population will remain in the island after the excitation is turned off, and diffuses only slowly back to the core over tens of minutes. A beamline observing only a single island source will see SR with a repetition rate of a single-bunch fill and an intensity of roughly one third of that of the core bunch which was used when populating the island. Using the same bunch-by-bunch

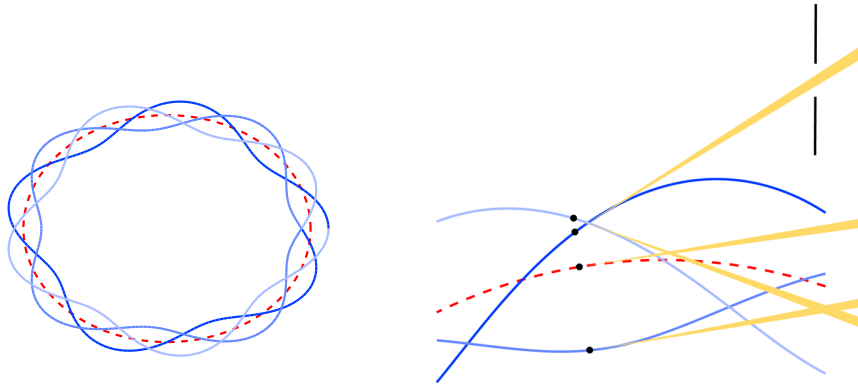

Figure 6.1: Left: Conceptual top-down view of a storage ring with a core (dashed red) and island (solid blue) orbit. The amplitude of the island orbit has been exaggerated. Right: Conceptual view of a beamline accepting the SR from a single island, while blocking the remaining two islands as well as the core.

system the population of the islands can be moved back to the core, without any loss of beam.

From linear optics characterisation using LOCO[44], the island orbit in horizontal phase space was found (see Fig. 6.2). Due to the core bunch being split three ways when populating the islands, it is not possible to confirm the island orbit calculated from the optics characterisation using the BPMs. However, the orbit can be confirmed by looking at the location of the islands as seen by the diagnostic beamlines of the ring. This comparison can be seen in Fig. 6.3. The simulated island orbit agrees well with the island positions in both diagnostic beamlines. This is a good indication of the accuracy of the simulated island orbit in the rest of the ring.

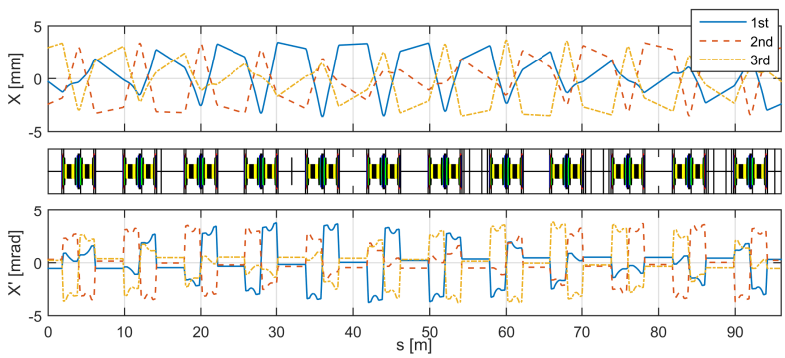

Figure 6.2: Simulated horizontal island orbit for each of the three turns of the orbit. The orbit was found using a LOCO fitted model of the machine while operating in the TRIBs mode.

The simulated island orbit seen in Fig. 6.2 shows that the islands are offset from the

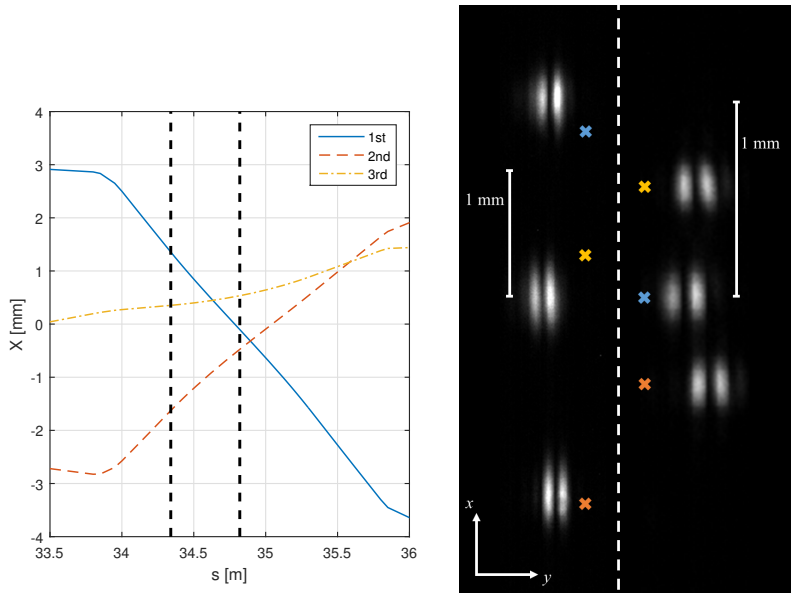

Figure 6.3: Left: Island orbit from Fig. 6.2 at the location of the source spots of the two diagnostic beamlines (indicated by the dashed vertical lines). Right: Islands as seen by the diagnostic beamlines when only the island orbit is populated. The coloured crosses correspond to the predicted horizontal island positions in the figure to the left.

nominal orbit by up to $\sim 3.5\,\mathrm{mm}$ and $\sim 0.5\,\mathrm{mrad}$ in the straight sections. Such large displacements raise the concern that the sources provided by the island orbit might be outside the acceptance of the beamlines. In order to verify that this was not the case, experiments were performed together with the FinEst and FlexPES beamlines. At the time of writing, these beamlines are the ones most interested in single-bunch delivery. The experiments showed that both beamlines were able to isolate the SR from a single island while blocking all other sources. Further tests with FlexPES allowed the beamline to thread the SR all the way to the sample. This is a necessary step to be able to use the TRIBs mode of operation for pseudo single-bunch delivery.

6.2 Effect of ID Focussing

Since the position of the islands in phase space is dependent on the horizontal tune and ADTS any change of horizontal focussing, e.g. from an ID changing its gap or phase, will move the islands. This might lead to a reduction of flux at a beamline taking SR from the island orbit, as their alignment to the source spot may no longer be correct. In order to resolve this issue there needs to be scheme in place which corrects for the perturbations in focus from the IDs. The experiments with FinEst and FlexPES indicated that it was not sufficient to correct the perturbation globally

by restoring the betatron tunes. Instead a scheme which also corrects the perturbations to the beta functions is required. This is because of the dependence of the ADTS (see Eq. (3.56)) on the beta functions. At the time of writing, such a correction scheme is in development at the 1.5 GeV ring. Once the perturbations from the IDs are sufficiently compensated for, the TRIBs mode of operation has the potential of enabling pseudo single-bunch delivery in the MAX IV 1.5 GeV storage ring.

Chapter 7

Conclusions and Outlook

7.1 Characterisation and Calibration of 2nd Order Optics

In this thesis, properties of higher order optical functions have been studied with the purpose of characterising and calibrating the non-linear optics of a storage ring. As the field of non-linear optics is quite expansive, this part of the thesis focusses on the lowest non-linear order of optics, the 2nd order optics.

For this purpose the object of study has been the MAX IV 3 GeV storage ring, the first realised fourth generation synchrotron light source. This new generation of storage rings has higher requirement on the 2nd order components of the lattice. In this thesis the novel NOECO scheme was presented. It is an expansion of the well-known LOCO scheme and uses the quadrupole feed-down from chromatic sextupoles to correct the 2nd order optics. The NOECO scheme's application to the MAX IV 3 GeV storage ring resulted in new chromatic sextupole settings which were presented in this thesis. These new settings achieved a symmtrisation of the chromatic functions and a concurrent correction of the lattice chromaticity. Measurements of the momentum acceptance before and after applying these settings showed an increase of Touschek lifetime by a factor 2 at the delivery RF momentum acceptance, relative to model sextupole settings. This increase could also be seen during delivery as an increase in beam lifetime from 2.5 Ah to 5.0 Ah.

With the commissioning of several new low emittance fourth generation storage rings, a more detailed control of the strong non-linear magnetic elements is required. Although limited to chromatic sextupoles, the NOECO scheme is one method which can be used to calibrate such a lattice and help achieve the desired performance. The NOECO scheme has also been shown to be able to accurately characterise the 2nd

order optics, which makes it a tool for investigating and identifying unknown errors in the lattice.

7.2 Optics Optimisation

A different approach to non-linear optics correction is the online optimisation of machine performance. This type of optimisation can be performed with a variety of objectives and fitting parameters. Since the number of non-linear magnets in the MAX IV 1.5 GeV ring is quite small, the optimisation experiments were performed on the 3 GeV storage ring, which offered a larger parameter space. These experiments had the goal of increasing beam kick resilience, beam lifetime, as well as correcting the ADTS towards that of the design lattice. The parameter space of the optimisations consisted of either the sextupole and octupole strengths, or only the octupole strengths.

In the case of the kick resilience of the stored beam of the MAX IV 3 GeV storage ring the optimisation was able to achieve an increase of $\sim 75\,\%$, using both sextupole and octupole family strengths as fitting parameters. This increase was important, as it allowed for an increase in stored current when injecting with the dipole injection kicker used at the time. The optimisation also resulted in an unintentional increase of beam momentum acceptance, which came about due to the beam lifetime contributing to the value of the fitness function.

With the introduction of the NOECO scheme the strengths of the 3 GeV ring sextupoles were already set through calibration. This limited the parameter space of subsequent lattice optimisations to the three octupole families. Presented in this thesis were optimisation procedures with the goal of increasing the current-lifetime product, or shape the ADTS. Both of these procedures resulted in a significant increase in Touschek lifetime, with the current-lifetime optimisation showing the largest increase. This procedure also had the largest increase in vertical acceptance, but a decrease in horizontal. The ADTS optimisation increased both transverse acceptances relative to model octupole settings, but had a smaller increase in both Touschek lifetime and vertical acceptance, compared to the current-lifetime optimisation. The increase of the different aspects of the machine performance have to be weighed against each other in order to determine which method is preferred.

As shown in this thesis, online optimisation of a storage ring is an effective method for increasing specific aspects of machine performance. It is relatively easy to deploy, and requires no model of the storage ring lattice. However, such procedures can sometimes have detrimental effects on parts of the performance which were not part of the fitness function. These effects can be difficult to predict, as a model-free optimisation

procedure offers no characterisation of the lattice. Employing a multi-objective optimisation might alleviate some of these problems at the cost of a more time-consuming optimisation procedure.

7.3 TRIBs as a Mode of Delivery

This thesis presents the results of all experiments performed on the MAX IV 1.5 GeV storage ring pertaining to optics which supports TRIBs. These have the potential of enabling pseudo single-bunch as a mode of delivery. The conducted studies show that it is possible to create and individually populate island buckets separated in transverse phase space from the standard closed orbit beam position. Further experiments performed in collaboration with the FinEst and FlexPES beamlines proved that the island separation was sufficient to allow the beamlines to make use of the synchrotron radiation from one island, while blocking all other sources.

The TRIBs mode of operation is more sensitive to focussing perturbations, compared to the standard mode of delivery, since these translate to a change of island position in phase space. In order to be able to reliably use this as a mode of pseudo single-bunch delivery an ID compensation scheme which sufficiently cancels perturbations is required. Such a scheme is currently being developed for the MAX IV 1.5 GeV storage ring. Once it has been implemented, TRIBs is a promising candidate for achieving pseudo single-bunch delivery in the MAX IV 1.5 GeV storage ring.

References

[1] D. Iwanenko and I. Pomeranchuk. On the Maximal Energy Attainable in a Betatron. *Phys. Rev.*, 65:343–343, June 1944.

[2] H. C. Pollock. The discovery of synchrotron radiation. *American Journal of Physics*, 51(3):278–280, 1983.

[3] History of Synchrotron Radiation. `https://xdb.lbl.gov/Section2/Sec_2-2.html`. Accessed: 2022-01-20.

[4] R. Chasman, G. K. Green, and E. M. Rowe. Preliminary Design of a Dedicated Synchrotron Radiation Facility. *IEEE Transactions on Nuclear Science*, 22 (3):1765–1767, 1975.

[5] N. Martensson and M. Eriksson. The saga of MAX IV, the first multi-bend achromat synchrotron light source. *Nucl. Instrum. Methods Phys. Res. A*, 907: 97–104, 2018.

[6] D. Einfeld, J. Schaper, and M. Plesko. Design of a diffraction limited light source (DIFL). In *Proc. of the 1995 Particle Accelerator Conference*, volume 1, pages 177 – 179, 06 1995.

[7] M. Eriksson, J. Ahlbäck, Å. Andersson, M. Johansson, S. C. Leemann D. Kumbaro, C. Lenngren, P. Lilja, F. Lindau, L.-J. Lindgren, L. Malmgren, J. Modeér, R. Nilsson, M. Sjöström, J. Tagger, P. F. Tavares, S. Thorin, E. Wallén, S. Werin, B. Anderberg, and L. Dallin. The MAX IV synchrotron light source. In *Proc. of the 2nd International Particle Accelerator Conference*, pages 3026–3028, San Sebastián, Spain, 2011.

[8] J. D. Jackson. *Classical Electrodynamics*. Wiley, 3 edition, 1999.

[9] K. Wille. *The Physics of Particle Accelerators - An Introduction*. Oxford, 2000.

[10] A. Liénard. Champ électrique et magnétique produit par une charge concentrée en un point et animée d'un mouvement quelconque. *L'éclairage Electrique*, 16, 1898.

[11] E. Wiechert. Elektrodynamische Elementargesetze. *Annalen der Physik*, 309: 667–689, 03 2006.

[12] F. Frenet. Sur les courbes à double courbure. *Journal de mathématiques pures et appliquées*, 17:437–447, 1852.

[13] H. Wiedemann. *Particle Accelerator Physics*, chapter 1, pages 3–30. Springer, 3 edition, 2007.

[14] K. L. Brown and R. V. Servranckx. First- and second-order charged particle optics. Technical Report SLAC-PUB-3381, SLAC, July 1984.

[15] H. Wiedemann. *Particle Accelerator Physics*, chapter 3, pages 63–109. Springer, 3 edition, 2007.

[16] Detailed Design Report. Technical report, MAX IV Laboratory, 2010.

[17] H. Wiedemann. *Particle Accelerator Physics*, chapter 2, pages 37–59. Springer, 3 edition, 2007.

[18] G. W. Hill. On the part of the motion of the lunar perigee which is a function of the mean motions of the sun and moon. *Acta Mathematica*, 8, 1886.

[19] H. Wiedemann. *Particle Accelerator Physics*, chapter 5, pages 153–187. Springer, 3 edition, 2007.

[20] M. J. Liouville. Leçons sur les fonctions doublement périodiques faites en 1847 par M. J. Liouville. *Journal für die reine und angewandte Mathematik (Crelles Journal)*, 1880(88-89):277–310, 1880.

[21] G. Floquet. Sur les équations différentielles linéaires à coefficients périodiques. *Annales scientifiques de l'École Normale Supérieure*, 12:47–88, 1883.

[22] S. Y. Lee. *Accelerator Physics*, chapter 2, pages 35–237. World Scientific Publishing Co. Pte. Ltd., 3 edition, 2011.

[23] H. Wiedemann. *Particle Accelerator Physics*, chapter 13, pages 479–501. Springer, 3 edition, 2007.

[24] C. Pellegrini. On a new instability in electron-positron storage rings. (the head-tail effect). *Nuovo Cim. A*, 64:447–473, 1969.

[25] H. Wiedemann. *Particle Accelerator Physics*, chapter 14, pages 503–534. Springer, 3 edition, 2007.

[26] A. Streun. Lattices for light sources. In *Proc. of CAS - CERN Accelerator School: Intermediate Course on Accelerator Physics*, pages 217–244, 2003.

[27] M. Ries, J. Feikes, T. Goetsch, P. Goslawski, J. Li, M. Ruprecht, A. Schälicke, and G. Wüstefeld. Transverse Resonance Island Buckets at the MLS end BESSY II. In *Proc. 6th International Particle Accelerator Conference*, pages 138–140, Richmond, VA, USA, 2015.

[28] K. R. Symon. Beam extraction at a third integral resonance I-IV. Technical Report FN-130, 134, 140, 144, Fermilab, 1968.

[29] S. Y. Lee. *Accelerator Physics*, chapter 3, pages 239–416. World Scientific Publishing Co. Pte. Ltd., 3 edition, 2011.

[30] J. B. Murphy. Synchrotron Light Source Data Book. Technical Report BNL-42333, BNL, 1996.

[31] H. Wiedemann. *Particle Accelerator Physics*, chapter 6, pages 191–231. Springer, 3 edition, 2007.

[32] H. Wiedemann. *Particle Accelerator Physics*, chapter 8, pages 289–329. Springer, 3 edition, 2007.

[33] F. J. Cullinan, Å. Andersson, and P. F. Tavares. Harmonic-cavity stabilization of longitudinal coupled-bunch instabilities with a nonuniform fill. *Phys. Rev. Accel. Beams*, 23:074402, July 2020.

[34] Å. Andersson and A. Streun. Lifetime and acceptance of the SLS storage ring. In *Proc. of the 10th European Particle Accelerator Conference*, pages 3421–3423, Edinburgh, Scotland, 2006.

[35] J. LeDuff. Single and Multiple Touschek Effects. Technical Report CERN 89-01, CERN, Geneva, 1989.

[36] A. Streun. Momentum acceptance and Touschek lifetime. Technical Report SLS Note 18, PSI, November 1997.

[37] A. Nadji, G. Flynn, J.-L. Laclare, M.-P. Level, P. Nghiem, and J. Payet. Energy acceptance and Touschek lifetime calculations for the SOLEIL project. In *Proc. of the 1997 Particle Accelerator Conference*, volume 2, pages 1517–1519, 1997.

[38] M. Eriksson, L.-J. Lindgren, M. Sjöström, E. Wallén, L. Rivkin, and A. Streun. Some small-emittance light-source lattices with multi-bend achromats. *Nucl. Instrum. Methods Phys. Res. A*, 587(2):221–226, 2008.

[39] P. Röjsel. A beam position measurement system using quadrupole magnets magnetic centra as the position reference. *Nucl. Instrum. Methods Phys. Res. A*, 343 (2):374–382, 1994. ISSN 0168-9002.

[40] A. Stella. Analysis of the DAFNE Beam Position Monitor with a Boundary Element Method. DAFNE Technical Note CD-10, INFN-LNF, Accelerator Division, 1997.

[41] J. Breunlin and Å. Andersson. Emittance Diagnostics at the MAX IV 3 GeV Storage Ring. In *Proc. of the 7th International Particle Accelerator Conference*, pages 2908–2910, 2016.

[42] Å. Andersson. Emittance Measurements on Future Ring Light Sources. presented at FLS2018 in Shanghai, China, unpublished, June 2018.

[43] Å. Andersson, M. Böge, A. Lüdeke, V. Schlott, and A. Streun. Determination of a small vertical electron beam profile and emittance at the Swiss Light Source. *Nucl. Instrum. Methods Phys. Res. A*, 591:427–446, 2008.

[44] J. Safranek. Experimental determination of storage ring optics using orbit response measurements. *Nucl. Instrum. Methods Phys. Res. A*, 388:27–36, 1997.

[45] A. Terebilo. Accelerator modeling with MATLAB accelerator toolbox. In *Proc. of the 2001 Particle Accelerator Conference*, volume 4, pages 3203–3205, 2001.

[46] S. C. Leemann. Updates to the MAX IV 3 GeV Storage Ring Lattice. Technical Report 20121107, MAX-lab, November 2012, Rev. 2014.

[47] OPA Lattice Design Code. `https://ados.web.psi.ch/opa/`. Accessed: 2022-03-22.

[48] X. Huang, J. Corbett, J. Safranek, and J. Wu. An algorithm for online optimization of accelerators. *Nucl. Instrum. Methods Phys. Res. A*, 726:77–83, 2013.

[49] J. Laskar, C. Froeschlé, and A. Celletti. The measure of chaos by the numerical analysis of the fundamental frequencies. Application to the standard mapping. *Physica D: Nonlinear Phenomena*, 56(2):253–269, 1992. ISSN 0167-2789.

[50] S. Y. Lee. Decoherence of the Kicked Beams II. Technical Report SSCL-N-749, Fermilab, February 1991.

[51] P. Alexandre, R. Fekih, A. Letrésor, S. Thoraud, J. Castro, F. Bouvet, J. Breunlin, Å. Andersson, and P. Tavares. Transparent top-up injection into a fourth-generation storage ring. *Nucl. Instrum. Methods Phys. Res. A*, 986:164739, 2021.

[52] C. Sun, G. Portmann, M. Hertlein, J. Kirz, and D. S. Robin. Pseudo-Single-Bunch with Adjustable Frequency: A New Operation Mode for Synchrotron Light Sources. *Phys. Rev. Lett.*, 109, 2012.

[53] C. Stråhlman, T. Olsson, S. C. Leemann, R. Sankari, and S. L. Sorensen. Preparing the MAX IV Storage Rings for Timing-based Experiments. In *Proc. of the 12th International Conference on Synchrotron Radiation Instrumentation*, volume 1741, 2015.

[54] T. Olsson, S. C. Leemann, G. Georgiev, and G. Paraskaki. Pseudo-single-bunch mode for a 100 MHz storage ring serving soft X-ray timing experiments. *Nucl. Instrum. Methods Phys. Res. A*, 894:145–156, 2018.

[55] T. Olsson, Å. Andersson, and D. K. Olsson. Pulse-Picking by Resonant Excitation (PPRE) for Timing Users at the MAX IV 3 GeV Storage Ring. In *Proc. 9th International Particle Accelerator Conference*, pages 4300–4303, Vancouver, Canada, 2018.

[56] T. Olsson and Å. Andersson. First Measurement of Pulse Picking by Resonant Excitation (PPRE) at the MAX IV 3 GeV Storage Ring. In *Proc. 8th International Particle Accelerator Conference*, pages 2750–2752, Copenhagen, Denmark, 2017.

[57] D. Olsson, L. Malmgren, and A. Karlsson. The Bunch-by-Bunch Feedback System in the MAX IV 3 GeV Ring. Technical Report LUTEDX/(TEAT-7253)/1-48/(2017), 2017.

[58] E. D. Courant and H. S. Snyder. Theory of the alternating-gradient synchrotron. *Annals of Physics*, 3(1):1–48, 1958. ISSN 0003-4916.

[59] M. Johansson, B. Anderberg, and L.-J. Lindgren. Magnet design for a low-emittance storage ring. *Journal of synchrotron radiation*, 21:884–903, 09 2014.

Scientific publications

Author contributions / Comments on the papers

Paper I: Nonlinear optics from off-energy closed orbits

This paper describes the novel NOECO scheme developed at the MAX IV Laboratory. It shows the scheme's performance on a model lattice perturbed by magnet and alignment errors, proof-of-concept measurements, as well as a characterisation and correction of the 2nd order optics of the MAX IV 3 GeV storage ring. I was the main contributor to the design of NOECO, I also performed all simulations, measurements, data analysis, and wrote the paper.

Paper II: Commissioning and first-year operational results of the MAX IV 3 GeV ring

This paper presents results and experiences, from a number of different fields and systems, acquired during the commissioning and first-year operation of the 3 GeV ring. My contributions were limited to the optimisation and measurement of the dynamic aperture. This corresponds to sections 3.1 and 3.2 of the paper. The optimisation was performed by myself and Magnus Sjöström, while the measurements of the dynamic aperture, and the data analysis, was performed by me. All the writing and the figures in the two sections were done by me.

Paper III: Online Optimisation of the MAX IV 3 GeV Storage Ring Octupoles

This paper presents online optimisation performed on the MAX IV 3 GeV storage ring using the octupoles as fitting parameters. Two different objectives are investigated:

the increase of Touschek lifetime, and the shape of the ADTS relative to design. The performance of the resulting octupole settings is also investigated. All measurements and data analysis in the manuscript was performed by me. I also wrote the manuscript.

Paper IV: Studies on Transverse Resonance Island Buckets in third and fourth generation synchrotron light sources

This paper presents experiments with TRIBs performed on both MAX IV storage rings, although the focus is on the 1.5 GeV storage ring. Both simulations and measurements are presented, as well as the results of the first tests of the TRIBs optics done together with the FinEst and FlexPES beamlines. All measurements and simulations in the paper was performed by me. I also performed most of the theory and data analysis, and wrote the paper.

Paper V: 2nd Order Optics Symmetrisation through Off-Energy Orbit Response Matrix Analysis

This paper shows the early results of what would eventually become the NOECO scheme presented in Paper **I**. I conducted the measurements, performed the data analysis, and wrote the paper.

Paper VI: Trials of Beam-Based Sextupole Calibration through 2nd Order Dispersion

This paper presents a beam-based method of calibrating the chromatic sextupoles of a storage ring using the linearity of the 2nd order dispersion with chromatic sextupole strength. I conducted the measurements, performed the data analysis, and wrote the paper.

Paper VII: Online Optimisation of the MAX IV 3 GeV Ring Dynamic Aperture

This paper presents the first online optimisation performed on the MAX IV 3 GeV storage ring. The optimisation was with the purpose of increasing the horizontal kick resilience of the stored beam. Optimisations and measurements were conducted by me. I also performed the data analysis, and wrote the paper.

Appendix A

Derivations

This section presents derivations which are important for the completeness of this thesis, but were considered too long and cumbersome to be included in the theory section.

A.1 Derivation of the Equation of Motion

Here we will derive the equation of motion for a particle travelling in a magnetic field up to the order which is relevant in this thesis. The derivation follows that of Brown and Servranckx[14] with some conventions changed to match those used in this thesis.

Starting from the Lorentz force experienced by a charged particle moving through a static magnetic field

$$\mathbf{F} = \dot{\mathbf{p}} = e(\mathbf{v} \times \mathbf{B}) \tag{A.1}$$

where e is the charge of the particle, $\mathbf{v}$ is its velocity, and v its speed.

It is possible to write the velocity and momentum of the particle as $(\mathrm{d}\mathbf{T}/\mathrm{d}T)v$ and $(\mathrm{d}\mathbf{T}/\mathrm{d}T)p$, respectively, where p is the magnitude of the particle momentum, $\mathbf{T}$ its position vector, and T is its distance to the origin. The Lorentz force becomes

$$v\frac{\mathrm{d}}{\mathrm{d}T}\Big(\frac{\mathrm{d}\mathbf{T}}{\mathrm{d}T}p\Big) = vp\frac{\mathrm{d}^2\mathbf{T}}{\mathrm{d}T^2} + v\frac{\mathrm{d}\mathbf{T}}{\mathrm{d}T}\Big(\frac{\mathrm{d}p}{\mathrm{d}T}\Big) = ve\Big(\frac{\mathrm{d}\mathbf{T}}{\mathrm{d}T} \times \mathbf{B}\Big) \tag{A.2}$$

Since the magnetic force is always perpendicular to the velocity of a particle moving

through a static magnetic field we get that p is a constant of motion. The equation of motion can be simplified to

$$\frac{\mathrm{d}^2\mathbf{T}}{\mathrm{d}T^2} = \frac{e}{p}\left(\frac{\mathrm{d}\mathbf{T}}{\mathrm{d}T} \times \mathbf{B}\right) \tag{A.3}$$

The curvilinear coordinate system used for this derivation can be seen in Fig. A.1[14]. It satisfies the following relations, where primed variables indicate the derivative with respect to s, $\mathrm{d}/\mathrm{d}s$:

$$\begin{aligned} \hat{x} &= \hat{y} \times \hat{s},\ \hat{x}' = h\hat{s}, \\ \hat{y} &= \hat{s} \times \hat{x},\ \hat{y}' = 0, \\ \hat{s} &= \hat{x} \times \hat{y},\ \hat{s}' = -h\hat{x}, \end{aligned} \tag{A.4}$$

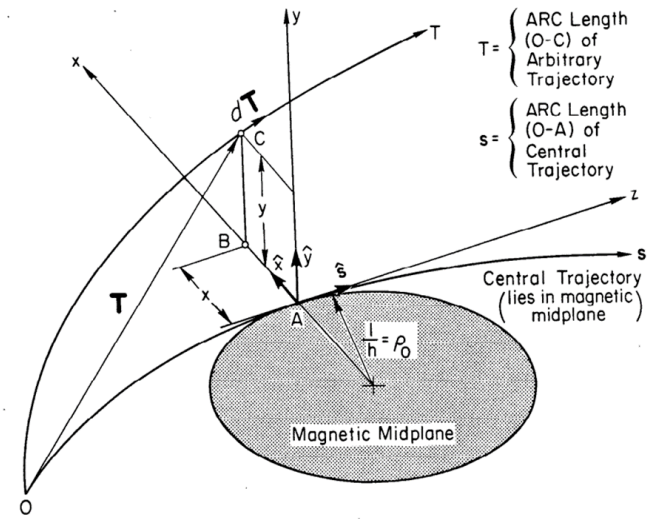

Figure A.1: The curvilinear coordinate system used when deriving the equation of motion[14].

The following relations can now be derived in order to rewrite the equation of motion

$$\frac{\mathrm{d}\mathbf{T}}{\mathrm{d}T} = \frac{(\mathrm{d}\mathbf{T}/\mathrm{d}s)}{\mathrm{d}T/\mathrm{d}s} = \frac{\mathbf{T}'}{T'} \tag{A.5}$$

$$\frac{\mathrm{d}^2\mathbf{T}}{\mathrm{d}T^2} = \frac{1}{T'}\frac{\mathrm{d}}{\mathrm{d}s}\left(\frac{\mathbf{T}'}{T'}\right) \tag{A.6}$$

$$T'^2 \frac{\mathrm{d}^2\mathbf{T}}{\mathrm{d}T^2} = \mathbf{T}'' - \frac{1}{2}\frac{\mathbf{T}'}{T'^2}\frac{\mathrm{d}}{\mathrm{d}s}(T'^2) \tag{A.7}$$

The equation of motion becomes

$$\mathbf{T}'' - \frac{1}{2}\frac{\mathbf{T}'}{T'^2}\frac{\mathrm{d}}{\mathrm{d}s}(T'^2) = \frac{e}{p}T'(\mathbf{T}' \times \mathbf{B}) \tag{A.8}$$

From the line element

$$\mathrm{d}\mathbf{T} = \hat{x}\mathrm{d}x + \hat{y}\mathrm{d}y + (1+hx)\hat{s}\mathrm{d}s \tag{A.9}$$

we can derive the following relations

$$T'^2 = x'^2 + y'^2 + (1+hx)^2 \tag{A.10}$$

$$\frac{1}{2}\frac{\mathrm{d}}{\mathrm{d}s}(T'^2) = x'x'' + y'y'' + (1+hx)(hx' + h'x) \tag{A.11}$$

$$\mathbf{T}' = \hat{x}x' + \hat{y}y' + (1+hx)\hat{s} \tag{A.12}$$

$$\mathbf{T}'' = \hat{x}\big(x'' - h(1+hx)\big) + \hat{y}y'' + \hat{s}(2hx' + h'x) \tag{A.13}$$

We can now rewrite the equation of motion and separate it into its components. For the horizontal plane the equation becomes

$$\begin{aligned} &x'' - h(1+hx) - \frac{x'}{T'^2}\Big(x'x'' + y'y'' + (1+hx)(hx' + h'x)\Big) \\ &= \frac{e}{p}T'\Big(y'B_s - (1+hx)B_y\Big) \end{aligned} \tag{A.14}$$

and for the vertical plane it becomes

$$\begin{aligned} &y'' - \frac{y'}{T'^2}\Big(x'x'' + y'y'' + (1+hx)(hx' + h'x)\Big) \\ &= \frac{e}{p}T'\Big((1+hx)B_x - x'B_s\Big) \end{aligned} \tag{A.15}$$

Table A.1: The first four orders of the multipole expansion of the magnetic field as defined by Eq. (A.19).

dipole	$h = \frac{e}{p} B_{y0} = \frac{e}{p} A_{10}$
quadrupole	$k = \frac{e}{p} \frac{\partial B_y}{\partial x}\Big\|_{x,y=0} = \frac{e}{p} A_{11}$
sextupole	$m = \frac{e}{p} \frac{\partial^2 B_y}{\partial x^2}\Big\|_{x,y=0} = \frac{e}{p} A_{12}$
octupole	$o = \frac{e}{p} \frac{\partial^3 B_y}{\partial x^3}\Big\|_{x,y=0} = \frac{e}{p} A_{13}$

The longitudinal plane has been omitted since its higher order equation of motion is not used in this thesis.

We now expand T'^{-2} and keep only cubic terms and lower. The left-hand sides of the equations of motion become

$$x'' - h(1 + hx) + x'(h^2 x x' + h h' x^2 - h x' - h' x - x' x'' - y' y'') \tag{A.16}$$

and

$$y'' + y'(h^2 x x' + h h' x^2 - h x' - h' x - x' x'' - y' y'') \tag{A.17}$$

A magnetic field in vacuum with zero current density can be expressed as a scalar potential ϕ, with $\mathbf{B} = \nabla\phi$, where the minus sign has been omitted for convenience. The scalar potential can be written in the general form

$$\phi(x, y, s) = \sum_{m=0}^{\infty} \sum_{n=0}^{\infty} A_{2m+1,n} \frac{x^n}{n!} \frac{y^{2m+1}}{(2m+1)!} \tag{A.18}$$

From the potential we get the components of $\mathbf{B} = \nabla\phi$

$$\begin{aligned} B_x &= \frac{\partial \phi}{\partial x} = \sum_{m=0}^{\infty} \sum_{n=0}^{\infty} A_{2m+1,n+1} \frac{x^n}{n!} \frac{y^{2m+1}}{(2m+1)!} \\ B_y &= \frac{\partial \phi}{\partial y} = \sum_{m=0}^{\infty} \sum_{n=0}^{\infty} A_{2m+1,n} \frac{x^n}{n!} \frac{y^{2m}}{(2m)!} \\ B_s &= \frac{1}{(1+hx)} \frac{\partial \phi}{\partial s} = \frac{1}{(1+hx)} \sum_{m=0}^{\infty} \sum_{n=0}^{\infty} A'_{2m+1,n} \frac{x^n}{n!} \frac{y^{2m+1}}{(2m+1)!} \end{aligned} \tag{A.19}$$

From this it is possible to identify the standard multipole terms as seen in Tab. A.1. We expand the expressions in Eq. (A.19) keeping only 3rd and lower order terms:

$$
\begin{aligned}
B_x &= A_{11}y + A_{12}xy + \frac{1}{2}A_{13}x^2y + \frac{1}{6}A_{31}y^3 \\
B_y &= A_{10} + A_{11}x + \frac{1}{2}A_{12}x^2 + \frac{1}{6}A_{13}x^3 + \frac{1}{2}A_{30}y^2 + \frac{1}{2}A_{31}xy^2 \\
B_s &= A'_{10}y + (A'_{11} - hA'_{10})xy + (\frac{1}{2}A'_{12} - hA'_{11} + h^2A'_{10})x^2y + \frac{1}{6}A'_{30}y^3
\end{aligned}
\tag{A.20}
$$

Using the above expressions and the expansion of Eq. (A.10) the right-hand sides of equations (A.14) and (A.15) can be expanded

$$
\begin{aligned}
&\frac{e}{p}T'(y'B_s - (1+hx)B_y) = \\
&-h - (2h^2+k)x - (h^3 + \frac{1}{2}m + 2hk)x^2 - \frac{1}{2}hx'^2 \\
&+ \frac{1}{2}(h'' + hk + m)y^2 + h'yy' - \frac{1}{2}hy'^2 \\
&- (h^2k + hm + \frac{1}{6}o)x^3 + \frac{1}{2}(-h'^2 + h^2k + 3hm + k'' + o)xy^2 \\
&+ k'xyy' - \frac{1}{2}kx(x'^2 + y'^2)
\end{aligned}
\tag{A.21}
$$

$$
\begin{aligned}
&\frac{e}{p}T'((1+hx)B_x - x'B_s) = \\
&ky + (2hk+m)xy - h'x'y + \frac{1}{6}(2hh'' + h'^2 + h^2k - hm - k'' - o)y^3 \\
&+ (h^2k + 2hm + \frac{1}{2}o)x^2y - k'xx'y + \frac{1}{2}kx'^2y + \frac{1}{2}kyy'^2
\end{aligned}
\tag{A.22}
$$

where the following relations have been used[14]:

$$
\begin{aligned}
A_{30} &= -A''_{10} - A_{12} - hA_{11} \\
A_{31} &= -A''_{11} + 2hA''_{10} + h'A'_{10} - A_{13} - hA_{12} + h^2A_{11}
\end{aligned}
\tag{A.23}
$$

In order to account for energy deviations we can expand

$$
\frac{1}{p} = \frac{1}{p_0(1+\delta)} = \frac{1}{p_0}\sum_{n\geq 0}(-\delta)^n \tag{A.24}
$$

The full horizontal equation of motion to third order finally becomes

$$
\begin{aligned}
&x'' - h(1+hx) + x'(h^2xx' + hh'x^2 - hx' - h'x - x'x'' - y'y'') = \\
&(1-\delta+\delta^2-\delta^3)\Big[-h - (2h^2+k)x - (h^3 + \frac{1}{2}m + 2hk)x^2 - \frac{1}{2}hx'^2 \\
&+ \frac{1}{2}(h'' + hk + m)y^2 + h'yy' - \frac{1}{2}hy'^2 \\
&- (h^2k + hm + \frac{1}{6}o)x^3 + \frac{1}{2}(-h'^2 + h^2k + 3hm + k'' + o)xy^2 \\
&+ k'xyy' - \frac{1}{2}kx(x'^2 + y'^2)\Big]
\end{aligned}
\tag{A.25}
$$

and the vertical equation of motion becomes

$$
\begin{aligned}
&y'' + y'(h^2xx' + hh'x^2 - hx' - h'x - x'x'' - y'y'') = \\
&(1-\delta+\delta^2-\delta^3)\Big[ky + (2hk+m)xy - h'x'y \\
&+ \frac{1}{6}(2hh'' + h'^2 + h^2k - hm - k'' - o)y^3 \\
&+ (h^2k + 2hm + \frac{1}{2}o)x^2y - k'xx'y + \frac{1}{2}kx'^2y + \frac{1}{2}kyy'^2\Big]
\end{aligned}
\tag{A.26}
$$

The above two equations of motion (Eq. (A.25) and Eq. (A.26)), although cumbersome, are useful when investigating the behaviour of higher order transverse beam dynamics.

A.2 Floquet's Transformation

Floquet's transformation [21] is a useful tool when calculating both the linear and higher order dispersion functions, as well as the closed orbit distortion from a dipole kick. In order to not needlessly repeat these very similar calculations a more general case is presented here. This derivation somewhat follows that of Wille [9], but similar derivations can be found in other literature [19,22].

The equation to be solved is the general linear equation of motion (see Eq. (3.7)) subjected to some longitudinally dependent perturbation, $f(s)$,

$$q_i(s)'' + K(s)q_i(s) = f(s) \tag{A.27}$$

where $K(s)$ is a piece-wise continuous function representing the focusing of the lattice. In order to increase the legibility of the derivation the longitudinal dependence of q_i will not be explicitly written out.

We introduce the following Floquet's transformation to find the periodic solution to the above equation [19]

$$\begin{aligned} \Phi(s) &\equiv \frac{\Psi_i(s)}{\nu_i} = \frac{1}{\nu_i}\int_0^s \frac{\mathrm{d}\sigma}{\beta_i(s)} \\ w(s) &\equiv \frac{q_i}{\sqrt{\beta_i(s)}} \end{aligned} \tag{A.28}$$

where, once again, the longitudinal dependence of Φ and w will not be explicitly written out.

The derivatives with respect to the new variables are

$$\begin{aligned} \frac{\mathrm{d}w}{\mathrm{d}\Phi} &= \frac{\mathrm{d}w}{\mathrm{d}s}\frac{\mathrm{d}s}{\mathrm{d}\Phi} = \frac{\mathrm{d}}{\mathrm{d}s}\Big(\frac{q_i}{\sqrt{\beta_i(s)}}\Big)\nu_i\beta_i(s) \\ &= \Big(\frac{\alpha_i(s)}{\sqrt{\beta_i(s)}}q_i + \sqrt{\beta_i(s)}q_i'\Big)\nu_i \\ \frac{\mathrm{d}^2w}{\mathrm{d}\Phi^2} &= \frac{\mathrm{d}}{\mathrm{d}s}\Big(\frac{\mathrm{d}w}{\mathrm{d}\Phi}\Big)\nu_i\beta_i(s) \\ &= \Big[\beta_i^{3/2}(s)q_i'' + \Big(\frac{\alpha_i^2(s)}{\sqrt{\beta_i(s)}} + \alpha_i'(s)\sqrt{\beta_i(s)}\Big)q_i\Big]\nu_i^2 \end{aligned} \tag{A.29}$$

In order to continue the derivation an expression for $\alpha_i'(s)$ needs to be found. Although this can be found in literature[9,19,22] it will also be derived here for the sake of completion. Rewriting Eq. (3.8) using the trigonometric angle sum identities results in

$$\begin{aligned} q_i =& \sqrt{\varepsilon_i}\sqrt{\beta_i(s)}\Big[\cos\Psi_i(s)\cos\phi_i - \sin\Psi_i(s)\sin\phi_i\Big] \\ q_i' =& -\frac{\sqrt{\varepsilon_i}}{\sqrt{\beta_i(s)}}\Big[\alpha_i(s)\cos\Psi_i(s)\cos\phi_i - \alpha_i(s)\sin\Psi_i(s)\sin\phi_i \\ &+ \sin\Psi_i(s)\cos\phi_i + \cos\Psi_i(s)\sin\phi_i\Big] \end{aligned} \tag{A.30}$$

By introducing initial values at some longitudinal position s_0, $q_i(s_0) = q_{i0}$, $q_i'(s_0) = q_{i0}'$, $\beta_i(s_0) = \beta_{i0}$, $\alpha_i(s_0) = \alpha_{i0}$, and $\Psi_i(s_0) = 0$ we can find an expression for the initial phase, ϕ_i, and insert this into Eq. (A.30), resulting in

$$\begin{aligned} q_i =& \sqrt{\frac{\beta_i(s)}{\beta_{i0}}}\Big[\cos\Psi_i(s) + \alpha_{i0}\sin\Psi_i(s)\Big]q_{i0} + \sqrt{\beta_i(s)\beta_{i0}}\sin\Psi_i(s)q_{i0}' \\ q_i' =& \frac{1}{\sqrt{\beta_i(s)\beta_{i0}}}\Big[\big(\alpha_{i0} - \alpha_i(s)\big)\cos\Psi_i(s) - \big(1 + \alpha_{i0}\alpha_i(s)\big)\sin\Psi_i(s)\Big]q_{i0} \\ &+ \sqrt{\frac{\beta_{i0}}{\beta_i(s)}}\Big[\cos\Psi_i(s) - \alpha_i(s)\sin\Psi_i(s)\Big]q_{i0}' \end{aligned} \tag{A.31}$$

which can be written as

$$\begin{pmatrix} q_i \\ q_i' \end{pmatrix} = \mathbf{M}\begin{pmatrix} q_{i0} \\ q_{i0}' \end{pmatrix} \tag{A.32}$$

with

$$\mathbf{M} = \begin{pmatrix} \sqrt{\frac{\beta_i}{\beta_{i0}}}\big(\cos\Psi_i + \alpha_{i0}\sin\Psi_i\big) & \sqrt{\beta_i\beta_{i0}}\sin\Psi_i \\ \frac{\big(\alpha_{i0}-\alpha_i\big)\cos\Psi_i - \big(1+\alpha_{i0}\alpha_i\big)\sin\Psi_i}{\sqrt{\beta_i\beta_{i0}}} & \sqrt{\frac{\beta_{i0}}{\beta_i}}\big(\cos\Psi_i - \alpha_i\sin\Psi_i\big) \end{pmatrix} \tag{A.33}$$

where the longitudinal dependence of the Twiss parameters and the phase advance is no longer explicitly written out.

With Eq. (A.32) it is possible to calculate the phase-space position of a particle at any longitudinal position given the initial position of the particle, the phase advance, and the Twiss parameters. For a full revolution of a storage ring the transfer matrix becomes

$$\mathbf{M}_{s\to s+L} = \begin{pmatrix} \cos\mu + \alpha_i \sin\mu & \beta_i \sin\mu \\ -\gamma_i \sin\mu & \cos\mu - \alpha_i \sin\mu \end{pmatrix} \tag{A.34}$$

where $\mu = 2\pi\nu_i$, omitting the subscript i for simplicity.

Advancing the longitudinal position by an infinitesimal distance ds the full revolution transfer matrix becomes

$$\begin{aligned} \mathbf{M}_{s+ds\to s+ds+L} &= \begin{pmatrix} \cos\mu + \left(\alpha_i + \frac{\mathrm{d}\alpha_i}{\mathrm{d}s} ds\right) \sin\mu & \left(\beta_i + \frac{\mathrm{d}\beta_i}{\mathrm{d}s} ds\right) \sin\mu \\ -\left(\gamma_i + \frac{\mathrm{d}\gamma_i}{\mathrm{d}s} ds\right) \sin\mu & \cos\mu - \left(\alpha_i + \frac{\mathrm{d}\alpha_i}{\mathrm{d}s} ds\right) \sin\mu \end{pmatrix} \\ &= \mathbf{M}_{s\to s+L} + \begin{pmatrix} \alpha_i' \sin\mu & \beta_i' \sin\mu \\ -\gamma_i' \sin\mu & -\alpha_i' \sin\mu \end{pmatrix} ds \end{aligned} \tag{A.35}$$

This matrix can be expressed in another form by treating the propagation over a full turn, L, and the infinitesimal distance, ds, separately. The resulting transfer matrix will be identical regardless of whether the propagation over L or ds is applied first

$$\mathbf{M}_{s+ds\to s+ds+L} \mathbf{M}_{s\to s+ds} = \mathbf{M}_{s\to s+ds} \mathbf{M}_{s\to s+L} \tag{A.36}$$

The transfer matrix over ds is given by

$$\mathbf{M}_{s\to s+ds} = \begin{pmatrix} 1 & ds \\ -K(s)ds & 1 \end{pmatrix} \tag{A.37}$$

where $K(s)$ is the generalised focussing gradient found in Eq. (A.27).

Solving Eq. (A.36) for $\mathbf{M}_{s+ds\to s+ds+L}$ results in

$$
\begin{aligned}
&\mathbf{M}_{s+ds\to s+ds+L} \\
&= \begin{pmatrix} 1 & ds \\ -K(s)ds & 1 \end{pmatrix} \begin{pmatrix} \cos\mu + \alpha_i \sin\mu & \beta_i \sin\mu \\ -\gamma_i \sin\mu & \cos\mu - \alpha_i \sin\mu \end{pmatrix} \begin{pmatrix} 1 & -ds \\ K(s)ds & 1 \end{pmatrix} \\
&= \mathbf{M}_{s\to s+L} + \begin{pmatrix} \big(\beta_i K(s) - \gamma_i\big)\sin\mu & -2\alpha_i \sin\mu \\ -2K(s)\alpha_i \sin\mu & -\big(\beta_i K(s) - \gamma_i\big)\sin\mu \end{pmatrix} ds
\end{aligned}
\tag{A.38}
$$

which can be compared to Eq. (A.35) to obtain

$$
\begin{aligned}
\alpha_i'(s) =& \beta_i(s)K(s) - \gamma_i(s) \\
\beta_i'(s) =& -2\alpha_i(s) \\
\gamma_i'(s) =& 2\alpha_i(s)K(s)
\end{aligned}
\tag{A.39}
$$

finally allowing us to rewrite the second derivative in Eq. (A.29) as

$$
\frac{\mathrm{d}^2 w}{\mathrm{d}\Phi^2} = \Big[\beta_i^{3/2}\big(q_i'' + K(s)q_i\big) - \frac{q_i}{\sqrt{\beta_i}}\Big]\nu_i^2 \tag{A.40}
$$

The initial equation of motion (Eq. (A.27)) has now been transformed from forced oscillations of Hill's equation to forced oscillations of a harmonic oscillator

$$
\frac{\mathrm{d}^2 w}{\mathrm{d}\Phi^2} + \nu_i^2 w = \nu_i^2 \beta_i^{3/2} f(s) \tag{A.41}
$$

Regarding the right-hand side of Eq. (A.41) as a function of Φ, the know solution[58] can be written as

$$
w(\Phi) = \frac{\nu_i}{2\sin\pi\nu_i} \int_{\Phi}^{\Phi+2\pi} \beta_i^{3/2} f(\psi) \cos\nu_i(\pi + \Phi - \psi)\mathrm{d}\psi \tag{A.42}
$$

Introducing the original variables results in the solution to the perturbed equation of motion

$$
q_i(s) = \frac{\sqrt{\beta_i(s)}}{2\sin\pi\nu_i} \int_{s}^{s+L} \sqrt{\beta_i(\sigma)} f(s) \cos\big(\pi\nu_i + \Psi(s) - \Psi(\sigma)\big)\mathrm{d}\sigma \tag{A.43}
$$

Depending on the perturbation, $f(s)$, the above equation gives the expression for any order of dispersion, as well as the closed orbit distortion from distributed dipole errors.

Appendix B

The MAX IV Storage Ring Lattices

In this section the lattice structures of the MAX IV storage rings are presented, along with some fundamental parameters of each machine. This aims to serve as a useful reference for the reader.

B.1 The 3 GeV Storage Ring

The work presented in this thesis which involves the MAX IV 3 GeV storage ring focusses mainly on the sextupoles and octupoles of the ring, leaving the linear elements to the well established LOCO scheme[44]. Therefore, the following overview of the lattice structure will not include details regarding the bending dipoles nor the quadrupoles. For more details of the application of LOCO on the 3 GeV ring see Sec. 4.1 and Paper **II**. For a more thorough review of the 3 GeV ring lattice, including the linear lattice, see the MAX IV detailed design report[16] and internal note[46].

The 3 GeV storage ring lattice consists of 20 optically identical achromats, which are each symmetric around their centre point. With its seven-bend achromat structure, the ring is the first realised multi-bend lattice and can be considered the first fourth generation synchrotron. The beta and dispersion functions of the 3 GeV storage ring can be seen in Fig. B.1, while some of the important parameters of the ring can be seen in Tab. B.1.

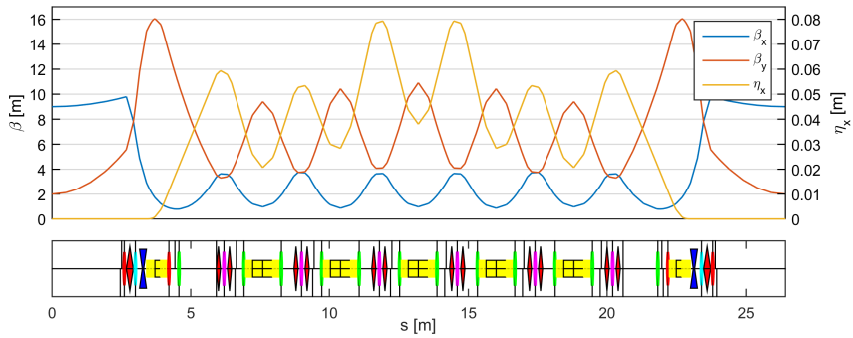

Figure B.1: Top: Nominal beta functions and horizontal (first order) dispersion of the 3 GeV storage ring achromat. Since the vertical dispersion is nominally zero it has been omitted from the plot. Bottom: Longitudinal position of magnetic elements. For a more detailed overview see figures B.2 and B.3.

BPMs and Dipole Correctors

Each achromat of the 3 GeV ring contains a total of 10 BPMs, 10 horizontal dipole correctors, and 9 vertical dipole correctors. Their distribution along the achromat can be seen in Fig. B.2. In the case of the vertical dipole correctors the second corrector shown in the figure is not present as it would block the extraction of synchrotron radiation from the preceding ID straight section.

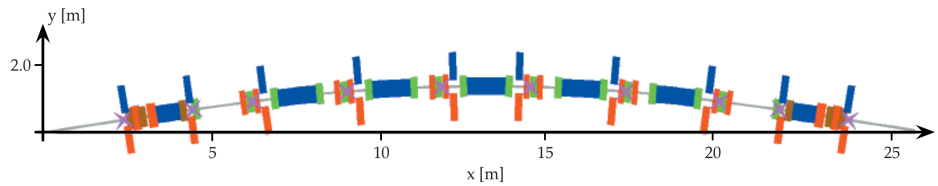

Figure B.2: Position of BPMs (magenta crosses) and horizontal and vertical dipole corrector magnets (blue and orange stripes) in the 3 GeV storage ring achromats. In the case of the vertical dipole correctors the second corrector in the image is not present.

Sextupoles and Octupoles

The 3 GeV ring has a total of five sextupole magnet families: SD, SDend, SFi, SFo, and SFm, all of which are chromatic. Their locations in the achromat can be seen in Fig. B.3. All magnets belonging to the same family are connected in series to a single circuit within each achromat. The only exception is the SFi family in achromat 8, where the circuit is split up for the purpose of BPM offset investigations. In total, there are 101 independent sextupole circuits in the MAX IV 3 GeV storage ring. In the case of the SDend, SFi, SFo, and SFm families, each circuit consists of two magnets,

Table B.1: Important parameters of the MAX IV 3 GeV storage ring.

Periodicity	20
Circumference	528 m
Horizontal tune ν_x	42.20
Vertical tune ν_y	16.28
Natural horizontal chromaticity ξ_x	-49.984
Natural vertical chromaticity ξ_y	-50.198
Momentum compaction factor α_c (linear)	3.06×10^{-4}
Horizontal emittance ε_x (bare lattice, at I = 0 mA)	0.328 nmrad
Energy loss per turn (bare lattice)	363.8 keV
Natural energy spread σ_δ (bare lattice)	0.769×10^{-3}
Horizontal damping time τ_x (bare lattice)	15.725 ms
Vertical damping time τ_y (bare lattice)	29.047 ms
Longitudinal damping time τ_E (bare lattice)	25.0194 ms
Horizontal beta function at centre of LS β_x (bare lattice)	9.00 m
Vertical beta function at centre of LS β_y (bare lattice)	2.00 m

with the exception of the two aforementioned SFi circuits in achromat 8 which each consist of a single magnet. In the case of the SD family, each circuit consists of 10 magnets.

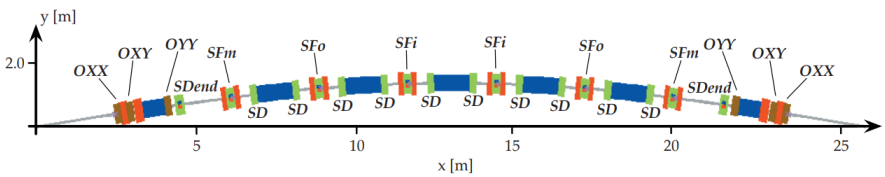

Figure B.3: Locations of sextupoles (green) and octupoles (brown) in the 3 GeV storage ring achromats. The remaining elements are bending dipoles (blue) and quadrupoles (orange). Adapted from the MAX IV detailed design report [16].

The ring also has three families of octupoles: OXX, OXY, and OYY. Their locations in the achromat can be seen in Fig. B.3. All octupole magnets belonging to the same family are connected in series in a single circuit across the ring. The only exception is the OXX and OXY magnets in achromat 1 which are connected to a separate circuit as these magnets have a different pole gap to allow for injection. The OXX and OXY families are achromatic, while the OYY family is weakly chromatic.

Should a correction of individual magnets be required, rather than relying solely on the circuits, each magnet, including lower order magnets, is individually connected to a shunt board. The shunt board consists of an array of resistors with different resistances. These can be connected in parallel to the magnet coil, allowing for precise corrections of individual magnet strengths. At the time of writing, these shunt boards are not in use for any magnet family as they have not yet been required to achieve the desired lattice performance.

On all families of sextupoles, as well as octupoles, there are additional coil windings which are powered independently of the main coils. These *trim coils* can be powered to function as horizontal or vertical dipole correctors, quadrupoles, or skew quadrupoles. In the case of the sextupoles, the trim coils can also be powered create a sextupole field[59]. Each of the above mentioned magnets have a separate power supply feeding its trim coils, allowing them to be powered individually within the magnet families. At the time of writing, the trim coils of the SFm, SFo, and OXX families are used in skew quadrupole mode to correct coupling using LOCO, while the trim coils of a few of the OYY magnets are used in vertical dipole corrector mode to alleviate the saturation of a few vertical dipole correctors when correcting the orbit position in the BPMs. Additionally, the trim coils are used in quadrupole mode when finding the offset of nearby BPMs (see Paper **II** and Chap. 3 Sec. 3.6 for further details).

B.2 The 1.5 GeV Storage Ring

Unlike the MAX IV 3 GeV storage ring, the 1.5 GeV storage ring is a more standard third generation synchrotron with a double-bend achromat structure. The lattice consists of 12 optically identical achromats which are each symmetric around their centre point. A schematic of the achromat can be seen in Fig. B.5. Each achromat contains two focussing combined quadrupole-sextupole magnet families: SQFi and SQFo, while the defocussing quadrupole gradient is integrated in the pole shape of the bending dipoles. The SQFi family is chromatic, while the SQFo family is harmonic. The optical functions of the ring can be seen in Fig. B.4, while some of its important parameters can be seen in Tab. B.2. For more details see see the MAX IV detailed design report[16].

All magnets belonging to the SQFi family are connected in series and powered by a single power supply. The SQFo family is split up into six separate circuits: five powering two magnets each, with each pair flanking an ID straight section, and one powering all the remaining magnets. This split-up has been done for the purposes of compensating ID focussing. All magnets of the 1.5 GeV storage ring are connected to shunt boards similar to those described in B.1. These are utilised in the case of the SQFi and SQFo families to achieve a more uniform focussing gradient throughout the ring.

In addition to the combined quadrupole-sextupole magnets the ring also contains two main defocussing families of sextupoles: SDi and SDo, as well as two corresponding sextupole corrector families: SCi and SCo. The SDi and SCi families are chromatic, while the SDo and SCo families are harmonic.

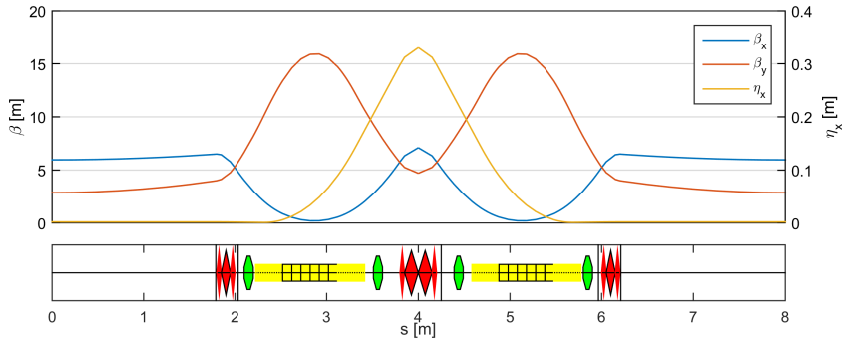

Figure B.4: Top: Nominal beta functions and horizontal (first order) dispersion of the 1.5 GeV storage ring achromat. Since the vertical dispersion is nominally zero it has been omitted from the plot. Bottom: Longitudinal position of magnetic elements. For a more detailed overview see Fig. B.5.

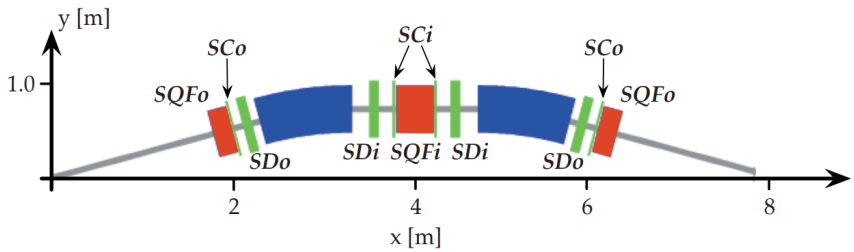

Figure B.5: Locations of the combined quadrupole-sextupoles (orange) and sextupoles (green). The remaining elements (blue) are the two dipole bending magnets.

Table B.2: Important parameters of the MAX IV 1.5 GeV storage ring.

Periodicity	12
Circumference	96 m
Horizontal tune ν_x	11.22
Vertical tune ν_y	3.15
Natural horizontal chromaticity ξ_x	-22.964
Natural vertical chromaticity ξ_y	-17.154
Momentum compaction factor α_c (linear)	3.055×10^{-3}
Horizontal emittance ε_x (bare lattice, at I = 0 mA)	5.982 nmrad
Energy loss per turn (bare lattice)	114.1 keV
Natural energy spread σ_δ (bare lattice)	0.745×10^{-3}
Horizontal damping time τ_x (bare lattice)	5.751 ms
Vertical damping time τ_y (bare lattice)	8.417 ms
Longitudinal damping time τ_E (bare lattice)	5.479 ms
Horizontal beta function at centre of LS β_x (bare lattice)	5.69 m
Vertical beta function at centre of LS β_y (bare lattice)	2.84 m

Printed by Media-Tryck, Lund 2022 NORDIC SWAN ECOLABEL 3041 0903

ISBN 978-91-8039-362-1
Division of Synchrotron Radiation Research
Department of Physics
Faculty of Science
Lund University